Inferring the Impacts of Anthropogenic Changes and Catchment Spatial Heterogeneity on the Water Cycle Dynamics and Transport Time Scales

A Dissertation
SUBMITTED TO THE FACULTY OF
UNIVERSITY OF MINNESOTA
BY

Mohammad Danesh-Yazdi

IN PARTIAL FULFILLMENT OF THE REQUIREMENTS
FOR THE DEGREE OF
DOCTOR OF PHILOSOPHY

Efi Foufoula-Georgiou, Advisor

February 2017

Acknowledgements

When I joined St. Anthony Falls Laboratory (SAFL) in 2011, I was the youngest not only in our group but also in the whole lab. I had thus a lot of lessons to learn, particularly the criticality in work, which was always emphasized by my adviser, Efi Foufoula-Georgiou. I do appreciate her generous scientific and financial supports as well as the freedom she gave me to explore my own research ideas.

Needless to say, my Ph.D. path was extremely tortuous, making me gasp many times. I couldn't climb mountains of disappointment and difficulties without the sincere support of my family back in Yazd and friends in Minneapolis. Ali (my decision-making adviser), Nasim (for her endless kindness), Amin Tadayon (who helped me so much to come over various challenges at the beginning of my graduate studies), John Schwenk (for the fun times we had together), Breda folks (Davood Taherinia, Mohammad Mohsen Mahmoodi (from Isfahan), and Fazel Zare Bidoky for their warm hosting and enjoyable friendship), and Beyt-e Badri (for organizing entertainments). You guys have already occupied a part of my heart.

Diligence has always been my main thrust toward success. However, I cannot deny the very special role of poetry, music, and painting in my personal life as the secondary motivating powers. I am deeply grateful to Fereydoon Moshiri, Sohrab Sepehri, Foroogh Farokhzad, and Hossein Monzavi for being the reason I started writing poem, Mohammad Reza Shajarian, Shahram Nazeri, Parviz Meshkatian, and Behdad Babaie whose touching music encouraged me to start playing Setar, and Mojdeh Kazem who paved my way to the beautiful world of colors by mentoring me in watercolor painting. Very pleasant and soothing moments from our literary circle composing of Mahdi Ahmadi (a talented writer), Reza Halvagar, Farzad Shirazi, Sara Parhizgari (the first philosophist I've ever met), Hamidreza Badri (who increased my confidence in PES by losing one after another), Shahrzad Zafaranloo, and Ensiye Mohammadi, have left an everlasting color on the canvas of my diaries. I will never forget the influence that Akaky Akakievich, Hossein Sabzian, and Akbar Norouzi have had in my vision toward life.

And ultimately, every single word of this dissertation is dedicated to my guardian angels, Marzieh Tavakoli and Reza Danesh-Yazdi.

To my parents, Marzieh and Reza

Abstract

Climatic trends and anthropogenic interventions during past decades have undeniably impacted the hydrology and water quality of streams at the field, watershed, and regional scales in complex ways. This dissertation has developed a quantitative framework within which first-order estimates of the relative changes in travel time statistics in those landscapes undergoing substantial alterations in land-use land-cover can be quantified. Results from analysis of a sub-basin in the Minnesota River Basin located in the Midwestern United States indicated a significant decrease in the mean travel time of water in the shallow subsurface layer during the growing season under current conditions compared to the pre-1970's conditions. Highly damped year-to-year fluctuations in the mean travel time were also found, which were attributed to the homogenization of the hydrologic response due to artificial drainage. Regarding the lack of high spatiotemporal resolution hydro-chemical data (in many catchments) required for an accurate estimation of transport time scales, this work has explored whether a lumped system representation via a time-varying stochastic Lagrangian formulation can provide reliable estimates of mean travel time in spatially heterogeneous catchments in the absence of within-catchment observations. This time (variability) for space (heterogeneity) substitution yielded mean travel times that are not significantly biased to the aggregation of spatial heterogeneity under different sampling assumptions. Despite the significant variability of mean travel time at small spatial scales, there exists a characteristic scale above which the mean travel time is not impacted by the aggregation of spatial heterogeneity. Extensive simulations of randomly generated river networks revealed that the ratio between the characteristic scale and the mean incremental area is on average independent of river network topology and the spatial arrangement of incremental areas. As the river network structure (which is typically considered self-similar) might impose a significant control on the in-stream transport time scales and be used to explain some properties of the relating physical processes, we further explored those river networks that do not obey the typical self-similar relationships over a range of spatial scales. We proposed methodologies that can probe into the structure of such outlier basins, called self-dissimilar, in ways that are able to reveal their spatially heterogeneous organization and quantify preferential scales of dissection, which in turn can influence the transport and storage time scales at large-scale catchments with implications for solute transport and water quality.

Table of Contents

List of Tables

List of Figures

1

Introduction

River basins around the world are undergoing hydrologic change due to climatic and/or anthropogenic stressors. Among them, intensively managed landscapes experience changes in their coupled hydro-bio-geochemical cycles with remarkable implications for water quality and aquatic life [e.g., *Kladivko et al.*, 2001; *Zedler et al.*, 2003; *Kanwar et al.*, 2005]. This research was motivated by agricultural landscapes in the Midwestern United States which have undergone significant changes in land-cover land-use (LULC) over the past several decades [e.g., *Schilling and Helmers*, 2008], raising serious concerns due to increased concentrations of nitrate, phosphorus, and pesticides in streams [e.g., *Skaggs et al.*, 1994; *Tomer et al.*, 2003; *Blann et al.*, 2009]. The replacement of hay and small grains with row crops of corn and soybean in the Upper Midwestern basins since the 1970's [e.g., *Foufoula-Georgiou et al.*, 2015 and references therein] has been accompanied by an expansion of artificial surface and subsurface drainage, and also conversion of forests and wetlands to agricultural lands. In Minnesota, 50% of wetlands statewide and 90% in the southern and western regions have been drained for agricultural purposes since 1850 [*Minnesota Pollution Control Agency (MPCA)*, 2006]. In the Redwood River Basin (one of the major sub-basins of the Minnesota River Basin (MRB)), the tile drainage density, i.e., total length of tiles

divided by the drainage area, has been more than doubled in two decades from 2.90 km^{-1} in 1991 to 6.34 km^{-1} in 2010 [*Minnesota State University, Water Resources Center*]. As a result of such practices, more than 40% of the lakes and rivers in Minnesota do not meet water quality standards mostly due to excess nutrients arising from agricultural fields, which have been recognized to be the source for 40% of phosphorus and 78 % of nitrogen delivery into water bodies [*MPCA*, 2013].

Such LULC alterations have undoubtedly changed the water cycle dynamics [e.g., *Chapman et al.*, 2005; *Zhang and Schilling*, 2006; *Basu et al.*, 2011; *Foufoula-Georgiou et al.*, 2015] which in turn have impacted water and solute transport time scales. Understanding changes in the transport time scales, including residence times in the soil column and/or in natural depressions or wetlands in intensively managed landscapes, is important as these time scales modulate changes in chemical and biogeochemical reactions affecting the quality of water entering the streams [e.g., *Clement et al*., 2003]. For instance, total annual nitrate load can be 2−4 times larger in extensively drained landscapes as opposed to low-drained conditions, depending on the tile drainage density [e.g., *Spaling*, 1995; *Monaghan et al.*, 2000; *Mcisaac and Hu*, 2004; *Kennedy et al.*, 2012]. By studying 11 North American and European estuaries having a wide range of physical characteristic, *Dettmann* [2001] found a strong positive correlation between water residence time and denitrification loss of nitrogen such that nitrogen export can be decreased by 10% and 50% in estuaries with 3.3 and 30 months of water residence time, respectively. Also, via modeling of 40 wetlands in southern Sweden, *Arheimer and Wittgren* [2002] indicated that nitrogen removal is enhanced from 14% to 40% in wetlands with residence times of 25 days and 106 days, respectively.

Accurate estimation of water and solute transport time scales requires high-quality, high spatiotemporal resolution hydrologic, chemical, or isotopic data over prolonged periods of time, which are rarely available [e.g., *Hrachowitz et al.*, 2011]. Even if this information is available at the field scale, how to upscale information from the field

scale to the catchment scale is still a challenge both in terms of effective modeling parameterizations and in using available observations. This reinforces adopting an aggregated systems approach for estimating water and solute transport properties at the catchment scale [e.g., *Botter et al.*, 2011; *Benettin et al.*, 2013a, 2015a], at the expense, however, of introducing another challenge of how to find relevant lumped system representations that allow for accurate estimation of whole catchment behavior without explicitly incorporating the within-catchment (unknown) spatial heterogeneity.

We have discussed so far the physical processes and transport time scales corresponding to the catchment subsurface layer and/or surface water depressions. However, some natural processes such as hyporheic exchanges and interactions with riparian zones take place in streams. The transport features engaging with these processes, thus, cannot be understood without considering their influence across many (mostly heterogeneous) parts of the drainage system, including the terrestrial landscape and channels of the river network [e.g., *Lindgren et al.*, 2004; *Mulholland et al.*, 2008; *Ranalli and Macalady*, 2010]. Characterization of a river network via its river network topology facilitates exploring the connections between the river network structure and in-stream natural processes [e.g., *Power and Dietrich*, 2002; *Kiffney et al.*, 2006; *Sklar et al.*, 2006; *Stewart-Koster et al.*, 2007; *Muneepeerakul et al*., 2008; *Czuba et al.*, 2015] through, e.g., some scaling relationships. These relationships presume that the river network exhibits self-similar properties across a range of hierarchical spatial scales, i.e., a topological structure that can be re-scaled in simple ways from one scale to another [e.g., Hortonian or Tokunaga self-similar networks; see *Rodriguez-Iturbe and Rinaldo*, 2001]. Nevertheless, this might not be true in some basins. For instance in the MRB, geologic controls dating back to the post-glaciation period [*Ojakangas*, 1982; *Nicollet*, 1993] have imposed constraints on the landscape dissection, leaving behind river networks which do not always obey self-similar organization, resulting in different spatial organization and variability over some range of scales. Such a violation from self-

similarity thus intensifies the necessity of revisiting the scaling laws in these settings either in the form the landscape topography or river network topology.

The overall goal of this research was to understand and quantify the water cycle dynamics within small to large catchments and specifically decipher the time scales of transport and storage as a function of scale and catchment spatial heterogeneity, such that inferences on water quality can be made under changing conditions imposed by agricultural practices. To advance this goal, three main objectives were pursued: (1) develop a quantitative framework within which possible changes in the time scales of water cycle dynamics can be quantified, (2) investigate whether a spatially lumped system representation but dynamically variable (e.g., via a time-varying stochastic Lagrangian transport formulation) can properly capture the influence of within-catchment spatial heterogeneity into the transport time scales accounting for the catchment storage and mixing, and (3) quantify how external geologic controls might express themselves on river network topology, spatial heterogeneity of drainage patterns, and emergence of preferred scales of landscape dissection, which in turn can influence the transport and storage time scales at large-scale catchments with implications for solute transport and water quality.

This dissertation is organized as follows. Chapter 2 overviews the theory of time-variant travel time distributions (TTDs) within the StorAge Selection (SAS) function framework. In Chapter 3, a quantification of the TTDs during two periods of time, before and after LULC change in the Redwood River Basin, is presented. Via numerical simulations, Chapter 4 examines the ability of the time-variant TTDs to appropriately encapsulated within-catchment spatial heterogeneity, as well as explores the dependence of the mean travel time (MTT) on the hierarchical aggregation of network-structured spatial heterogeneity. Chapter 5 examines landscapes exhibiting spatial heterogeneity in their topologic branching structure (and thus deviation from self-similarity) via wavelet multi-scale analysis and synthesis, to identify and quantify scales of preferred

organization and relate them to the underlying geologic controls. Finally, Chapter 6 presents concluding remarks and perspectives on future research.

2

Theory of Time-Variant Travel Time Distributions

2.1. Travel Time Distribution (TTD) vs. Hydrologic Response

The difference between a catchment's hydrologic response and Travel Time Distribution (TTD) has been stressed by a number of studies [e.g., *Rodhe et al.*, 1996; *McGuire et al.*, 2005; *Heidbuchel et al.*, 2012]. The hydrologic response, controlled by the celerity of hydraulic potentials, reflects how fast a rainfall event is translated into discharge. In contrast, the TTD, controlled by the solute velocity, reflects the transport and aging of individual water particles during their travel in the catchment, which is time-variant and depends on the pore water velocity and history of prior precipitation and soil moisture [e.g., *McDonnell and Beven*, 2014]. Besides, the time scale of hydrologic response is often orders of magnitude smaller than the MTT of water because perturbations in the pressure head can advance much faster in the unsaturated soil profile than the transport of tracer or water particles through a catchment [*Kirchner et al.*, 2000; *Weiler et al.*, 2003; *Fiori and Russo*, 2008].

Due to the complex subsurface mixing mechanism and spatial heterogeneity in the preferential flowpaths, proper quantification of the TTD is important for a better

understanding and prediction of the water storage and solute transport in hydrologic systems [e.g., *McGuire et al.*, 2002; *Dusek et al.*, 2012; *Fiori and Russo*, 2013]. By using the concentration of a passive tracer or water stable isotope measured in the precipitation and streamflow, several studies have attempted to estimate the travel times by assuming and parameterizing a theoretical form for the TTD [see *McGuire and McDonnell*, 2006 and references therein for a comprehensive review on the catchment travel time modeling]. Such studies include investigating the role of topography [*McGuire et al*., 2005*; Braxton et al*., 2009; *Tetzlaff et al*., 2009a], soil hydrology [*Soulsby et al*., 2006; *Tetzlaff et al*., 2009b; *Troch et al*., 2013], climate [*Hrachowitz et al*., 2009; *Heidbuchel et al*., 2013], and geology [*Asano and Uchida*, 2012] on the mean travel or residence time by observation-based modeling. In many of these attempts, the assumed TTDs (such as the exponential or gamma distributions) are calibrated under the steady-state assumption, i.e., water storage and hydrologic fluxes in the catchment do not change over time. However, this consideration is insufficient to account for the antecedent soil moisture condition and the temporal dynamics of the physical processes such as precipitation and evapotranspiration, which are the primary sources of temporal variability and irregular shape of the TTDs. In addition to these first-order controls, preferential contribution of aged water in the soil storage to the outfluxes (such as discharge and evapotranspiration) plays a second-order control which is driven by the catchment physical properties and spatiotemporal distribution of (in)active flowpaths. The time-varying nature of the travel times is thus governed by both the temporal variability of the storage and hydrologic fluxes and the way different ages are sampled from the subsurface, which explains the distinction between different catchments in how they retain or release the water in storage.

Several time-varying approaches have been developed so far to address the time-variant feature of the TTDs and advance our understanding of the dynamic response of catchments [*Hrachowitz et al.*, 2010b; *Rao-Garcia and Weiler*, 2010; *Birkel et al.*, 2012; *McMillan et al.*, 2012; *Heidbuchel et al.*, 2012]. This study employs the recently

developed theory of time-variant TTDs within the StorAge Selection (SAS) function framework [*Botter et al.*, 2010, 2011; *Van der Velde et al.*, 2012; *Harman*, 2015; *Benettin et al*., 2015a] that explicitly accounts for the aforementioned major controls on the temporal dynamics of the TTDs.

2.2. Stochastic Lagrangian Formulation of Water and Solute Transport

2.2.1. Distinction between Travel and Residence Time Distributions

The theory of time-variant TTD has been developed based on the Lagrangian representation of a catchment, where the water and solute particles are tracked along their spatially heterogeneous hydrologic pathways (Figure 2.1). By conceptualizing the catchment as a single Control Volume (CV) and assuming that the loss to and/or the recharge from groundwater is negligible, the major fluxes closing the mass balance (Eq. (1)) for the water storage (S) in the CV are precipitation (P) as the only source of input, discharge (Q) at the outlet, and evapotranspiration (ET). The ET integrates the evaporation from the soil surface and the plant transpiration by accounting for the solar and terrestrial radiation, climatic attributes, plant type, and water availability.

$$\frac{dS(t)}{dt} = P(t) - Q(t) - ET(t) \tag{2-1}$$

Using the Lagrangian description of flow, the time at which a given water particle enters and exits the CV is represented by t_i and t_e, respectively. The travel time (t_T) is then defined as $t_T = t_e - t_i$, i.e., the time spent by the particle since its entrance into the CV at time t_i until it exits the CV at time t_e. Correspondingly, the partition function, $\theta(t_i)$, is defined as the fraction of those particles injected at time t_i that will eventually join the stream as discharge. Alongside the travel time, the age or residence time (t_R) of a particle is defined as the elapsed time since the particle entered into the CV, i.e., $t_R = t - t_i$.

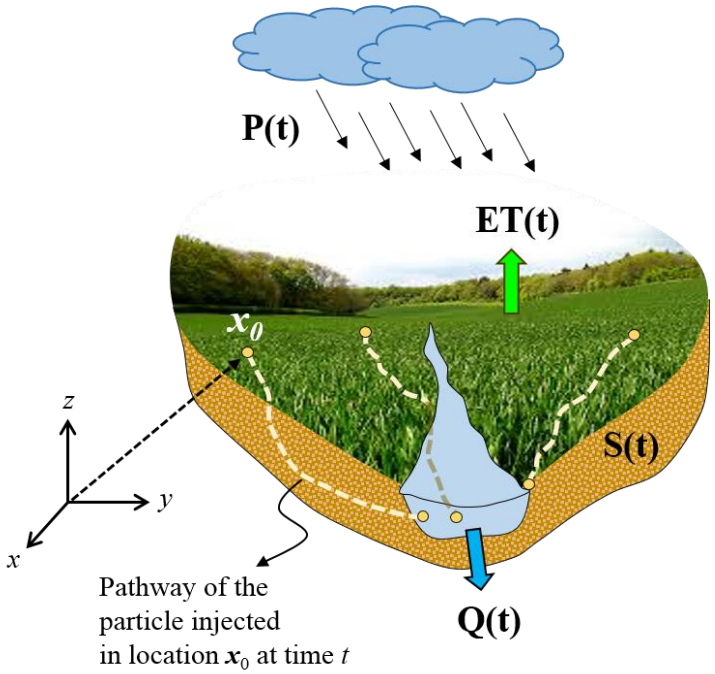

Figure 2.1. Schematic of the Lagrangian representation of a catchment. The catchment is considered as a single control volume assuming that the loss to and/or the recharge from groundwater is negligible, and the major fluxes closing the mass balance are the water storage (S), precipitation (P) as the only source of input, discharge (Q) at the outlet, and evapotranspiration (ET). Particles injected at the same time can have very different ages at the same location due to the spatial heterogeneity of the transport properties along their pathways.

Recently, *Benettin et al.* [2015a] provided a coupled description of transport processes using life expectancy and travel time. The life expectancy (t_E) [*Cornaton and Perrochet*, 2006] is the time a particle is expected to spend from the current moment until it reaches the outlet, i.e., $t_E = t_e - t$. Therefore, it can be immediately concluded that the travel time of a particle is a special case of its age and life expectancy, i.e., the travel time is the same as life expectancy at time of injection while it coincides with the residence time when evaluated at the exit time.

By keeping track of each water particle and recording the corresponding travel and residence times, three types of time-relevant distributions can be constructed to characterize the particles transport in the CV. The *residence time distribution* (RTD), $p_R(t_R, t)$, is the probability distribution function (pdf) of the ages of all particles that are still present in the CV at time t. The set of residence times existing in the CV changes as time progresses due to the disproportional entrance of zero-age particles and exit of older ones, thereby the residence time distribution varies in time as well. Depending on whether the particles are tracked forward or backward in time, TTDs can be defined in two separate ways. The *TTD conditioned on the injection time*, $p_T(t_T, t_i)$, or the *forward TTD* gives the pdf of the travel time of those particles that were injected into the CV at the same time t_i. On the other hand, the *TTD conditioned on the exit time*, $p'_T(t_T, t_e)$, or *backward TTD*, represents the pdf of the ages of particles sampled in the discharge at time t_e, no matter when they entered into the CV. It is worth mentioning that in general, the forward and backward distributions are not necessarily the same except under the steady-steady condition when the water storage is constant [*Niemi*, 1977; *Rinaldo et al.*, 2011]. Moreover, the backward distribution is always constrained by the residence time distribution since the ages of particles in the discharge at any given time have to be a subset of the ages available in the CV at that time.

2.2.2. Master Equation for the Residence Time Distribution (RTD)

If we assume some water particles were injected in the CV at time t_0, the probability that they reach location $\boldsymbol{x}$ at time t can be expressed by the stochastic displacement pdf. The displacement pdf is similar in form to the advection-dispersion model and obeys the Fokker-Planck equation [e.g., *Risken*, 1984]. Also, due to the spatially heterogeneous hydrologic pathways, particles in the same location at a given time can have very different ages. As such, the age distribution of particles residing in location $\boldsymbol{x}$ at time t can be characterized by the mass age density function [*Ginn*, 1999]. The linkage between the displacement and the mass age distribution functions [*Benettin et al.*,

2013a] constitutes the basis for the Master Equation [*Botter et al.*, 2011], describing how the age distribution of the particles evolves over time. The ME is expressed as

$$\frac{\partial(S(t)\,p_{RT}(t_R,t))}{\partial t} = -S(t)\frac{\partial(p_{RT}(t_R,t))}{\partial t_R} - Q(t)\,p'_T(t_R,t) - ET(t)\,p'_{ET}(t_R,t) \qquad (2\text{-}2)$$

where the left hand side of the above equation explains the temporal change of the water particles in storage having ages t_R at time t, and the right hand side consists of three terms responsible for the change of the age of water particles. The first term relates to the natural aging of the water particles as time progresses. The second term shows the fraction of the ages in storage that are sampled by Q at time t, and the third term is similar to the second one, but relevant to those ages leaving the CV at time t via ET.

2.3. StorAge Selection (SAS) Function

In order to solve for the RTD from the ME, an independent equation is written by relating the backward TTD and RTD through a function called the StorAge Selection (SAS) function.

$$p'_T(t_T,t_e) = p_{RT}(t_T,t_e)\omega_Q(t_T,t_e) \qquad (2\text{-}3)$$

$$p'_{ET}(t_T,t_e) = p_{RT}(t_{ET},t_e)\omega_{ET}(t_{ET},t_e) \qquad (2\text{-}4)$$

where ω_Q and ω_{ET} are the SAS function for discharge and evapotranspiration, respectively. These non-negative time dependent functions, i.e., ω_Q and ω_{ET}, essentially describe how different ages available in storage are preferentially sampled by the discharge or other form of out-fluxes. The SAS function thus integrates the effects of heterogeneity in flowpaths and dispersion mechanisms dictating the water and solute transport through a hydrologic system [*Benettin et al.*, 2013a; *Rinaldo et al.*, 2015].

Botter et al. [2011] introduced the first representation of the SAS function called the *age function* (or *absolute* SAS function), which is a function of the travel time, hence its shape might vary greatly from one catchment to another. For practical purposes, this

makes the comparison between different catchments challenging because they might span a completely different range of travel times, but follow a similar underlying mixing mechanism. To overcome this issue, *Van der Velde et al.* [2012] proposed the second generation of the SAS function called *Storage Outflow Probability* (*STOP*) *function* (or *fractional* SAS function), which is a function of the cumulative probability of the residence time distribution, $P_R(t_R, t)$, having a value between 0 (indicative of the youngest water particles) and 1 (indicative of the oldest water particles). The main advantage of the STOP function with respect to the age function is that the STOP function is a probability distribution integrating into 1 and thus can be parameterized by the existing theoretical distributions to simulate various types of the sampling mechanism [e.g., *Van der Velde et al.*, 2012, 2014]. *Harman* [2015] also proposed another form of such functions, named *ranked* SAS functions, which are expressed in terms of the ranked storage, i.e., $S_R(t_R, t) = P_R(t_R,t) \cdot S(t)$, rather than the cumulative probability of the residence times. Correspondingly, the ME can be reformulated by this ranked storage and the relevant ranked SAS function might be used as a tool to explicitly demonstrate the effect of the time-varying storage volume on the age selection. Availability of long time series of high resolution hydro-chemical data for input and output fluxes is necessary for inferring the appropriate form of the SAS function for a catchment of interest, which is usually a limiting factor in practical applications. Regardless of the challenges involved in calibrating the SAS function, when its appropriate form (constant or variable in time) is known for a catchment, the water and solute transport can be properly characterized in a stochastic way by the relevant residence and travel time distributions [*Rinaldo et al.*, 2015].

2.4. Analytical Solutions for the Travel and Residence Time Distributions

By substituting the backward distributions from Eq. (2-3) and (2-4) into Eq. (2-2), a quasi-linear partial differential equation is derived which can be solved analytically for the RTD, expressed as

$$p_{RT}(t_R,t)=\frac{P(t-t_R)}{S(t-t_R)} \tag{2-5}$$

$$.\exp\left\{\int_{t-t_R}^{t}\frac{Q(u)[1-\omega_Q(t_R-t+u,u)]-P(u)}{S(u)}du\right\}.\exp\left\{\int_{t-t_R}^{t}\frac{ET(u)[1-\omega_{ET}(t_R-t+u,u)]}{S(u)}du\right\}$$

Now, by inserting Eq. (2-5) into Eq. (2-3), the backward TTD is be derived as

$$p'_T(t_T,t_e)=\frac{P(t_e-t_T)\omega_Q(t_T,t_e)}{S(t_e-t_T)} \tag{2-6}$$

$$.\exp\left\{\int_{t_e-t_T}^{t_e}\frac{Q(u)[1-\omega_Q(t_T-t_e+u,u)]-P(u)}{S(u)}du\right\}.\exp\left\{\int_{t_e-t_T}^{t_e}\frac{ET(u)[1-\omega_{ET}(t_T-t_e+u,u)]}{S(u)}du\right\}$$

Finally, the governing equating of the forward TTD can be obtained with the help of another relationship known as the *Niemi*'s equation [1977], which is written as

$$Q(t)\,p'_T(t-t_i,t)=P(t_i)\theta(t_i)\,p_T(t-t_i,t_i) \tag{2-7}$$

The right hand side represents the fraction of water particles injected at time t_i leaving the CV via Q at time t, and the left hand side describes the fraction of the discharge sampled at time t composed of those particles entered at time t_i. By inserting Eq. (2-6) into Eq. (2-7), the forward TTD is derived as

$$p_T(t_T,t_i)=\frac{Q(t_i+t_T)\omega_Q(t_T,t_T+t_i)}{S(t_i)\theta(t_i)} \tag{2-8}$$

$$.\exp\left\{\int_{t_i}^{t_i+t_T}\frac{Q(u)[1-\omega_Q(u-t_i,u)]-J(u)}{S(u)}du\right\}.\exp\left\{\int_{t_i}^{t_i+t_T}\frac{ET(u)[1-\omega_{ET}(u-t_i,u)]-P(u)}{S(u)}du\right\}$$

As the explicit expressions show, the travel and residence time distributions are governed by (i) the temporal variability of the precipitation, evapotranspiration, discharge, and water storage in soil, and (ii) how the discharge and evapotranspiration

SAS functions dictate the distribution of ages sampled by Q and ET, respectively, from the ages available in S. Even if the SAS function is treated as time-invariant, these distributions are still time-variant as they are directly dependent on the temporal dynamics of the above fluxes.

In the context of the managed landscapes, it can also be recognized how the influence of altered soil hydrology and runoff generating mechanisms might be captured by the above controls on the TTDs. Transport through the artificial drainage systems, as strong preferential flowpaths, bypasses the complex dispersion in the subsurface resulting in water and solute delivery to the streams much faster than they might naturally move within the soil matrix. This is directly expressed in the SAS function (as the second-order control on the TTD) by giving higher preference to the younger water particles while sampling different ages in the soil storage during those times that the drainage system is active. On the other hand, quick removal of excess moisture from the shallow subsurface layer by the drainage system leaves more vacant space in the soil, which prevents overland flow generation (via allowing higher infiltration) and decreases the chance of evaporation. The resulting change in the balance between these hydrologic fluxes in such "engineered landscapes" is explicitly reflected in the TTD as a first-order control. Quantification of such change in the catchment TTDs undergone land-use land-cover (LULC) alterations will be further explored in Chapter 2.

3

Inferring Changes in Water Cycle Dynamics of Intensively Managed Landscapes via the Theory of Time-Variant Travel Time Distributions*

*Published as Danesh-Yazdi, M., E. Foufoula-Georgiou, D. L. Karwan, and G. Botter (2016), Inferring changes in water cycle dynamics of intensively managed landscapes via the theory of time-variant travel time distributions, *Water Resources Research*, 52, 7593–7614.

3.1. Summary

Climatic trends and anthropogenic changes in land cover and land-use are impacting the hydrology and water quality of streams at the field, watershed, and regional scales in complex ways. In poorly drained agricultural landscapes, subsurface drainage systems have been successful in increasing crop productivity by removing excess soil moisture. However, their hydro-ecological consequences are still debated in view of the observed increased concentrations of nitrate, phosphorus, and pesticides in many streams, as well as altered runoff volumes and timing. In this study we employed the theory of time-variant travel time distributions within the storage selection function framework to quantify changes in water cycle dynamics resulting from the combined climate and land-use changes. Our results from analysis of a sub-basin in the Minnesota River Basin

indicated a significant decrease in the mean travel time of water in the shallow subsurface layer during the growing season under current conditions compared to the pre-1970's conditions. We also found highly damped year-to-year fluctuations in the mean travel time, which we attribute to the "homogenization" of the hydrologic response due to artificial drainage. The dependence of the mean travel time on the spatial heterogeneity of some soil characteristics was further explored via numerical experiments, suggesting significant correlation between the mean travel time and the soil saturated hydraulic conductivity.

3.2. Introduction

Water cycle dynamics play a central role in the ecological and biogeochemical functioning of a watershed determining the water quality, sediment composition, and cycling of pollutants, nutrients, carbon, and nitrogen in its water bodies and floodplains. Human activities in recent decades have left their signatures on many watersheds around the world: from the contamination of the receiving water bodies due to nutrients, pesticides, and fine sediments [*Kladivko et al.*, 2001; *Kanwar et al.*, 2005; *Botter et al.*, 2006; *Schottler et al.*, 2014] to altered streamflow dynamics at many space and time scales [e.g., *Vörösmarty and Sahagian*, 2000; *Zhang and Schilling*, 2006; *Foufoula-Georgiou et al.*, 2015] to impaired aquatic systems [e.g., *Zedler et al.*, 2003]. One particular human activity of global interest is the intensification of agriculture for food and energy production [e.g., *Tilman et al.*, 2011; *Tscharntke et al.*, 2012; *Gelfand et al.*, 2013]. In the Midwestern U.S., the replacement of hay and small grains with row crops of corn and soybean since the 1970's [e.g., see Fig. 2 in *Foufoula-Georgiou et al.*, 2015] has been accompanied by expansion of artificial surface and subsurface drainage, and also conversion of forests and wetlands to agricultural lands [*Pavelis*, 1987; *Dahl et al.*, 2000; *Fraser and Fleming*, 2001]. In addition to human-induced landscape alterations, climatic trends in the Midwest have also been documented, especially following the mid-1970s with warmer temperatures, earlier snowmelt, increased annual precipitation,

and rainfall events of higher intensity and shorter duration [e.g., *Karl et al.*, 1996; *Groisman et al.*, 2004, 2012; *Villarini et al.*, 2011; *Higgins and Kousky*, 2013]. Acknowledging that both climatic trends and human actions modulate hydrologic change, which might cascade down to other environmental changes, the goal of this study is to provide a quantitative framework within which to study possible changes in the *time scales* of water cycling in the landscape before it is discharged to the streams. Changes in the time scales of water transport are important as they modulate changes in chemical and biogeochemical reactions affecting the quality of water entering the streams.

In agricultural landscapes with poorly drained soils and wet climate, a considerable portion of the water would remain undrained after a rainfall event. The resulting high soil moisture would impose stress on plants during the growing season by limiting the adequate aeration required for crop root development [*Spaling and Smit*, 1995]. Subsurface agricultural drainage systems can remove soil moisture above the field capacity, lowering the water table, reducing the excess water stress on plants, and allowing greater plant uptake of nutrients [*Zucker and Brown*, 1998; *Fraser and Fleming*, 2001] while at the same time facilitating earlier cultivation, orderly planting and harvesting, and timely tillage [*Jin et al.*, 2008]. However, several studies and long-standing debates discuss the direct and indirect effects of agricultural drainage (both surface and subsurface) from the hydrological, ecological, and economical viewpoints [e.g., see *Blann et al.*, 2009 and references therein]. For instance, nutrient loss due to subsurface drainage has been reported as a serious water quality concern in many regions [e.g., *Skaggs et al.*, 1994; *Tomer et al.*, 2003] mainly due to the potential to augment the loss of soluble nutrients and sediment by providing *extra pathways* for *fast* delivery of water and nutrients to streams [e.g., *Chapman et al.*, 2005; *Basu et al.*, 2011], as well as bypassing biological processes taking place in the riparian zone [e.g., *Clement et al.*, 2003].

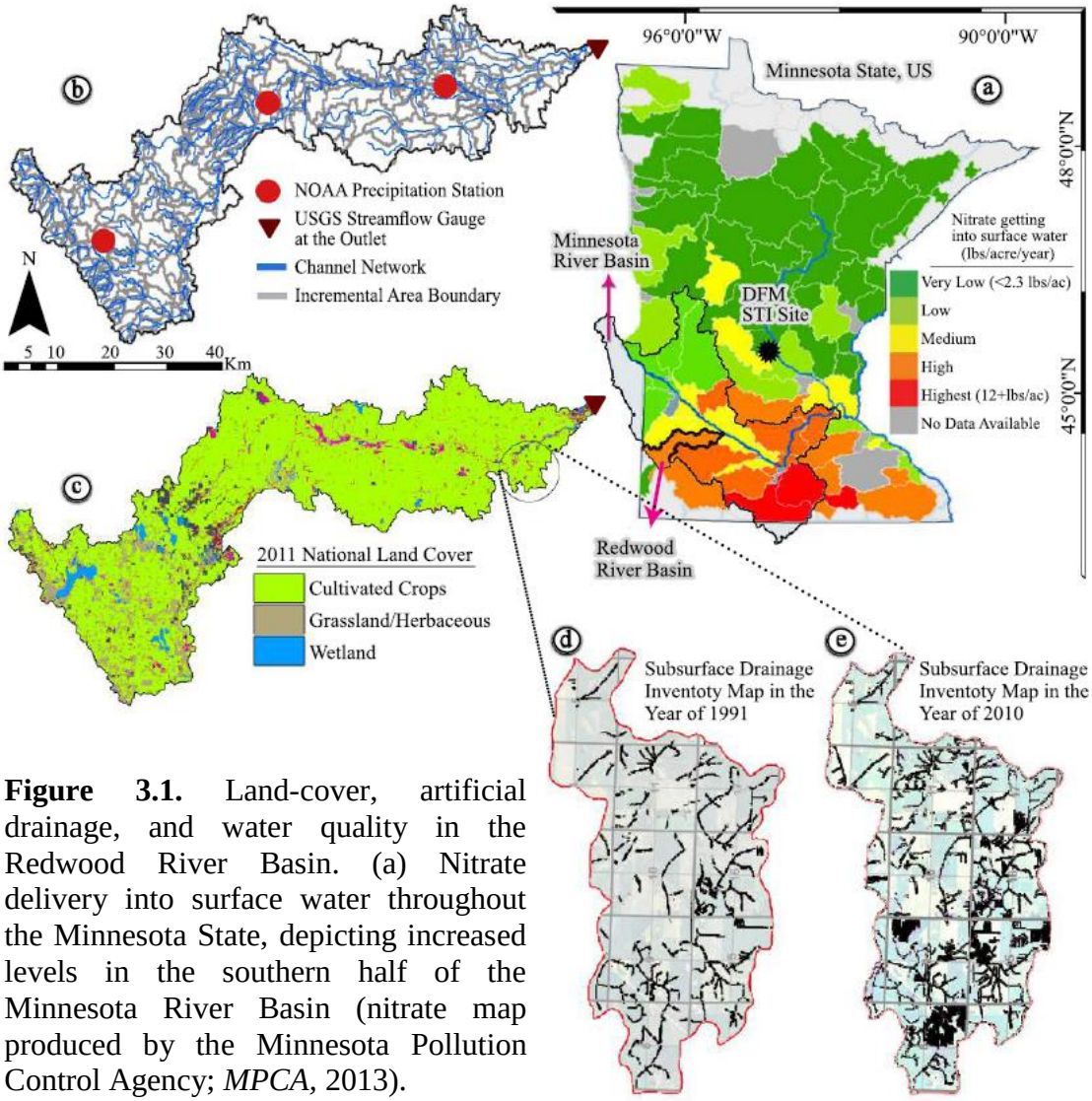

Figure 3.1. Land-cover, artificial drainage, and water quality in the Redwood River Basin. (a) Nitrate delivery into surface water throughout the Minnesota State, depicting increased levels in the southern half of the Minnesota River Basin (nitrate map produced by the Minnesota Pollution Control Agency; *MPCA*, 2013). (b) Map of the Redwood River Basin depicting channels and their incremental drainage areas. Daily precipitation data are available at three stations (Marshall, Vesta, and Tyler) marked with dots on the map and daily streamflow data are available at the outlet (USGS 05316500 Redwood River Station near Redwood Falls, MN). (c) 2011 National Land Cover cropped lands (depicted by green pixels). Cropland sources account for an estimated 89 to 95% of the nitrate load in the Minnesota River Basin [*MPCA*, 2013]. (d-e) Subsurface drainage inventory maps of a part of the Redwood county in the years 1991 and 2010, respectively (produced by the Minnesota State University, Water Resources Center). The total length of subsurface tiles has been more than doubled in two decades, increasing the tile drainage density from 2.90 km^{-1} in 1991 to 6.34 km^{-1} in 2010.

As an example, Fig. 3.1a depicts the nitrate delivery into surface water throughout the State of Minnesota, showing increased levels in the southern half of the Minnesota River Basin including the Redwood sub-basin. More than 80 percent of the delivered nitrate arises from the agricultural fields, and the elevated nitrate concentration in streams is partially attributed to the artificial drainage system, which is recognized as the most active pathway from cropland sources to streams [*Minnesota Pollution Control Agency* (*MPCA*), 2013]. Extensive installment of drainage systems has undoubtedly changed the water cycle dynamics and re-plumbed the subsurface structure by introducing extra flow pathways, making the landscape now respond differently compared to the pre-altered condition. However, the change in the time scale of water and nutrient transport in such managed landscapes is still poorly understood. Multiple approaches exist to estimate the water particles' travel times based on a linear system's response perspective, each with their own advantages and limitations. One widely-used approach relates catchment streamflow and precipitation tracer concentrations through a stationary convolution kernel with a pre-defined shape (e.g., exponential, gamma) representing the steady-state Travel Time Distribution (TTD) of that catchment. This method requires hydro-chemical data that are seldom available for direct calibration of the TTD [e.g., *Hrachowitz et al.*, 2011] and the data should also be of high frequency for a long period of time so that the tail of the TTD (signifying long-term catchment behavior) can be appropriately estimated [*Seeger and Weiler*, 2014; *Kirchner*, 2016]. Second, spatially distributed physical models with mechanistic or semi-empirical parameterizations of all water transport pathways have been developed to track the water particles through a spatial domain and compute their travel times [e.g., *Fiori and Russo*, 2013]. However, such models are often computationally expensive and might suffer from the well-known equifinality problem as they include a large number of parameters which are not directly observable and need to be calibrated with limited data. In this study, we employ a third model type: a lumped, stochastic Lagrangian formulation of transport [e.g., *Botter et al.*, 2011; *Van der Velde et al.*, 2012; *Harman*, 2015] to estimate the probabilistic structure

of TTDs by using the available hydrologic data measured at the watershed scale to best infer how water particles with different ages in storage are preferentially sampled by the discharge. The promise of this approach for such a study lies in its potential to incorporate the influence of exogenous factors that can significantly impact the TTDs, such as the LULC change considered here. Our analysis brings forward the possibility that a reduced complexity framework informed by real watershed conditions can provide insight on water cycle changes and prompt further data collection and analysis. Such insight provides a departure point for understanding nutrient cycling based on the residence times of water in the landscape. We emphasize that this study is not intended to estimate the real travel times in our specific catchment by performing a goodness of fit to any particular time series. Instead, the goal is to infer a first-order estimate of the *relative changes* in travel time statistics in those landscapes undergoing substantial alterations in LULC.

The rest of this chapter is organized as follows. Section 3 describes the study site and data used in the analysis. A seasonal parameterization of the SAS function is proposed in section 4 to acknowledge the different mechanisms at play during the winter, snowmelt, growing, senescence, and fall periods, and a quantification of the TTDs during two periods of time: 1944-1976 (before LULC change denoted by BLUC) and 1976-2007 (after LULC change denoted by ALUC) is presented. Section 5 further investigates the dependence of the Mean Travel Time (MTT) to the soil saturated hydraulic conductivity via numerical simulations. Finally, section 6 concludes by summarizing the important findings.

3.3. Study Area and Data

3.3.1. Climate and Land-Use

The 1821 km^2 Redwood River Basin (44°33′ N, 95°40′ W) is one of the main sub-basins of the Minnesota River Basin located in the Upper Midwestern U.S. (Fig. 3.1a). The

basin, which ranges from 253 m to 608 m above sea level in elevation, is underlain by Cretaceous sedimentary rocks and consists of soils that are primarily loamy sand within the Quaternary glacial till with scattered sandy outwash and silty alluvium on flood plains. The erodibility is moderate over the majority of the basin, having a complex mixture of well and poorly drained soils [*USDA-NRCS*, 2015]. The climate is continental with dry cold winters and wet warm summers. The average monthly temperature at the Redwood Falls over the 1944-2007 period fluctuates between -15.6°C in January and 16.4°C in July. The mean annual precipitation is 658 mm, more than 60% of which normally falls from May through September and there is almost no snow on ground during May-September. The average annual runoff is about 82 mm, and evapotranspiration is a sizable component of the annual water budget estimated to be approximately 80-90 percent of the total precipitation [e.g., *MPCA*, 2007].

Agriculture is the main land use in this basin where approximately 82% of the total available area in 949 farm lands consists of row crops [Fig. 3.1c]. The cropping pattern has been significantly changed since 1940's with increasing rate of corn and soybean cultivation, currently covering nearly 86% of the cropped lands, while small grains, hay, and grasslands constitute the rest of the balance [*USDA*, 2015; see also Fig. 3.2a in *Foufoula-Georgiou et al.*, 2015]. Artificial subsurface drainage is a common practice in this basin where the total length of subsurface tiles has been more than doubled in two decades (Figs. 3.1d and 3.1e), increasing the tile drainage density (i.e., total length of tiles divided by the drainage area) from 2.90 km^{-1} in 1991 to 6.34 km^{-1} in 2010. Analysis of precipitation and streamflow data for the Redwood basin indicates that daily precipitation statistics have not changed significantly in the ALUC period except for increased daily rainfall amounts during November-February, while daily streamflow has increased consistently in all months. Moreover, Copula analysis of the daily rainfall and streamflows reveals sharper rising limbs of streamflow hydrographs and stronger dependence on the previous-day precipitation during the growing season of May-June, which has then been attributed to non-climatic effects such as the extensive installment

of surface diches and subsurface drainage tiles over the years in this watershed [*Foufoula-Georgiou et al.*, 2015].

3.3.2. Hydro-Climatic Variables for Water Balance

In order to compute the TTDs, we need daily hydro-climatic data over our entire study period (1944- 2007) including precipitation (rainfall and the water equivalent of any type of frozen precipitation), discharge, and evapotranspiration. The daily precipitation at three available National Oceanic and Atmospheric Association (NOAA) stations, namely Marshall (GHCND: USC00215204), Vesta (GHCND: USC00218520), and Tyler (GHCND: USC00218429) for the 1944-2007 period is averaged to obtain a single precipitation signal for the basin, and the daily streamflow data are available at the USGS 05316500 Redwood River Station near Redwood Falls, MN (Figs. 3.1b and 3.2a). The daily evapotranspiration is estimated as

$$ET(t) = RET \times K_c \times K_w(t) \tag{3-1}$$

where *RET* is the daily reference evapotranspiration estimated using the Penman-Monteith method [*Allen et al.*, 2005], K_c is the crop coefficient, and K_w is the water availability coefficient. *RET* is estimated by using the minimum and maximum temperatures measured at the same NOAA stations, but due to the lack of long-term solar radiation, wind speed, and dew point temperature datasets, the available data at the nearest stations in the Minnesota River Basin are used as surrogate for these climatic variables. Corn, soybean, and hay are considered as dominant crops to compute K_c, and the percentage of total area cultivated by these crops each year is also taken into account. The duration of each plant's different growing stages accompanied by the corresponding crop coefficients are chosen as those recommended by *Hinck* [2008] for Southern Minnesota. The crop planting and harvesting time during the study period is determined based on the data provided by *Cardwell* [1982] and the U.S. Department of Agriculture, National Agricultural Statistical Service [*USDA*, 2015].

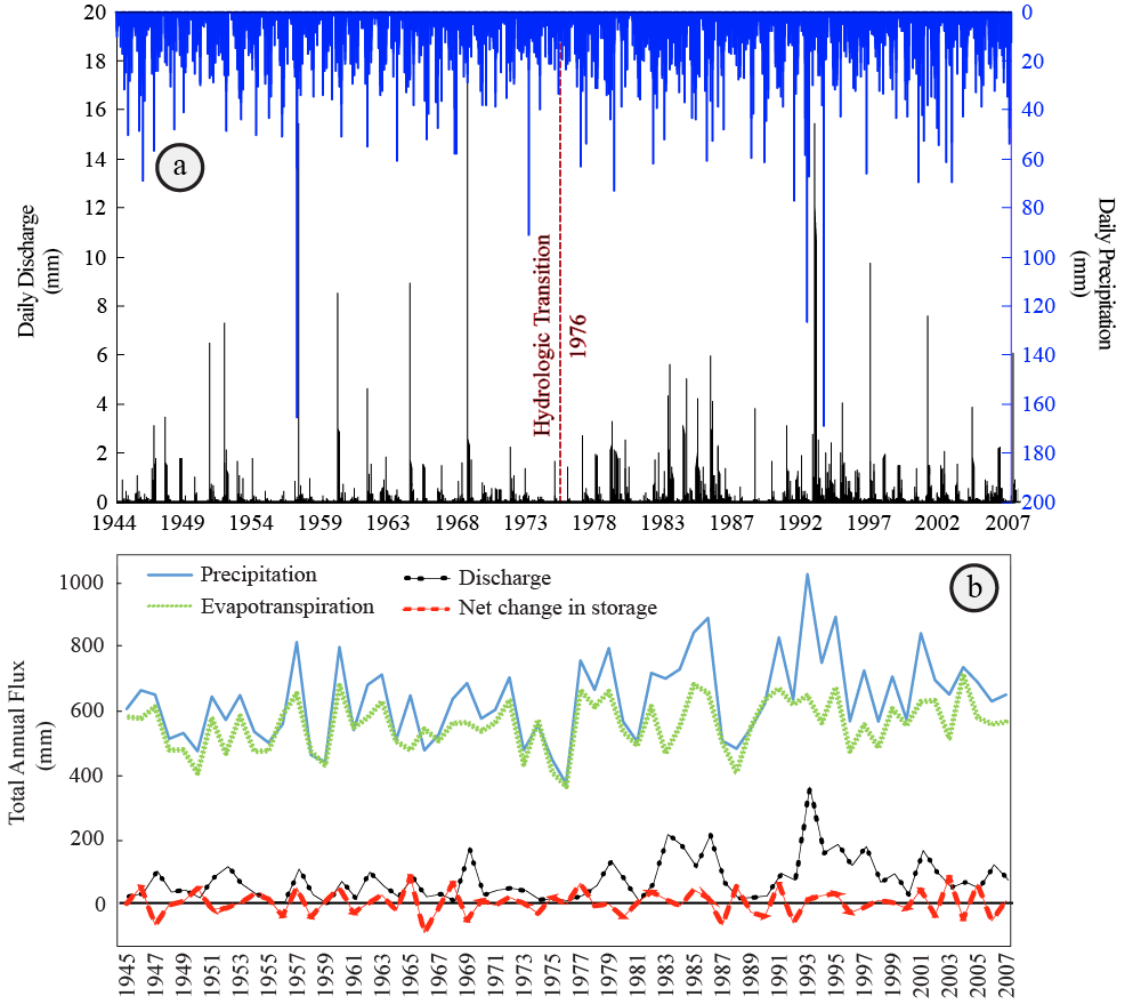

Figure 3.2. Hydrologic change in the Redwood River Basin. (a) Daily precipitation and streamflow time series for the Redwood basin from 1944 to 2007 with the hydrologic transition year of 1976 marked (see text). (b) Annual series of observed precipitation and streamflow and estimated evapotranspiration (see text) together with annual mass balance expressed as net change in storage.

The crop planting time should be properly included to make sure evapotranspiration is turned on at the right time of a year. This affects our analysis because evapotranspiration can play a key role on restricting the fraction of the water particles joining the streamflow, thereby affecting the TTDs via the partition function. The data presented by

Cardwell [1982, Table 1] was used to assign the corn planting time between 1930's and 1979. The source of this information was the State and Federal Crop and Livestock Reporting Service publications, Soil Conservation Service statistics and USDA Fertilizer Situation reports. According to this data, the corn planting time did not appreciably change from 1930's to mid-1960's. It started on May 21th and then shifted to May 13th and 11th during 1960's and 1975-1979, respectively (note that these dates are averages over the relating period). After 1979, the corn planting time was determined based on the data provided by the USDA, Statistical Service [*USDA*, 2015]. Similarly, the harvesting time can be extracted from the same database, and the duration of different growing stages is set to those recommended by *Hinck* [2008] for the Southern Minnesota. The planting/harvesting time is reported for the whole Minnesota State (rather than for separate sub-basins or counties) when certain percentages of these operations are complete across the State. For instance, beginning dates indicate when planting or harvesting is about 5 percent complete and ending dates show when operations are about 95 percent complete. Fig. 3.3a illustrates the temporal change in the average planting time when 10, 30, and 75 percent of the whole State of Minnesota is planted by corn. The common observation from all curves is the overall decreasing trend in the planting time revealing the effectiveness of the subsurface drainage system in facilitating earlier planting, while the fluctuations obviously arise from different climatic conditions from one year to another affecting the suitable time for planting. For our analysis, we choose the curve showing the average planting time when 30 percent of the agricultural lands are planted because the planting time in 1979 shown by this curve is close enough to the one reported by *Cardwell* [1982]. In addition, since the Redwood basin is located in the southern third of the Minnesota reaching warm temperature earlier than the northern regions, it is reasonable to consider this basin among those 30 percent areas in the State where the soil temperature gets high enough so that planting can be initiated. Having extracted the planting and harvesting times using the above information, the crop coefficient curve can then be constructed for each water year,

separately. Figure 3.3b shows the corn coefficient curve corresponding to two example water years 1956 and 1998 in the BLUC and ALUC periods, respectively, showing 17 days shift to earlier planting time from the water year of 1956 to 1998.

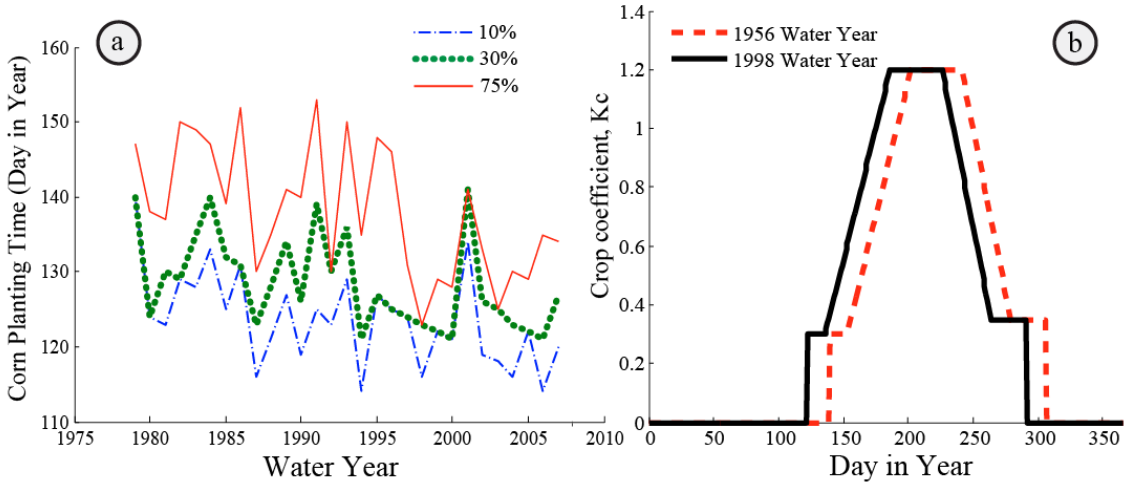

Figure 3.3. Temporal change in the corn planting time and crop coefficient curve. (a) Corn planting time (day of the year) in the 1979- 2007 period. The trend to earlier planting times is attributed to the effectiveness of the subsurface drainage system to drain the soil. The fluctuations in the planting time arise from different climatic conditions from one year to another affecting the suitable time for planting. (b) Corn coefficient curve corresponding to two example water years 1956 and 1998 in the BLUC and ALUC periods, respectively, showing 17 days shift to earlier planting time from the water year of 1956 to 1998 with nearly the same total annual precipitation depths.

Ultimately, K_w is computed by using the empirical relationship proposed by *Holmes and Robertson* [1963] as

$$K_w(t) = \begin{cases} 1 & s(t) > s_{fc} \\ 0 & s(t) < s_{wp} \\ \dfrac{\ln\left(100\left(\dfrac{s(t)-s_{wp}}{s_{fc}-s_{wp}}\right)+1\right)}{\ln(101)} & s_{wp} < s(t) < s_{fc} \end{cases} \tag{3-2}$$

where $s(t)$ is the soil moisture content, and s_{wp} and s_{fc} are the moisture content at the wilting point and field capacity, respectively. s_{wp} and s_{fc} are set to 0.11 and 0.31, respectively, which are typical for loamy sand soils [*Laio et al.*, 2001]. Starting with an initial $s(t)$, $K_w(t)$ and the soil storage $S(t+1)$ are computed dynamically via solution of the mass balance equation (i.e., $dS(t)/dt = J(t) - Q(t) - ET(t)$) and Eq. (3-2), respectively at a daily time step. The storage in a unit area of the shallow subsurface layer is equal to the product of the soil moisture content, soil porosity (set to 0.42 as the soil in the Redwood basin is mostly loamy sand), and the depth over which the soil storage is considered (set to 1.2 m which is the distance between the soil surface and the typical depth of drainage tiles being installed in this basin). It is noted that the assumed initial value for soil moisture content does not affect the results as its effect is dissipated after about ten months and our analysis is performed over periods of approximately 64 years.

To provide confidence in our estimation of the daily evapotranspiration, we computed the annual change in storage as shown in Fig. 3.2b, which indicates that the long-term average of the year-to-year fluctuations is very small (i.e., 1.08 mm) and no systemic trend is present in these fluctuations. Furthermore, average annual evapotranspiration constitutes 88 percent of the average annual precipitation (with a standard deviation of ±9.7 percent), which is in accordance with the previously reported budget for the Redwood basin by the *MPCA* [2007]. We also studied the sensitivity of the estimated *RET* to the air temperature, solar radiation, and wind speed. By changing these climatic variables each at a time by ±20 %, the wind speed showed the smallest influence on the

estimated long-term average daily *RET*, followed by the solar radiation and air temperature. The percent change in *RET* by varying the wind speed, solar radiation, and air temperature in the above range was (0.69, −0.61), (1.19, −4.98), and (2.48, −8.41), respectively.

3.4. Quantifying the Change in the Mean Travel Time (MTT)

The residence and travel time distributions are computed from Eq. (2-5, 2-6, and 2-8) for the 1944-2007 period by using the daily time series of the hydrologic fluxes discussed in section 3, as well as the SAS functions parameterized by characterizing how water particles with different ages in the subsurface contribute to the discharge and evapotranspiration. For the Redwood river basin, it was established in *Foufoula-Georgiou et al.* [2015] that 1975-1976 marked a year of significant hydrologic change partially impacted by tile drainage as inferred from simultaneous analysis of land cover data and localized multi-scale decomposition of daily precipitation and corresponding streamflow time series using wavelets (see Fig. 3.2a).

3.4.1. Parameterization of the StorAge Selection (SAS) Function

3.4.1.1. Qualitative Inference of the Type and Form of the SAS Functions

Availability of high resolution hydro-chemical data series for input and output fluxes is indispensable for determining the appropriate form of the SAS functions that describe the underlying sampling schemes of water ages in storage by the outfluxes [*Van der Velde et al.*, 2014; *Harman*, 2015; *Queloz et al.*, 2015; *Benettin et al.*, 2015b]. Due to the lack of hydro-chemical data in the Minnesota River Basin, however, direct estimation and calibration of the SAS function is infeasible. We use knowledge of hydrologic fluxes at daily time scales including precipitation, direct subsurface tile flow, soil moisture, and temperature data to construct representative and justifiable approximations of the sampling mechanism at different periods within a year in the BLUC and ALUC periods. This approach is described below for the Redwood basin.

For the evapotranspiration SAS function, the random sampling scheme (ω_{ET} = 1) is assumed for both the BLUC and ALUC periods, consistent with documented *ET* age sampling formulations in basins with wet climatic conditions [*Van der Velde et al.*, 2014]. However, different types of the discharge SAS functions (ω_Q) are assumed for the BLUC and ALUC periods and also during distinct seasons of the year to account for various sampling schemes of those water particles leaving the system as discharge, depending on the climatic condition, loss due to evapotranspiration, and soil moisture dynamics. To infer the form of the discharge SAS function (ω_Q) in the ALUC period, we used hydrologic data from the 11.41 hectare monitoring site, ST1, near the Redwood basin (see Fig. 3.1a) operated by the Discovery Farms Minnesota (DFM) program, where 15-minutes measurements of subsurface tile drainage flow and soil moisture are available. By mutual comparison of the precipitation, subsurface tile drainage discharge, and soil moisture time series, some inferences about the mixing processes in the subsurface root zone layer are made, which then help to parameterize the SAS functions. Figure 3.4 shows these data for the water year 2013, which are representative of the data available for other water years (2012-2015) with respect to runoff ratio, planting and harvesting times, and the period over which drainage from tiles was observed.

1. *Winter season* (*December-March*): According to the temperature data, the soil surface is almost always frozen during December-March and precipitation accumulates as snow. Since the excess soil moisture was already removed by the drainage tiles prior to freezing and no new water can infiltrate into the subsurface, streamflow during this season does not consist of water particles draining from the shallow subsurface layer. This is consistent with the observation showing that the soil moisture is much less than the field capacity and no direct subsurface tile drainage is recorded during this period (Fig. 3.3b). Thus the discharge SAS function in these months is formulated such that higher preference is given to the older particles.

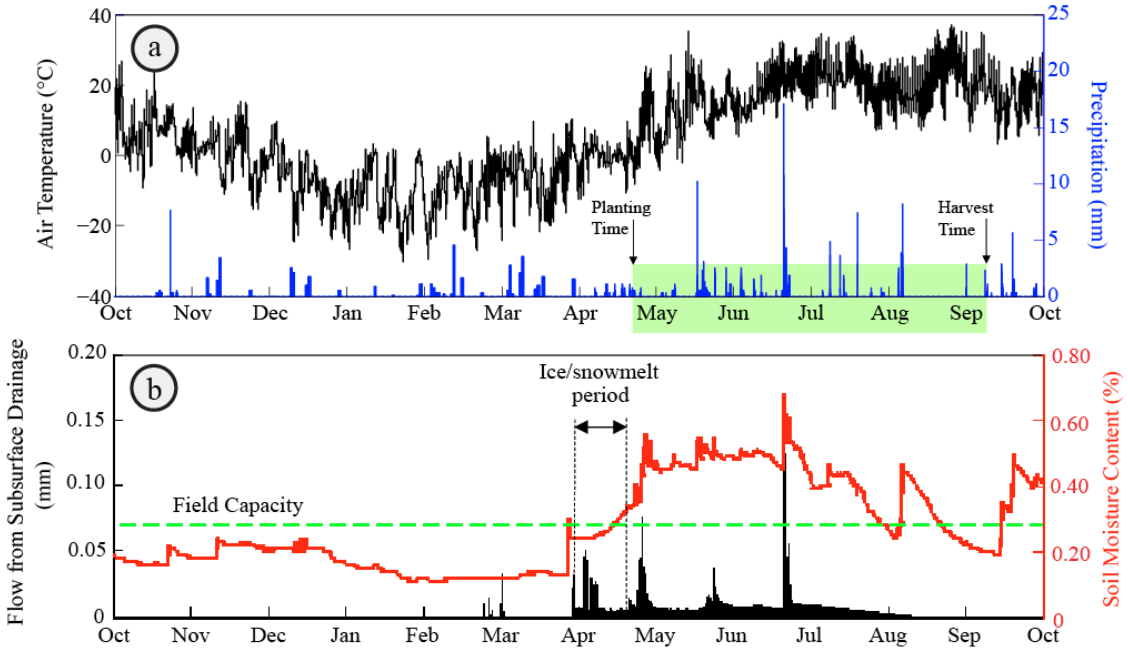

Figure 3.4. Detailed data at the 11.41 hectare Discovery Farms Minnesota experimental site Stearns (ST1) near the Redwood basin used to parameterize the SAS function displayed in Fig. 3.5. (a) Precipitation and air temperature, and (b) subsurface drainage flow and soil moisture content for the water year 2013. All data were measured in 15 minute increments, except precipitation from November to April that is not available at this site and the daily data shown above were obtained from the nearest National Weather Service station.

2. *Snowmelt season* (*April*): Shortly after the snowmelt begins (usually in April depending on the climatic condition and lasting for at most three weeks), the soil moisture gradually increases until it goes beyond the field capacity and the subsurface tiles start draining water from the soil, which includes a mixture of new and pre-stored water particles. Therefore, the random-sampling scheme is considered for this season.

3. *Growing season* (*May-July*): The major contribution to streamflow from subsurface tile drainage is observed in May, June, and July when the subsurface has large capacity for water storage as inferred from its high soil moisture above

field capacity (see Fig. 3.3b), resulting in a high contribution of young or fast flushed-out event-based water particles to streamflow. Comparing the chemographs and streamflow hydrographs in other tile-drained agricultural systems also indicate macropore flow quickly carries event water and water-borne chemicals to the receiving tile drainage networks under similar conditions [e.g., *Richard and Steenhuis*, 1988; *Gall et al.*, 2011]. Thus, a SAS function with higher preference to the younger ages is assumed for this season.

4. *Senescence season* (*August*): In August, the soil moisture is relatively high, but not as high as the May-June-July period because the soil moisture in excess of field capacity has already been removed by the drainage system as well as the growing crops' transpired water. Thus the soil has available volume for water storage, and less tile drainage is observed from the subsurface system compared to May, June, and July, prompting us to assume a SAS function with equal likelihood of age sampling.

5. *Fall season* (*September–November*): Lastly, during September-November, the soil moisture gradually decreases and almost no discharge is observed from the drainage system, except in those times experiencing very intense rainfall events. Thus a SAS function with preference to the older ages is selected for this season, but the preference is smaller than that for the winter season because the water particles entering from the new precipitation still have the chance to mix with the pre-stored particles.

3.4.1.2. Quantitative Parameterization of the SAS Functions

To convert the qualitative forms of the SAS functions discussed above into quantitative expressions, we follow the approach proposed by *Van der Velde et al.* [2012] in which the SAS function is quantified in terms of the cumulative probability of the residence times. Since the cumulative distribution function takes values between zero and one, a

typical parameterization of the SAS function is via the Beta distribution with shape parameters α and β. In this work, we assume time-invariant SAS functions where the parameter β is set to 1 for all seasons during both the BULC (pre-1975) and ALUC (post-1975) periods to ensure a monotonic shape for the beta distribution so that the SAS function gives preference to only one type of sampling ages, i.e., no simultaneous high preference is given to both young and old particles, which would not be physically realistic. This is consistent with the shape of the SAS functions inferred from long-term hydro-chemical datasets in highly monitored settings [e.g., *Harman*, 2015; *Benettin et al.*, 2015b]. The parameter α, however, has to be determined for all seasons and for both the BLUC and ALUC conditions.

Let us denote by i = 1, 2, 3, 4, 5, the winter, snowmelt, growing, senescence, and fall seasons respectively and by $j(i)$ the indices of the months belonging to season i, that is, for season i = 1 (winter: December to April), $j(i)$ = 12, 1, 2, 3. The parameters α_i^{BLUC} and α_i^{ALUC} are determined by solving the following optimization problem:

$$\textit{Minimize:} \qquad \sum_{k\in j(1)} \left| MTT_k^{BLUC} - MTT_k^{ALUC} \right| \tag{3-3}$$

$$\textit{Subject to:} \qquad b_{i=1,\ldots,5}^{BLUC,} = 1,\ b_{i=1,\ldots,5}^{ALUC} = 1 \tag{3-4a}$$

$$\alpha_{i=2,4}^{ALUC} = 1,\ 1 < \alpha_{i=1,5}^{ALUC} < 2,\ 0 < \alpha_{i=3}^{ALUC} < 1,\ \alpha_{i=5}^{ALUC} < \alpha_{i=1}^{ALUC} \tag{3-4b}$$

$$\alpha_{i=1}^{BLUC} = \alpha_{i=1}^{ALUC},\ \alpha_{i=2,\ldots,5}^{BLUC} = \alpha_{i=5}^{ALUC} \tag{3-4c}$$

We note that α = 1 indicates a random sampling scheme, while α < 1 and α > 1 gives preference to young and old particles, respectively, as inferred qualitatively in the previous section. In essence, the above objective function (3-3) treats the transport mechanism during "winter" (season i = 1) as a constraint for the estimated MTTs. Indeed, since 1) subsurface drainage tiles are inactive during winter, and 2) the soil is frozen, hence the input precipitation (consisting of zero-age particles) has no chance to

be mixed with the pre-stored water from last season(s), the mixing properties (SAS function) and the transport time scales (MTT) in the shallow subsurface layer are assumed to be the same during the BLUC and ALUC conditions. The solution of the above constrained optimization problem results in $\alpha_{i=1}^{ALUC}=1.6$, $\alpha_{i=3}^{ALUC}=0.5$, $\alpha_{i=5}^{ALUC}=1.4$ and the corresponding SAS functions are shown in Fig. 3.5b.

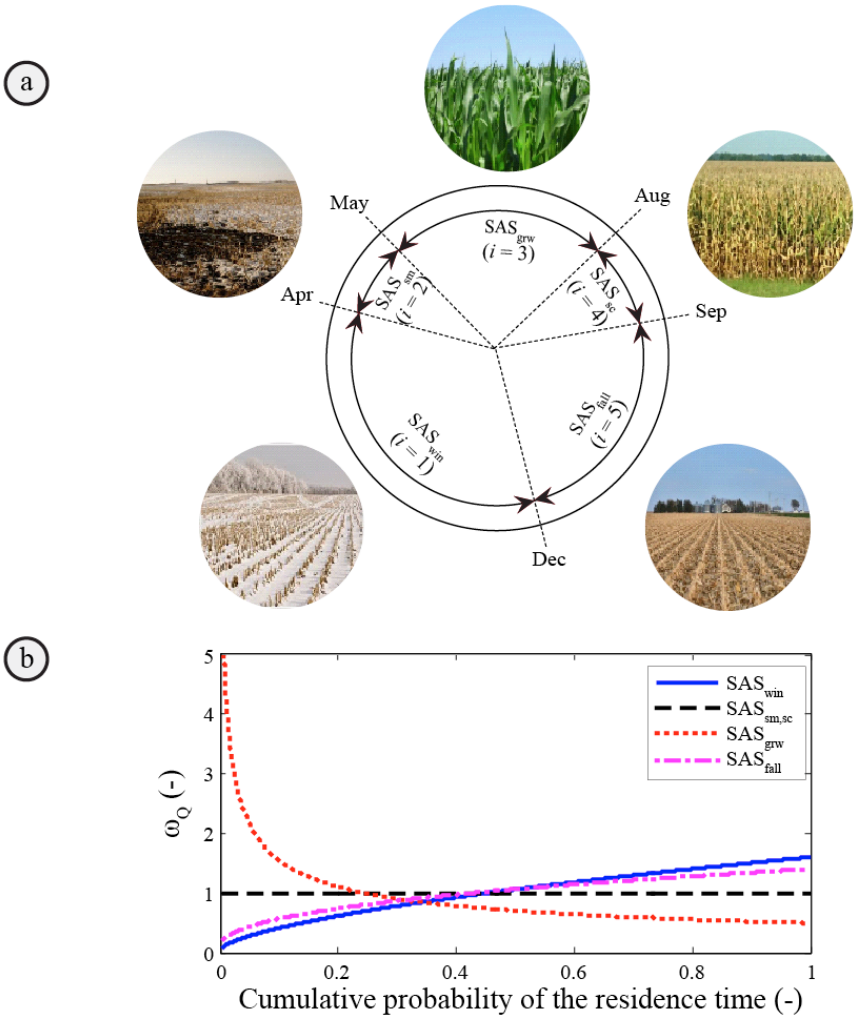

Figure 3.5. Parameterization of the StorAge Selection (SAS) function. (a) Qualitative inference of the type and form of the SAS functions for five distinct seasons in a year. SAS_{win}, SAS_{sm}, SAS_{grw}, SAS_{sc}, SAS_{fall} represent the SAS functions corresponding to the winter (i = 1), snowmelt (i = 2), growing (i = 3), senescence (i = 4), and fall (i = 5)

Figure 3.5 (continued) seasons, respectively. (b) Parameterized SAS functions as a Beta density function with parameters α and β. The parameter β was set to 1 for all seasons during both the BULC (pre-1975) and ALUC (post-1975) periods to ensure a monotonic shape for the beta distribution so that the SAS function gives preference to only one type of sampling ages. In the ALUC period, the parameter α was set to 1 in the snowmelt and senescence seasons (i.e., $\alpha_{i=2,4}^{ALUC}=1$) to enforce a random sampling scheme, while during the winter, growing, and fall seasons α was determined by solving a constrained optimization problem given in Eqs. (3) and (4), resulting in $\alpha_{i=1}^{ALUC}=1.6$, $\alpha_{i=3}^{ALUC}=0.5$, $\alpha_{i=5}^{ALUC}=1.4$ (see text for details).

To gain insight into the sensitivity of the MTTs to the assumed parameters of the SAS functions, we examined two extreme conditions, each giving preference to only young and only old particles, respectively, at all times in the ALUC period. The MTTs could increase (decrease) by 50 percent by switching from the seasonally parameterized SAS functions to the ones giving high preference to only old (only young) particles throughout the year. However, these are extreme and not physically meaningful parameterizations since they do not acknowledge the considerable within-year variability and are not consistent with the tile drainage observations of Fig. 3.4b. As a final remark, it should be noted that because the parameterized SAS functions are not expressed in terms of the residence time itself, the residence time distribution cannot be directly computed from the given analytical expressions and the Master Equation (ME) (see Eq. (2-2)) must be solved numerically. The chosen time step to update the storage while solving the mass balance equation (through a forward difference scheme) should be fine enough to achieve accurate computation of residence time probabilities. This is because the ME involves the ratios between the precipitation, discharge, evapotranspiration fluxes and storage, and if these fluxes are large enough compared to the storage, coarse time steps will result in significant numerical errors. It can be simply shown that the numerical solution of the ME using hourly time step suffices to avoid such an issue, which decreases the numerical error by two orders of magnitude compared to the daily time step.

3.4.2. Temporal Evolution of the Travel Time Statistics

By using the daily precipitation, evapotranspiration, discharge, and soil storage fluxes and parameterizing the SAS functions, the residence and forward travel time distributions are computed at a daily scale. Figures 3.6c and 3.6d show examples of such distributions conditional on time t_1: Sep. 13th-1974 and t_2: June 16th-1993, belonging to two periods with dry and wet hydrologic conditions, respectively (Figs. 3.6a and 3.6b). For each case, the impact of rainfall intermittency is clearly reflected in the non-smoothness of the TTDs, and the location of the peaks follows that of the discharge time series. There is also a remarkable difference between these two forward TTDs with respect to the shape, number of peaks, and the obtained range of the travel times. For instance, Figs. 3.6c and 3.6d show that the water particles injected at time t_2 resulted in much smaller travel times than those injected at time t_1, mainly explained by the underlying climatic and antecedent soil moisture conditions. This can be better understood by zooming into the discharge time series during the time interval around times t_1 and t_2 (Figs. 3.6a and 3.6b). The plots reveal that the rainfall event at time t_2 was both preceded and followed by wet periods leading to early peaks in the forward TTD, whereas a relatively long dry period after time t_1 resulted in a much later peak in the corresponding TTD. This illustration thus demonstrates how the temporal dynamics of the precipitation and discharge time series are translated into the temporal variability of the TTDs. In addition to the forward TTDs, the residence time distributions conditional on the same times t_1 and t_2 are also shown in Figs. 3.6c and 3.6d, respectively, to highlight the remarkable difference between these two distributions. First, in contrast to the forward TTDs, the residence time distributions, $p_R(t_R, t)$, contain gaps at those ages when $J(t - t_R) = 0$. Second, their temporal evolution follows the temporal dynamics of the precipitation time series. The tail of the residence time distribution, e.g. conditional on time t_2, is also three times longer than the tail of the forward TTD conditional on the same time, resulting in quite different mean residence and mean travel time.

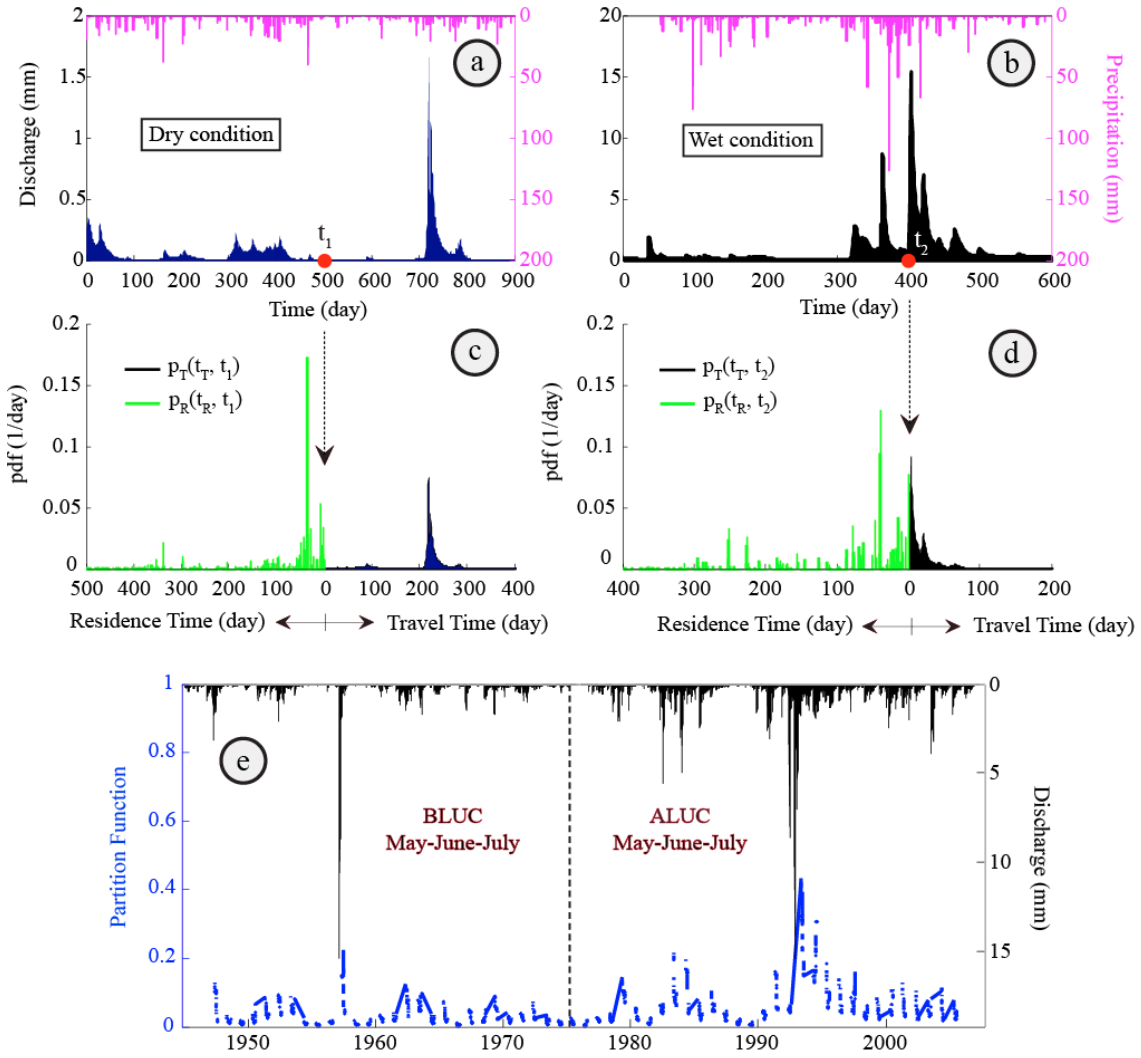

Figure 3.6. Residence and forward travel time distributions conditional on two times (t_1 and t_2) with different hydrologic conditions. (a-b) Observed precipitation and discharge time series around time t_1 (Sep. 13th-1974) and t_2 (June 16th-1993) under dry and wet conditions, respectively. (c-d) The forward travel time distributions, $p_T(t_T, t_i)$, conditional on the injection times t_1 and t_2, show remarkable differences with respect to the shape, number of peaks, and the estimated range of the travel times. The residence time distributions, $p_R(t_R, t)$, conditional on the same times t_1 and t_2 are also shown to highlight how the travel and residence time distributions can be considerably different. (e) Partition function versus daily streamflow for the months of May, June, and July. The plot shows how the temporal evolution of the partition function follows that of the streamflow, while the increased partition function in the ALUC period is obvious compared to the BLUC one. BLUC (ALUC) denote the pre- (post-) 1975 periods.

Figure 3.6e further depicts the computed partition function versus the streamflow time series for the months of May, June, and July, when the drainage system greatly contributes to discharge. The partition function can be analytically derived by setting the integral of the forward TTD to 1 (see Appendix B in *Botter et al.* [2010]). Not surprisingly, the temporal evolution of the partition function is governed by the discharge time series as the partition function at a given time gives the fraction of the injected water particles at that time leaving the system through discharge. However, the increased partition function in the ALUC period, compared to the BLUC period, is obvious (recall that the partition function ranges between 0 and 1), which is attributed to the increased discharge draining into the streams due to the subsurface drainage system.

Travel time statistics can also be tracked over time to infer how they have been changing from the BLUC to the ALUC period. Knowing the TTDs, the marginal TTDs as descriptors of the typical behavior of the system are then computed for each month by ensemble averaging the individual forward TTDs over that month from 1944 to 2007. Figure 3.7a shows the temporal evolution of the mean, median, 20^{th} and 80^{th} percentiles of the travel time for the month of June during the time window of the BLUC and ALUC periods. Time-averaged MTT has decreased by 41 percent from 77 days during the BLUC period to 45 days in the ALUC. This is interpreted as the result of the subsurface drainage providing faster pathways through which the drainable water (defined as the water corresponding to the soil moisture between the field capacity and saturation) can be quickly transported into the streams. The drainable water may include both the pre-stored water particles and the newly entered ones by most recent events, thereby the residence time of such particles would decrease while transported through the drainage system, resulting in the arrival of younger water particles to the streams compared to the undrained condition. Moreover, this plot depicts that in most years in the ALUC period the distance between the mean, and 20^{th} and 80^{th} percentiles of the travel time (especially the 80^{th} percentile) is smaller than that in the BLUC period, revealing significantly reduced variability in the travel times around the MTT. Mutual

comparison of the TTDs between BLUC and ALUC periods (see Figs. 3.6c and 3.6d for an example) also demonstrates that the TTDs during the ALUC period are more asymmetric in shape and show considerable shorter tail than those in the BLUC period.

Figure 3.7b, showing the differences of MTT between consecutive years, further demonstrates that the year-to-year MTT fluctuation in the ALUC period is also much smaller compared to that of the BLUC period, implying that the system has been hydrologically "homogenized" by the subsurface drainage system and responding in a more constrained or engineered way. Indeed, subsurface drainage basically provides a condition for a more uniform system response by reducing the degree of importance of the natural variability in key hydrologic processes such as groundwater table fluctuations or variations in the unsaturated hydraulic conductivity. The homogenization of the landscape by the artificial drainage systems has been already discussed by *Basu et al.* [2011] and the above observation is consistent with the findings of *Schilling and Helmers* [2008] who explored the effect of drainage on the baseflow and stormflow portion of the hydrographs as well as the characteristics of the streamflow recession after storm events. By analyzing the recession part of the hydrographs from heavily drained and less drained regions in Iowa and performing some model simulations, they concluded that the master recession curve (that is, the streamflow recession plotted against time on a semi-logarithmic scale) in intensively drained watersheds appears to indicate a linear relationship between storage and discharge compared to the less drained watersheds. This suggests that intensive subsurface drainage in such watersheds has led to the homogeneity in the dominant flow paths, resulting in a more predictable hydrologic response [*Boland-Brien et al.*, 2014]. These conclusions are also in accordance with the findings in *Foufoula-Georgiou et al*. [2015] where it was shown that the inherent non-linearity of the daily streamflow time series in the ALUC period was considerably reduced compared to the BLUC, attributed again to a more "regularized" hydrologic response of the re-plumbed landscape.

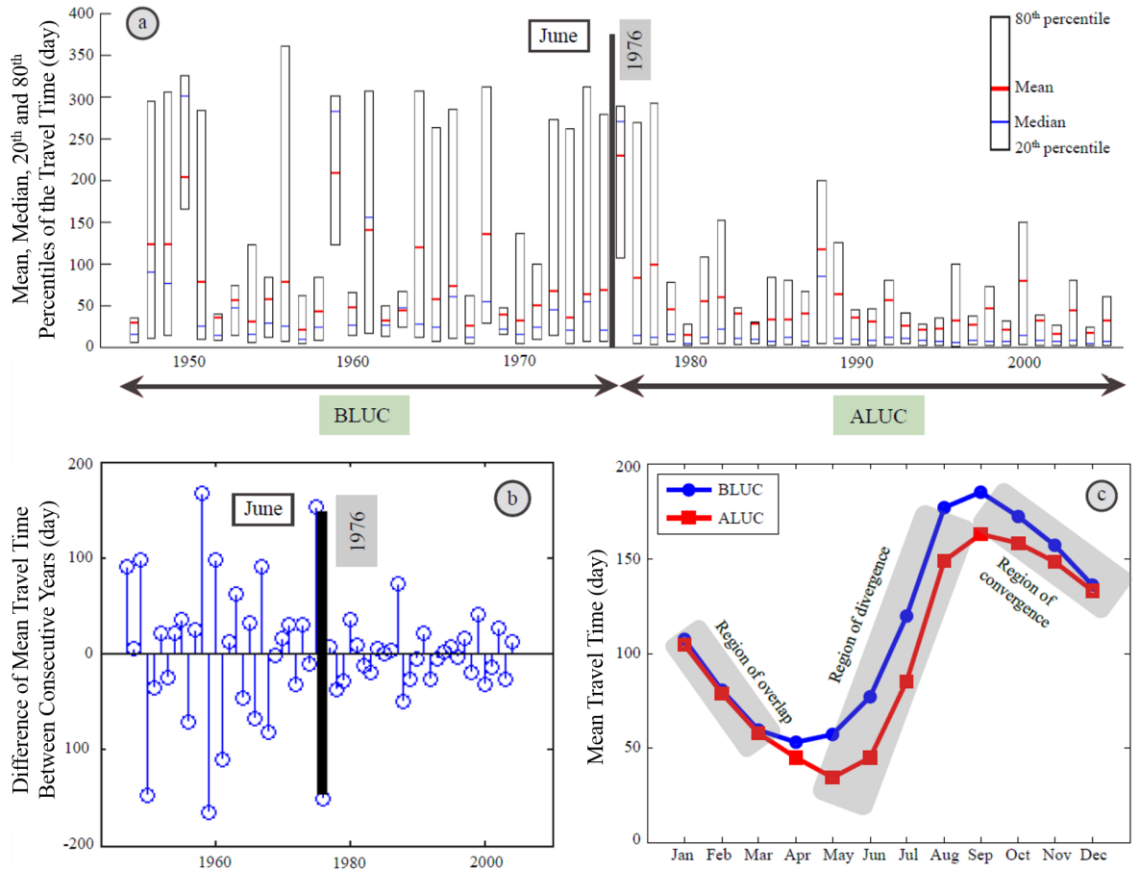

Figure 3.7. Temporal evolution of the travel time statistics and intra-annual variation of the mean travel time (MTT). (a) Mean, median, 20th and 80th percentiles of the travel time in the month of June. The time-averaged MTT indicates a reduction of 41 percent from 77 days during BLUC to 45 days in the ALUC period. Smaller distance between the mean, and 20th and 80th percentiles of the travel time in the ALUC period reveals significantly reduced variability in the travel times around the MTT. (b) Difference of MTT between consecutive years depicting the reduced year-to-year variation of the MTT in the ALUC period. (c) Seasonal pattern of the MTT during BLUC and ALUC periods. The ALUC curve does not exceed the BLUC curve in any month. The curves coincide during the months of December, January, February, and March, consistent with our parameterization of the SAS functions which assume that the subsurface drainage system plays a minimal role in the subsurface transport during these months. Starting in April, the curves start deviating from each other while the highest difference between them shows up during the months of May to August. From September on, the effect of subsurface drainage on discharge diminishes, resulting in the gradual convergence of the BLUC and ALUC curves. BLUC (ALUC) denote the pre- (post-) 1975 periods.

3.4.5. Seasonal Variation of the Mean Travel Time (MTT)

Figure 3.7c shows the seasonal variation of the MTTs for the BLUC and ALUC periods. Some interesting features are apparent in this figure. First, both curves show an overall cyclic shape during a year which is consistent to the similar behavior found by *Heidbuchel et al.* [2012] who also obtained a sinusoidal shape for the intra-annual variation of the MTT. Second, the ALUC curve does not exceed the BLUC curve in any month. An overlap of the curves during the months of December, January, February, and March (winter season) is consistent with our parameterization of the SAS functions which assumes that the drainage system during these months plays a minimal role in the subsurface transport and, in fact, this condition formed a major component of the constrained parameter estimation problem (see Eqs. 3-3 and 3-4). Third, the MTT curves begin to deviate from each other starting in April, i.e., at the beginning of the snowmelt period, with the ALUC curve remaining below the BLUC during the whole year, with the highest difference between them during the months of May to August. From September on, the effect of the drainage system on discharging water from the subsurface diminishes, resulting in the gradual convergence of the BLUC and ALUC curves. Substantial decrease in the MTT during the wet period (i.e., May-June-July), when the soil moisture exceeds the field capacity leading to drainage from subsurface tiles, might have serious implications for the water quality of the streams as the drainage system bypasses riparian buffers [*Schilling et al.*, 2015], contributing to the environmental degradation of surface waters due to eutrophication [*Ayars and Evans*, 2015].

The range of the estimated MTTs for the Redwood basin is small compared to the MTTs obtained for many other basins by using tracer or stable isotope measurements [e.g., see *McGuire and McDonnell*, 2006, Table 1]. This is partially because the MTTs were estimated by considering only the mixing processes that take place in the root zone layer, and not in the deep groundwater zone. The groundwater contribution to the travel

times can be incorporated by using other approaches such as a double-storage model [*Benettin et al.*, 2013b, 2015b]. This approach partitions the total storage into the shallow subsurface and deep groundwater layers, enabling us to compute the TTDs for each layer, separately, which obviously results in much longer MTTs corresponding to the groundwater layer. However, the focus of this study was only on the transport features taking place in the root zone layer because the subsurface drainage tiles are essentially beneath this zone (and above the groundwater table), cutting off the soil top layer from the deeper zone. In addition, a few recent studies [*Kirchner*, 2009, *Birkel et al.*, 2011, *Benettin et al.*, 2015b] have also shown that the chemical response of a watershed can be considerably influenced by another storage component, referred to as residual (or passive/dead/hidden) storage, which is not hydrologically active and can result in residence times that are much longer compared to the residence times of particles belonging to dynamic storage. This is an important consideration for the transport of reactive chemicals, nitrogen, and phosphorous in the agricultural watersheds but unfortunately, it cannot be incorporated except in the presence of hydro-chemical data. We understand that neglecting the residual storage, as considered in this study due to the lack of hydro-chemical data, can largely impact the absolute value of the estimated MTTs. However, since the residual storage is not influenced by the dynamical hydrologic fluxes and does not directly contribute to the streamflow [*Fenicia et al.*, 2010; *Soulsby et al.*, 2011], it is assumed that this portion of the total storage is not affected by the LULC change in the Redwood basin and consequently, it does not impact the relative difference between the estimated MTTs in the BLUC and ALUC periods.

3.5. Dependence of Mean Travel Time (MTT) on Soil Saturated Hydraulic Conductivity at the Hillslope Scale

Our analysis in the previous section considered the whole basin as a lumped control volume and used the available hydrologic data at the basin outlet to estimate the MTTs.

This approach did not explicitly take into account the spatial heterogeneity that is present in river basins, e.g., due to the spatially variable soil saturated hydraulic conductivity (K_{sat}). Moreover, the estimated MTTs might be very different from those that could be estimated from basins of smaller spatial scales if data were available. The goal of this section is thus to explore the sensitivity of the MTT to the spatial heterogeneity of soil characteristics that affect the mixing and transport of water and solutes throughout a catchment.

To this goal, a series of numerical simulations from hillslope to watershed scale were performed using a stochastic soil moisture model (see *Laio et al.* [2001] for a detailed expression of the model), which is based on the soil water balance of a hillslope in terms of precipitation, evapotranspiration, discharge, and water storage in the soil, and only considers the root zone dynamics. Daily rainfall is simulated as a Poisson process with the arrival rate λ (1/day), i.e., the average daily rainfall inter-arrival time (consecutive dry days separating rainy events) is $1/\lambda$ (day), and the daily rainfall depth is sampled from an exponential distribution with mean, γ (mm). Evapotranspiration is assumed to linearly increase with the soil moisture content, i.e., $ET(t) = ET_{max}\,(s(t) - s_{wp})/(s_{fc} - s_{wp})$, where the parameters ET_{max}, s_{fc}, and s_{wp} are assumed depending on the considered basin and soil type [see e.g., *Laio et al.*, 2001]. By assuming that the vertical flow is driven by gravity, the discharge is approximated to be proportional to a power of the soil water storage, $Q(t) = K_{sat}\, s(t)^c$ [*Brutsaert and Nieber*, 1977], where the exponent c depends on the soil type and can be determined by using the available look-up tables [e.g., *Laio et al.*, 2001, Table 1]. For the sake of simplicity, a uniform SAS function (i.e., random sampling scheme) for both Q and ET is chosen while computing the TTDs.

In these simulations, the Redwood basin is first decomposed into single channels and their corresponding 315 hillslopes by using the National Hydrography Dataset (NHDPlus2 released in 2012), where the hillslope or the incremental area is defined as the area draining directly into its connecting channel [see Fig. 3.1b]. The root zone

depth, average daily rainfall depth, and average rainfall inter-arrival time are set to 1000 mm, 20 mm, and 6.6 days, respectively. The mean of the log-normal distribution from which K_{sat} is randomly generated is set to 350 mm/day and the variance is chosen such that it gives a set of bounding real-world values for K_{sat}, ranging from ~100 mm/day for clay to ~2000 mm/day for sand. Given the above parameters, the model is run for each hillslope during a time window of 20 years and the forward TTDs are then computed using the fluxes corresponding to that hillslope. Figure 3.8a shows the temporal variation of the MTT versus injection time for two hillslopes with minimum and maximum K_{sat}. The hillslope with the smallest K_{sat} gives higher travel times due to slow transport of water through the soil. On the contrary, MTTs relating to the hillslope with the maximum K_{sat} are much smaller as higher hydraulic conductivity facilitates rapid movement of water in the hillslope. The MTTs corresponding to all the other hillslopes (not shown here) fall between these two extreme bounds. Spatial heterogeneity of the soil K_{sat} at the hillslope scale also results in significant variation of the MTT. By time-averaging the MTT relating to each hillslope, Fig. 3.8b shows an emergent relationship between average MTT and hillslope K_{sat}. For K_{sat} less than nearly 600 mm/day, a power law relationship (R^2 = 0.98) governs, while a linear relationship (R^2 = 0.99) holds for K_{sat} larger than 600 mm/day. A linear variation of the average MTT with relatively large K_{sat}'s (relating to loamy sand and sandy soils) can be explained as follows. As mentioned earlier, drainage from a hillslope varies as a power of water storage with the proportionality coefficient, K_{sat}, and the exponent that is dependent on the field capacity, with drainage taking place when the soil moisture exceeds the field capacity. On the other hand, the soil field capacity also decreases with increasing K_{sat}, with the rate of decrease highly dampened when K_{sat} is larger than ~ 500 mm/day (e.g., see Table 1 in *Laio et al.* [2001]). This suggests that when the soil K_{sat} is larger than a threshold, the resulting discharge from a hillslope is mainly governed by K_{sat} and becomes less dependent on the interplay between the field capacity and soil moisture, which in turn is reflected in the TTDs as they are strongly controlled by the hydrologic fluxes. The

power law dependence of MTT on K_{sat} for K_{sat} less than 600 mm/day is harder to analytically explain as discharge is non-linearly dependent on both K_{sat} and field capacity and the emergence of such a relationship requires further study.

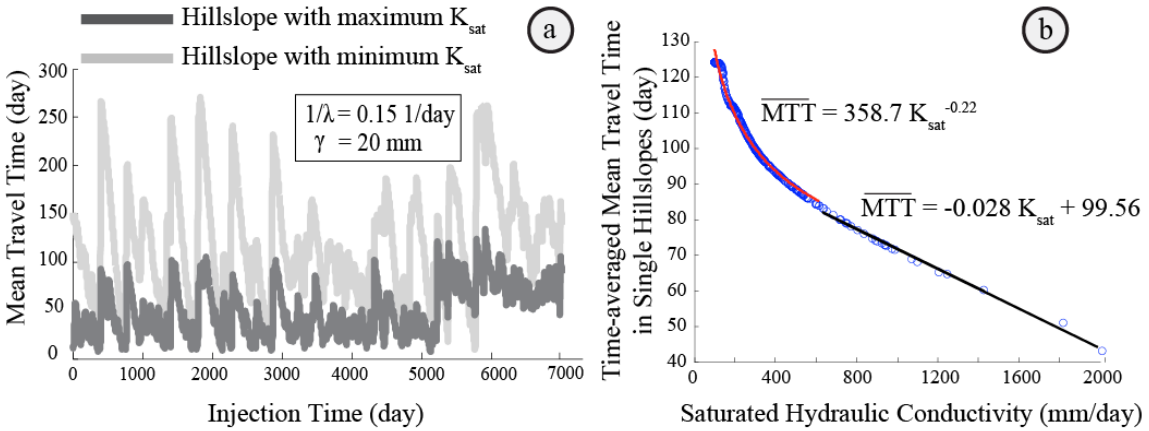

Figure 3.8. The effect of soil saturated hydraulic conductivity (K_{sat}) and spatial scale on the mean travel time (MTT). (a) MTT versus injection time for two hillslopes with minimum and maximum K_{sat}, and also for the whole basin scale. The overall basin MTT was computed as the integration of the MTTs of the nested sub-basins along the river network. (b) Time-averaged MTT versus soil K_{sat}, approximated by power law and linear relationships for soil saturated hydraulic conductivity less than and larger than 600 mm/day, respectively.

Strong correlation between the MTT and the spatial heterogeneity of soil properties at the hillslope scale motivates us to further explore the dependence of MTT on larger spatial scale to understand how spatial heterogeneity controls the MTTs estimated at hierarchical spatial scales of a basin. This is important since hydrologic and stream chemistry data are typically not available at plot scale but at much larger scales integrating the effects of the transport dynamics at the smaller scales of the watershed. Therefore, the answer to the above question would provide insight on the reliability of

the assessment of a catchment's behavior based on the data collected at the basin scale. This issue will be discussed in detail in Chapter 3.

3.6. Conclusions

The purpose of this study was to quantify the impact of climate and land-use land-cover (LULC) change, particularly the effect of extensive agricultural subsurface drainage, on the water cycle dynamics of intensively managed landscapes employing the theory of time-variant Travel Time Distributions (TTDs) within a stochastic Lagrangian transport formulation. By applying the methodology to the Redwood River Basin in the Midwestern U.S., where extensive expansion of subsurface tile drainage and a change in the daily hydrologic response have been documented in the post-1975 period, the following conclusions are made:

1) Travel time analysis showed that the Mean Travel Time (MTT) has considerably decreased post-1975, compared to the pre-1975 period, during all months with the maximum reduction during the growing season (e.g., reduction by 41 percent in the month of June). This is attributed to the intensification of tile drainage that can effectively extract the excess soil moisture from the subsurface by providing extra pathways through which water is delivered to the streams much faster compared to the natural transport within the soil matrix.

2) The year-to-year variability of the MTT was also found to be highly reduced in the presence of extensive subsurface tile drainage, indicating that the "filtering" of the natural heterogeneity via the artificially re-plumbed landscape results in a time-space homogenization of the hydrologic response and an overall system that responds to climatic variability in a more predictable way.

3) The spatial heterogeneity of the soil properties, e.g., saturated hydraulic conductivity (K_{sat}), was found to strongly affect the MTTs at the hillslope scale. For K_{sat} less than

nearly 600 mm/day, a power law relationship (R^2 = 0.98) was found between the MTT and K_{sat}, while a linear relationship (R^2 = 0.99) holds for K_{sat} larger than 600 mm/day.

Overall, our work puts forth the hypothesis that aspects of internal landscape plumbing can be estimated with hydrologic time series data in the absence of hydro-chemical data in spite of the uncertainty in the estimation of the StorAge Selection (SAS) functions. Even with increased collection of hydro-chemical data and higher spatial resolution of these data due to advances in remote-sensing technology, such hydro-chemical data cannot be historically reconstructed where they did not exist. Our study provides one approach to examine the relative effect of land use and other landscape changes based on more widely- and historically- available data. Specifically, even if the absolute values of the travel and residence times is not possible to obtain accurately, the detection and physical interpretation of system changes resulting from climatic and/or human alterations might still be feasible. Altered water pathways, and especially shortened residence time of water in the natural soil matrix, can have significant impacts on biochemical processes and thus water quality of the receiving streams. Thus, further work and data will be required to refine our analysis and interpretations.

4

Accounting for Catchment Spatial Heterogeneity via a Time-Variant Lagrangian Transport Formulation to Estimate Water and Solute Travel Time Distributions*

*Under Revision in *Geophysical Research Letters* as Danesh-Yazdi M., G. Botter, and E. Foufoula-Georgiou, Accounting for Catchment Spatial Heterogeneity via a Time-Variant Lagrangian Transport Formulation to Estimate Water and Solute Travel Time Distributions.

4.1. Summary

Lack of hydro-bio-chemical data at subcatchment scales necessitates adopting an aggregated systems approach for estimating water and solute transport properties, such as residence and travel time distributions, at the catchment scale. In this work, we show that within-catchment spatial heterogeneity, as expressed in spatially variable discharge-storage relationships, can be appropriately encapsulated within a lumped time-varying stochastic Lagrangian formulation of transport. This time (variability) for space (heterogeneity) substitution yields mean travel times (MTTs) that are not significantly biased to the aggregation of spatial heterogeneity under different sampling assumptions. Despite the significant variability of MTT at small spatial scales, there exists a characteristic scale above which the MTT is not impacted by the aggregation of spatial

heterogeneity. Extensive simulations of randomly generated river networks reveal that the ratio between the characteristic scale and the mean incremental area is on average independent of river network topology and the spatial arrangement of incremental areas.

4.2. Introduction

Developing detailed hydrologic models with a large number of parameters might explain some physical processes of interest at the field scale provided that enough observations are available for attribution of cause and effect. However, how to upscale information from the field scale to the catchment scale is still a challenge both in terms of effective parameterizations and in using available observations. For example, accounting for the within-catchment spatial heterogeneity to accurately estimate water and solute transport properties, such as residence and travel times, requires high-quality, high spatio-temporal resolution hydrologic, chemical, or isotopic data over prolonged periods of time that are rarely available [e.g., *Hrachowitz et al.*, 2011; *Birkel and Soulsby*, 2015]. Besides, how to find lumped system representations that allow for accurate estimation of whole catchment behavior without explicitly incorporating the small-scale heterogeneity also remains a challenge [e.g., *Young*, 2003; *Kirchner*, 2006].

The effect of within-catchment spatial heterogeneity on the catchment-scale travel time distribution (TTD) has been underestimated (if not neglected) in several studies by treating the whole catchment as a single homogeneous system and assuming a steady-state pre-defined shape (e.g., exponential or gamma) for the underlying TTD [see *McGuire and McDonnell*, 2006 and reference therein]. Such a consideration is not satisfying because (i) TTDs are nonstationary due to the temporal variability of hydrologic fluxes [e.g., *Rinaldo et al.*, 2011] and the fact that the temporal variation of their statistics might be slaved to the overall system dynamics [e.g., *Danesh-Yazdi et al.*, 2016], and (ii) even if time-invariant TTDs (e.g., exponential distribution in the simplest case) are assumed for the incremental areas (IAs) of a catchment, as the aggregation of

IAs takes place, the shape of the combined TTD would be quite different from the TTDs of any of the individual IAs.

In this work, we seek to examine the ability of the theory of time-variant TTDs [*Botter et al.*, 2010, 2011; *van der Velde et al.*, 2012; *Benettin et al.*, 2015b; *Harman*, 2015] to accurately predict the catchment transport properties in the absence of within-catchment observations. In particular, this study explores the following questions: (1) Can a lumped system representation via the stochastic Lagrangian transport formulation, which does not demand explicit characterization of within-catchment spatial heterogeneity, properly capture the influence of this spatial heterogeneity into the transport time scales expressing the system storage and mixing?; (2) Is the shape of the TTD at an aggregated scale physically consistent with the structured spatial heterogeneity of the combining IAs?; and (3) What is the dependence of the TTD on the network-structured spatial heterogeneity as the hierarchical aggregation of IAs takes place, and does a characteristic spatial scale exist above which the MTT becomes independent of the spatial heterogeneity of IAs? If so, what controls its magnitude?

4.3. Methods and Assumptions

4.3.1. Generation of Spatially Heterogeneous Catchments

Let w denote a catchment composed of two or more IA_i's, $i = 1,\ldots, N$, that are connected via a river network topology (Figure 4.1a). We use the Tokunaga self-similar (TSS) model to represent the river network topology, that is, we assume that $T_k = ac^{k-1}$ where T_k is the average number of branches of order j per branch of order $(j+k)$, and a and c are positive parameters (see, e.g., *Zanardo et al.* [2013] for a recent review and extensive analysis of TSS trees in the context of river networks). Let l_i, g_i, and b_i represent the length, gradient, and width of the channel corresponding to IA_i, respectively. We assume that the drainage area of the IA_i, i.e., DA_i, follows an exponential distribution with mean λ, that is, $f(DA_i) \sim exp\ (1/\lambda)$, and g_i and b_i are assumed to obey the typical scaling

relationships for fluvial networks, i.e., $g_i \sim A_i^{-0.30}$, $b_i \sim A_i^{0.35}$ [e.g., *Rodríguez-Iturbe and Rinaldo*, 2001], where A_i is the total upstream area of the outlet of the IA_i. If L_i is the length of the longest stream from the outlet of IA_i to its most upstream catchment divide and we assume Hack's law, i.e., $L_i \sim A_i^{0.55}$ [*Hack*, 1957], the channel length l_i can then be hierarchically computed through the river network. Using the above procedure, spatially heterogeneous catchments of arbitrary order can be generated.

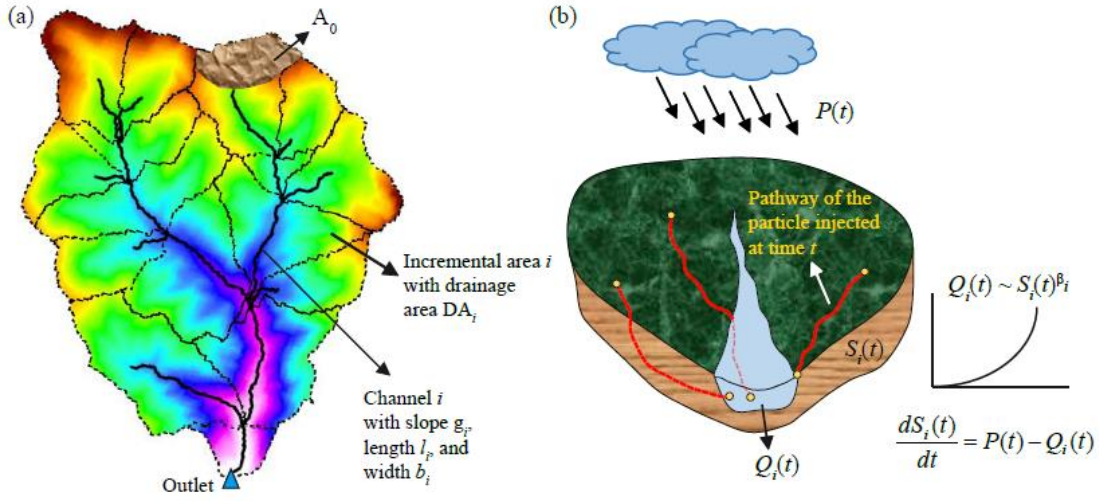

Figure 4.1. Schematic of a catchment decomposition into incremental areas (IAs), each IA represented by a single storage model. (a) A hypothetical catchment *w* composing of channels *i*, $i = 1, ..., N$, each with incremental drainage area DA_i. Each channel is characterized by its length, gradient, and width denoted by l_i, g_i, and b_i, respectively, and A_0 is the channel initiation area. (b) Illustration of a single storage model at which the mass balance holds between the precipitation (P), soil storage (S_i), and discharge (Q_i). Evapotranspiration is ignored for simplicity.

4.3.2. Hydrologic Model

The flow through each IA_i is simulated using a single storage (reservoir) model (Fig. 4.1b). Precipitation (P) is considered spatially uniform across all IA_i's, evapotranspiration is ignored for simplicity, and the discharge (Q_i)-storage (S_i) relationship is assumed to be a power law with parameters K_i and β_i, i.e.,

$$Q_i(t) = K_i S_i(t)^{\beta_i} . \quad (4\text{-}1)$$

Kirchner [2016b] proposed that the coefficient K in equation (4-1) can be parameterized by the exponent β and a storage value called "reference" storage, S_{ref}. Being much more meaningful and easier to interpret than K, the reference storage is a surrogate for the residual storage when β_i is significantly larger than 1 and represents the storage levels at which Q equals the long-term average input rate ($\overline{P}$), i.e., $\overline{P} = KS_{ref}^{\beta}$. As such, the mass balance for IA_i is written as

$$\frac{dS_i(t)}{dt} = P(t) - \overline{P}\left(\frac{S_i(t)}{S_{i,ref}}\right)^{\beta_i} . \quad (4\text{-}2)$$

4.3.3. Time-Variant Travel Time Distribution (TTD) Analysis

The theory of time-variant TTD has been developed based on the Lagrangian representation of a catchment, where the water and solute particles are tracked along their spatially heterogeneous hydrologic pathways. The probability distribution of the particles' stochastic displacement is expressed by the Fokker-Planck equation [e.g., *Risken*, 1984] which is similar in form to the advection-dispersion model. Also, each particle contained within the catchment is labeled by its age or residence time (t_R) which is the difference between the current time and the time at which it entered the catchment. Particles injected at the same time can have very different ages at the same location due to the spatial heterogeneity of the transport properties along their pathways. The age distribution of the particles residing in a given location at a given time can be characterized by the mass age density function [*Ginn*, 1999] and the linkage between the displacement and the mass age distribution functions [*Benettin et al.*, 2013a] constitutes the basis for the Master Equation [*Botter et al.*, 2011], describing how the age distribution of the particles evolves over time. In general, the particle's travel time (t_T), which is the time between its entrance to and exit from the catchment, is different from

its residence time. However, in the case of the random sampling scheme (which gives the same preference to the particles with different ages in storage while they are sampled by discharge), TTD conditioned on a given time t, $p(t_T, t)$, coincides with the residence time distribution conditioned on the same time and is expressed as

$$p(t_T, t) = \frac{P(t - t_T)}{S(t - t_T)} \exp\left(\int_{t-t_T}^{t} - \frac{P(u)}{S(u)} du \right). \quad (4\text{-}3)$$

If the Master Equation is first multiplied by t_R and then integrated between 0 and ∞, a first-order linear differential equation is derived for the time-variant MTT [*Porporato and Calabrese*, 2015] which can be solved analytically. The general solution (under the random sampling assumption) is

$$MTT(t) = \exp\left\{ - \int_0^t \frac{P(u)}{S(u)} du \right\} \cdot \left[MTT_0 + \int_0^t \exp\left\{ \int_0^u \frac{P(z)}{S(z)} dz \right\} du \right]. \quad (4\text{-}4)$$

where MTT_0 is the MTT at the initial time step. Higher order moments of the TTD, however, should be numerically computed from equation (4-3).

4. Results and Discussion

4.1. Biasedness of Mean Travel Time (MTT) to Aggregation of Spatial Heterogeneity

We first focus on the simplest case for illustration purposes: a two component model in which two IA_i's with different β_i's and $S_{i,ref}$'s mix. To introduce significant contrasting heterogeneity among the IA_i's, β_i and $S_{i,ref}$ are sampled from uniform distributions varying between [1−50] and [20−1000] mm, respectively, giving a wide range of system response to the input precipitation. For each IA, the hydrologic model is run over a 6 years period by using the daily precipitation data for the Redwood River Basin (44°33′ N, 95°40′ W), Minnesota, USA; however, one might use data from other locations or run a stochastic model to generate a synthetic precipitation time series. The resulting

hydrologic fluxes (i.e., P, Q_i and S_i) are then used in equation (4-3) (which assumes the random sampling scheme) to compute $p_i(t_T, t)$.

Under the aggregation of two IAs, the "true" TTDs in the mixture are computed by flow-weighted averaging of $p_i(t_T, t)$, $i = 1, 2$, to account for different mixing ratios arising from different instantaneous flows from each of the IA. Now, if we pretend that we do not know the fluxes corresponding to the two IAs, but only know their aggregate flux (which would be the case in the absence of subcatchment data) and use this flux in equation (4-3), the "apparent" TTDs [after *Kirchner*, 2016a] can be obtained. In both cases, since we are interested in the integrated long-term behavior of a catchment, the marginal TTD, $p_{w,m}(t_T)$, is computed as

$$p_{w,m}(t_T) = \int_{\Gamma} p_w(t_T, t)\, f(t) dt. \tag{4-5}$$

where Γ is the simulation period and the weights $f(t)$ are equal to the normalized discharge time series (by the total discharge over Γ) at the whole catchment outlet. Accordingly, the first and second moments of $p_{w,m}(t_T)$ denoted by $\mathrm{MTT}_{w,m}$ and $\mathrm{SDTT}_{w,m}$, respectively, are estimated. Skipping the first year of simulation as a warm-up period, the results for the last 5 years are reported and discussed below.

Figure 4.2a shows the apparent versus true MTT for the case of a system with two spatially heterogeneous IAs. The simulation was performed for 1000 pairs of IAs with MTTs differing by a factor of 1 to 5. The excellent coefficient of determination (R^2 = 0.99) and small root-mean-square error (RMSE = 6.02 days) shows that the apparent MTTs estimated from the time-varying lumped stochastic Lagrangian formulation of transport are unbiased as compared to the true MTTs which explicitly consider the spatial heterogeneity. This is because the influence of the IAs' spatial heterogeneity is translated into the time-variability of the corresponding hydrologic fluxes (via the discharge-storage relationships), which is subsequently projected into the temporal

dynamics of the combined fluxes of the IAs, used to compute the whole catchment's TTD.

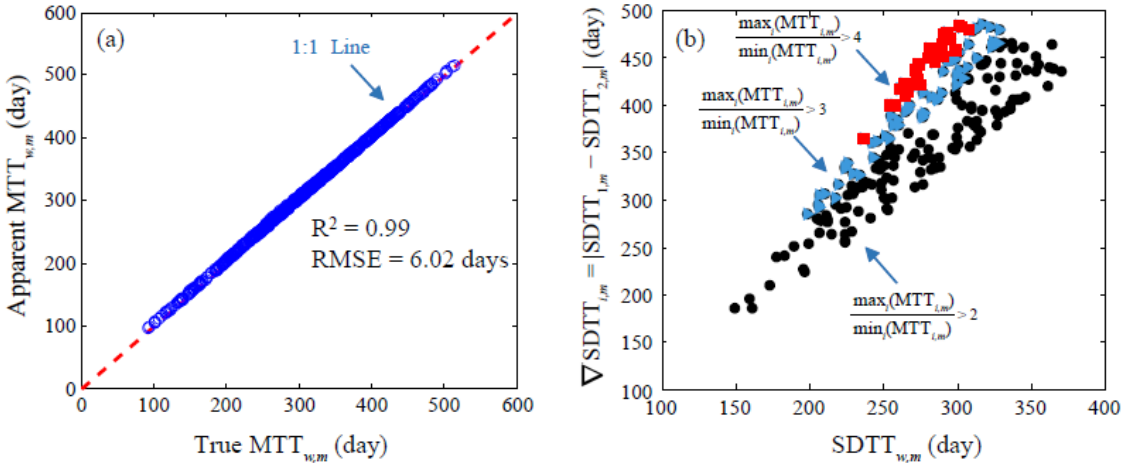

Figure 4.2. Effect of spatial heterogeneity on the scale and shape of the aggregated time-variant travel time distribution (TTD). (a) Comparison of the apparent MTT (computed using the aggregated fluxes of the catchment and a time-varying lumped Langrangian formulation) with the true MTT (computed using the fluxes of the individual IAs) in a two reservoir system under the random sampling assumption. Each point corresponds to a catchment comprising of two IAs with contrasting MTTs. The excellent fit to the 1:1 line shows that the apparent MTTs estimated from the time-varying lumped stochastic Lagrangian formulation are unbiased as compared to the true MTTs which explicitly consider the spatial heterogeneity. (b) Dependence of the form of the catchment TTD on the spatial heterogeneity of IAs. The horizontal axis gives the standard deviation of the marginal TTD in a catchment comprising of two IAs, and the vertical axis gives the difference between the standard deviations of the marginal TTDs of the individual IAs. Within-catchment spatial heterogeneity imposes stronger influence on the form of the catchment TTD when the difference between the IAs' average transport time scales is larger.

We also explored the biasedness of the apparent MTT to the aggregation of spatial heterogeneity if other than random sampling mechanisms were used. This was examined by assuming that the IAs and their mixture follow the same sampling scheme, giving high preference to water particles with younger ages while they are sampled as discharge

from storage, under the same other simulation conditions used in Figure 4.2a (preference to younger ages has been revealed by many experimental and modeling studies, e.g., *Benettin et al.* [2015a]). Figure 4.3 shows that the relationship between the apparent and true MTTs is more scattered, but not strongly biased as evidenced by R^2 = 0.88 and RMSE = 18.02 days.

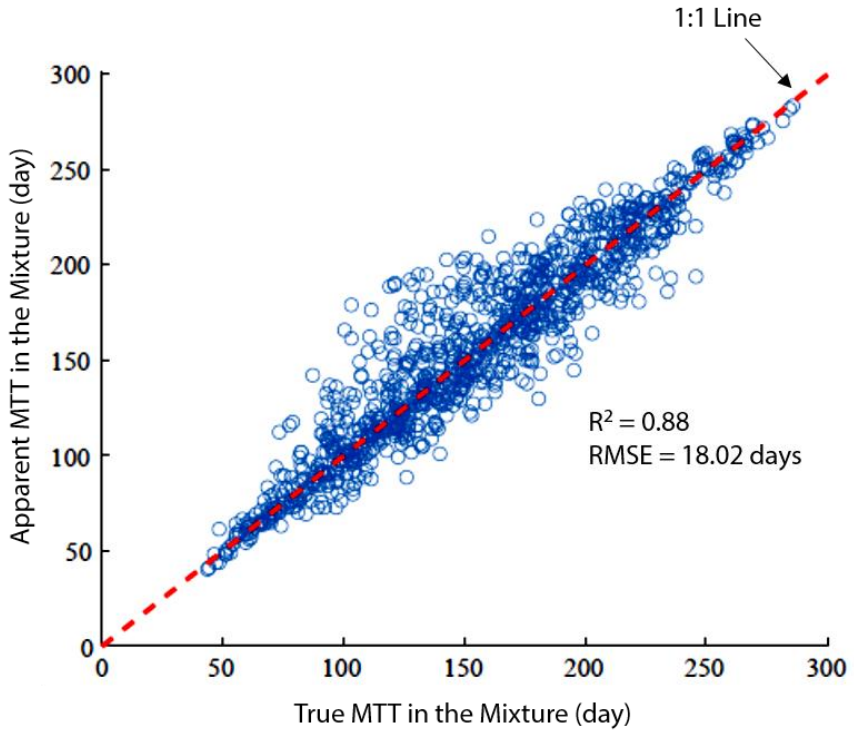

Figure 4.3. Apparent MTT (computed using the aggregated fluxes of the catchment) versus true MTT (computed using the fluxes of the individual Incremental Areas, IAs) in a catchment comprising of two IAs. Individual IAs are assumed to follow a SAS function giving high preference to younger ages (by setting $\alpha = 0.4$ and $\beta = 1$). The same SAS function shape is assumed for the mixture.

Additionally, to understand how the mixture's true SAS function might look like when two IAs are combined, the following quantities were computed:

$$p_{RT}(t_R,t)_{mix} = \frac{S_1(t)\,p_{RT}(t_R,t)_1 + S_2(t)\,p_{RT}(t_R,t)_2}{S_1(t) + S_2(t)}. \tag{4-6}$$

$$p_T(t_T,t)_{mix} = \frac{Q_1(t)\,p_T(t_T,t)_1 + Q_2(t)\,p_T(t_T,t)_2}{Q_1(t) + Q_2(t)}. \tag{4-7}$$

These two equations are indeed storage- and flow-weighted averages of the residence and travel time distributions of the IAs to find the corresponding true residence and travel time distributions in the mixture, respectively. The SAS function of the mixture can then be computed as the ratio between $P_T(t_T,t)_{mix}$ and $p_{RT}(t_R,t)_{mix}$.

$$\omega_Q(t_T,t)_{mix} = \frac{P_T(t_T,t)_{mix}}{p_{RT}(t_T,t)_{mix}} \tag{4-8}$$

Figure 4.4 illustrates that under the random sampling assumption, the mixture's true sampling scheme tends to remain almost uniform, making thus the assumption of uniform sampling for the mixture reasonable. Nevertheless, this does not necessarily hold for other sampling schemes, i.e., the mixture's true sampling scheme might be significantly different from that assumed for the individual IAs. This implies that the scatter in Fig. 4.3 might be due to the assumption that the mixture has the same sampling scheme as the individual IAs. Therefore, if one can determine or closely approximate the underlying sampling mechanism at some aggregation scale (e.g., from concentration time series), the apparent MTTs at that scale are expected to show even less scatter than that shown in Fig. 4.3.

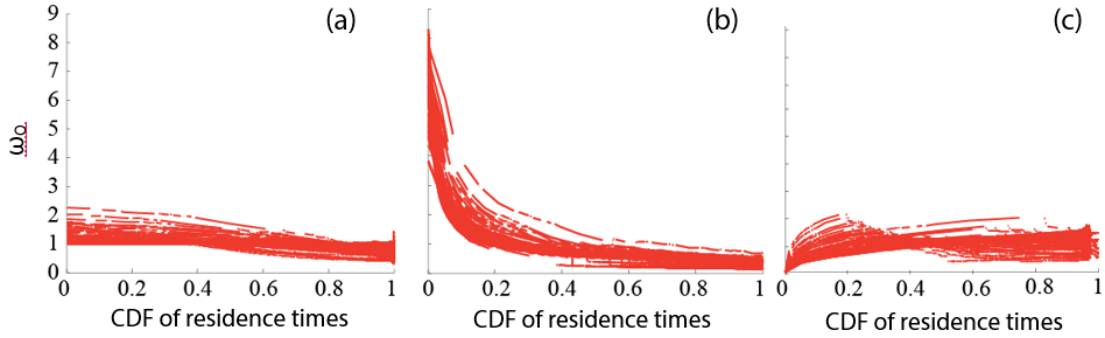

Figure 4.4. Estimated SAS functions ω_Q in a catchment comprising two Incremental Areas (IAs) with three different underlying sampling schemes. (a-c) show the SAS functions inferred from the mixture of IAs with sampling schemes giving no preference to ages, high preference to younger ages, and high preference to older ages, respectively. Each scenario includes 100 simulations having the same SAS function shape, but different discharge- storage relationships.

These observations are noteworthy for the following reasons. First, since climatic and stream hydro-chemistry measurements are often only available at the whole catchment scale, the above findings indicate that the implemented time-variant lumped stochastic transport formulation can make use of such data to provide a reliable estimation of the MTT at some aggregated scale without needing to explicitly define the spatial heterogeneity at smaller scale, but still reflecting its influence. Although it was recently concluded that there is little basis for optimism that the MTT estimated from the existing methods is immune to aggregation error [*Kirchner*, 2016a, 2016b], our study provides a benchmark testing of the stochastic Lagrangian framework, demonstrating that its time-variant nature yields MTTs that are not significantly biased to the aggregation of spatial heterogeneity, particularly under the random sampling hypothesis (e.g., compare Fig. 4.2a with Fig. 7 in *Kirchner* [2016a]). Second, our analysis highlights the advantage of this framework to estimate less biased MTTs as opposed to the extensively used sine-wave fitting method [e.g., *Soulsby et al.*, 2000; *Rodgers et al.*, 2005, among others]. *Kirchner* [2016a] elegantly showed that MTTs estimated by using the seasonal tracer

cycles of precipitation and streamflow at the whole catchment scale via the sine-wave fitting method can be 6 times smaller than the true MTTs.

4.2. Spatial Heterogeneity Projected in the Form of the Travel Time Distribution (TTD)

Under the same numerical experiment outlined in section 4.1, Fig. 4.2b shows the difference between the standard deviations of the TTDs of the two IAs, i.e., $\nabla \mathrm{SDTT}_{i,m} = |\mathrm{SDTT}_{1,m} - \mathrm{SDTT}_{2,m}|$, against the combined w catchment apparent $\mathrm{SDTT}_{w,m}$ for 1000 simulations. Pairs with MTTs differing by at least a factor of 2, 3, and 4 are shown by different colors. The scatter in the relationship between $\nabla \mathrm{SDTT}_{i,m}$ and $\mathrm{SDTT}_{w,m}$ decreases as the difference between the combining IAs' average transport time scales increases, i.e., the more the IAs contrast with respect to their transport time scales, the stronger the dependence of the TTD of the mixture on the spatial heterogeneity of IAs. Here we note that in most real-world cases, the physical characteristics of nearby IAs (e.g., geology, topography, and soil hydraulic properties) typically do not differ significantly, thereby the spatial variability at small spatial scales (resulting from spatial heterogeneity) might not be readily inferred from the time variability of the TTDs at some immediate larger scale. Furthermore, it is acknowledged that if a larger than 2 number of IAs aggregate, the prediction of the relationship between the whole catchment variability and its IAs' spatial heterogeneity is even more challenging and poorly understood [e.g., *Kirchner et al.*, 1993]. The next section explores the dependence of such variability on the aggregation of spatial heterogeneity in large-scale catchments (i.e., $O(10^2)$−$O(10^3)$ km^2).

4.3. Variability of Mean Travel Time (MTT) vs. Spatial Aggregation

The numerical experiment presented above was extended to study the effect on TTD of a wider range of spatial variability and structured heterogeneity in the catchment organization. We first generate a TSS tree with $a = 1.1$, $c = 2$, and $\Omega = 5$. Each channel

is assigned a drainage area DA_i, randomly sampled from an exponential distribution with mean 3 km^2. The hydrologic model is then run to obtain the hydrologic fluxes at the outlet of each IA_i, and the outflows from all IA_i's are routed through the river network by using the channels' topographic and geometric attributes (i.e., l_i, g_i, and b_i) determined as described in section 2.1. The flow routing scheme we used is based on the numerical solution of the coupled mass and momentum conservation equations for each channel [see *Mantilla et al.*, 2006 for more detail]. Travel time analysis (using equation (4-4)) is then performed for all catchments with $1 \leq \Omega \leq 5$, but by using the routed fluxes at their corresponding outlets. We also assume that the transport time scales in the river channels are much smaller than those in the soil storage and are thus neglected.

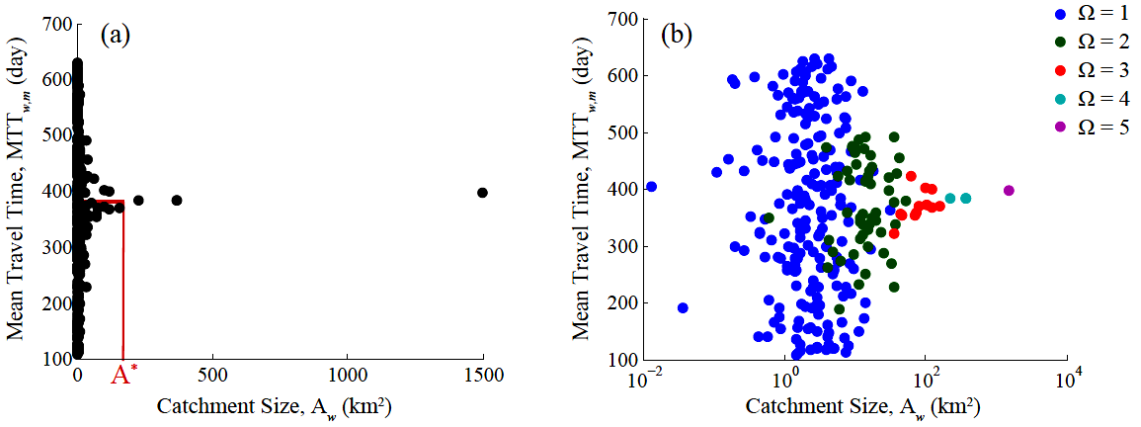

Figure 4.5. Variability of the mean travel time (MTT) with the scale of hierarchical spatial aggregation, and dependence of the catchment characteristic scale (A^*) on the spatial distribution of incremental areas (IAs) and the underlying river network topology. (a) Variability of catchment $MTT_{w,m}$ with the catchment size A_w in a fifth-order catchment composing of nested subcatchments. The catchment was synthetically generated by the Tokunaga model with parameters a = 1.1 and c = 2 and IAs with an exponential distribution with mean λ = 3 km^2. As the hierarchical aggregation of IAs takes place, $MTT_{w,m}$ shows a convergence to a constant value after A^*. (b) shows the same plot as (a), but the horizontal axis is in a logarithmic scale so that the scatter at the small spatial scales is more visible. Catchments with the same Horton-Strahler order (Ω) are also depicted by distinct colors.

Figure 4.5a shows the $MTT_{w,m}$ versus the upstream area A_w, and Fig. 4.5b shows the same plot, but the horizontal axis is in a logarithmic scale so that the scatter at the small spatial scales is more visible. The hierarchical aggregation of the IAs is seen to reduce variability in the MTTs, making them progressively less dependent on the network structured spatial heterogeneity. Moreover, as the aggregation scale increases, there exists a characteristic spatial scale (A^*) above which the variability in the MTT vanishes and the magnitude of MTT is not influenced by the aggregation of spatial heterogeneity. This observation raises the immediate question: what controls the magnitude of A^* as well as the magnitude of the MTT at A^*?

Via Monte-Carlo simulations of a stochastic soil moisture model, *Botter et al.* [2010] and *Botter* [2012] found that MTTs in a hillslope are clearly dependent on the hydro-climatic features of a basin, that is, the MTTs in wet climates are smaller than those observed in dry climatic conditions. This suggests that the magnitude of the MTT at spatial scales larger than A^*, which is equal to the average of the IAs' MTTs, is to some degree controlled by climate. However, it might also depend on the underlying geology [e.g., *Maxwell et al.*, 2016], vegetation [e.g., *Tetzlaff et al.*, 2014], and topography [e.g., *McGuire et al.*, 2005] which is more complex to quantify as these characteristic typically co-evolve with climate [*Troch et al.*, 2013]. For instance, *Heidbüchel et al.* [2013] concluded that in very dry climatic conditions with a rare soil moisture response, the MTT is significantly dependent on the landscape topography (as most of the water flow pertains to groundwater and bedrock aquifers), while in very wet soil moisture conditions, soil depth, and hydraulic conductivity would control the MTT (as a significant portion of the soil profile is involved in transport). Quantifying the distinct influence of geology, topography, and climate on the MTT thus cannot be easily determined and needs further study. Nevertheless, the theory of time-variant TTDs offers the opportunity to quantify the impact of morphologic and climatic attributes on MTTs through the analysis of their impact on the underlying hydrologic fluxes.

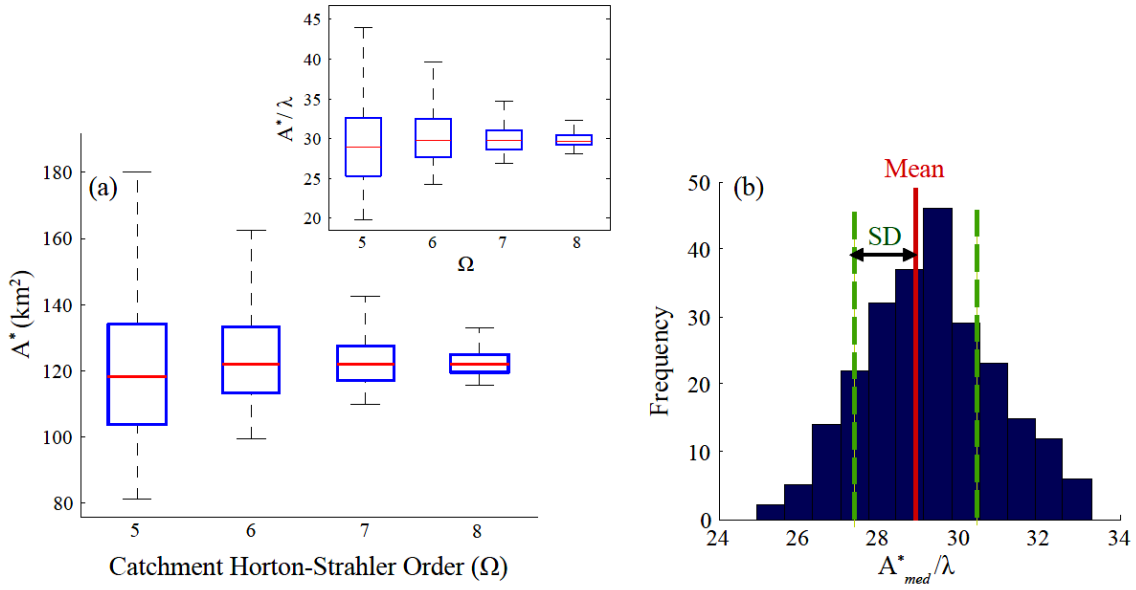

Figure 4.6. Dependence of the catchment characteristic scale (A^*) on the spatial distribution of incremental areas (IAs) and the underlying river network topology. (a) A^* versus Ω for 1000 realizations of Tokunaga trees with a = 1.1, c = 2, λ = 3 km^2, and Ω = 5, 6, 7, 8. For each realization, DA_i and β_i were randomly sampled from exponential distribution with mean λ and uniform distribution spanning the ranges of 1−50, respectively. The inset shows A^*/λ versus Ω. The median of A^*/λ, i.e., A^*_{med}/λ, takes place at almost the same magnitude in catchments with different orders, while its variance decreases as the catchment's order increases. (b) Histogram of the ratio A^*_{med}/λ for the Tokunaga trees with Ω = 5, and parameters a and c ranging in [0.9−1.3] and [2−3.4], respectively (1000 simulations per each pair of a and c). A^*_{med}/λ is seen to vary between 25.0 to 33.3 with mean 29.2 and standard deviation of 1.7, suggesting that A^*_{med}/λ does not depend significantly on the river networks' probabilistic branching structure.

Numerous realizations of heterogeneous catchments were generated composed of exponentially distributed IAs with λ = 3 km^2 attached to branching structures corresponding to the generated TSS trees of parameters a = 1.1 and c = 2. Although TSS trees with the same a and c have the same probabilistic branching structure, each realization gives a river network exhibiting different channel connectivity as well as

spatial arrangement of incremental areas. For each simulation, the variance of the MTTs over increasing spatial scales is computed and A^* is identified as the scale after which the standard deviation is less than 0.01 day. Figure 4.6a shows the box plot of A^* for 4 sets of simulations, each including 1000 realizations of TSS trees with Ω = 5, 6, 7, and 8. Regardless of the catchment's order (or size), the median of A^* (denoted by A^*_{med} from here on) takes place at almost the same magnitude, showing independence to the catchment's underlying river network topology as well as the spatial arrangement of the IAs within a catchment. Also, the variance of A^* is seen to decrease as the catchment's order increases because, in higher order catchments, there exists a larger number of lower-order branchings that aggregate, hence their heterogeneity imposes less influence on the overall variability of MTT.

We notice from Fig. 4.6a that the magnitude of A^*_{med} obtained from these experiments is ~120 km^2. However, this is not a universal value and it relates to the catchment mean incremental area (λ) and the channel initiation area (A_0), which were kept constant in the above numerical experiments. For instance, if two catchments with the same total drainage area are considered, the one with smaller A_0 would be dissected by a larger number of channels (or IAs), resulting in larger drainage density, smaller λ, and hence smaller A^*. Since both A^* and λ vary with A_0 in the same direction, their ratio might not depend on A_0. We examine this by extracting multiple river networks from 10m Digital Elevation Model of the Redwood River Basin by defining different A_0's ranging from 0.05 to 0.5 km^2 [e.g., *Tarboton et al.*, 1991], and the corresponding λ's were computed by delineating the IAs of each channel network (we note that switching from synthetic to real river networks for this experiment was simply because A_0 cannot be introduced while generating TSS trees). By repeating the travel time analysis on the extracted networks, Fig. 4.7 shows that A^*_{med}/λ does not change significantly with A_0, spanning from 25.9 to 33.4 with mean 28.7 and standard deviation of 2.4. Accordingly, Fig. 4.6a

was transformed by plotting A^*/λ versus Ω (see the inset), indicating that A^*_{med}/λ varies slightly between 28.87 and 29.54 with mean 29.2 and standard deviation of 0.45.

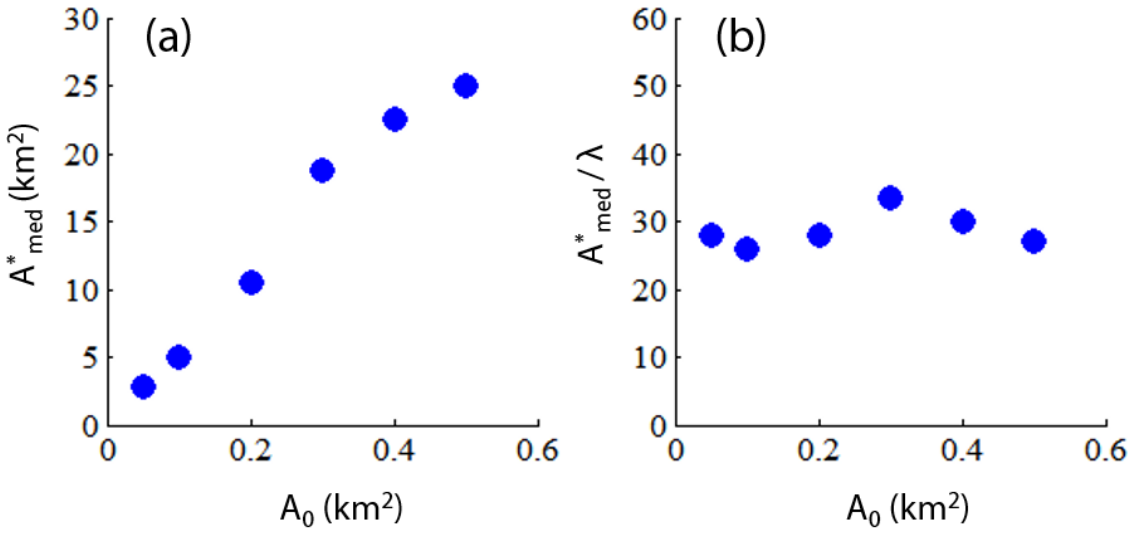

Figure 4.7. Dependence of the catchment median characteristic scale, A^*_{med}, on the channel initiation area, A_0. (a) shows A^*_{med} computed for multiple river networks, all extracted from 10m Digital Elevation Model of the Redwood River Basin but by varying the channel initiation area A_0 between 0.05 to 0.5 km^2. (b) shows A^*_{med}/λ versus A_0 for the same river networks in (a). For each network, λ was computed by delineating its incremental areas (IAs) and then computing their mean.

Figure 4.8 also shows the relationship between A^*_{med}, A_0, and drainage density, as well as the illustration on the independence of A^*_{med}/λ to the catchment drainage density. It is seen that significant correlation holds between A^*_{med} and drainage density, implying that as the drainage density increase, A^*_{med} decreases (via a power law) due to the fact that in a catchment with larger drainage density, there exists a larger number of IAs required to reach the characteristic scale, hence A^*_{med} takes place in smaller spatial scale. A_0 also

shows almost the same relationship to the drainage density simply because there relationship between A^*_{med} and A_0 is linear. However, no clear relationship is found between the ratio of A^*_{med}/λ and drainage density.

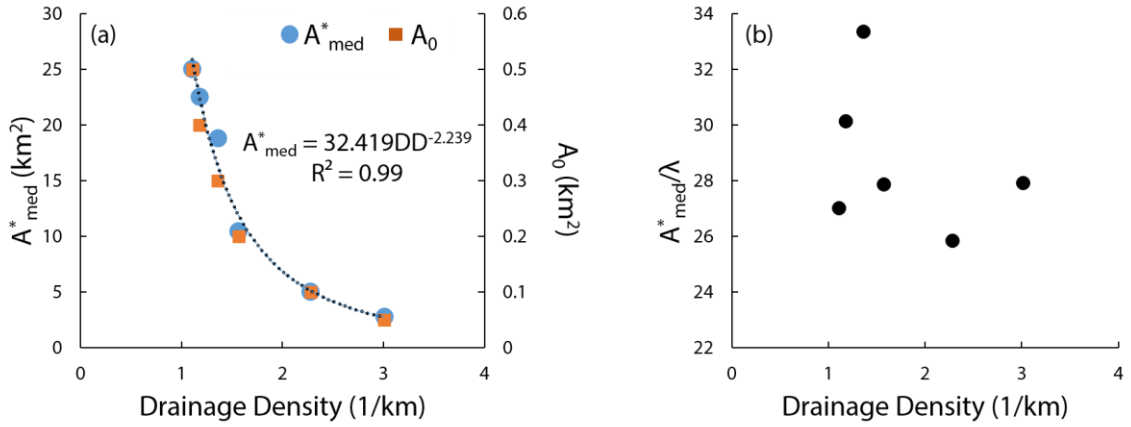

Figure 4.8. Relationship between the catchment median characteristic scale (A^*_{med}) and drainage density. (a) A^*_{med} shows a power law relationship with the drainage density for the same river networks in Fig. 4.7 with the channel initiation area A_0 between 0.05 to 0.5 km$^{2.}$. (b) The ratio of A^*_{med}/λ versus drainage density indicating no correlation between them.

4.4. Dependence of Catchment Characteristic Scale on Tokunaga Parameters

Since the estimation of the TSS parameters for a catchment is robust to the A_0 used to define the first-order channels [*Zanardo et al.*, 2013], we further examine the dependence of A^*_{med}/λ to the Tokunaga parameters *a* and *c*. Figure 4.6b shows the histogram of A^*_{med}/λ for the TSS trees with Ω = 5, and parameters *a* and *c* ranging in [0.9−1.3] and [2−3.4], respectively (1000 simulations per each pair of *a* and *c*). The chosen Tokunaga parameters are within the range reported by *Zanardo et al.* [2013, Fig. 9] for the majority of the river basins across the Unites States. For all values of the

Tokunaga *a* parameter, significant negative correlation was found between A^*_{med}/λ and the *c* parameter (Pearson's linear correlation coefficient >−0.8 and P-value < 0.003 at 5% significant level). This is because in a river network with a larger value of *c*, there exists a larger number of low-order channels merging to higher-order branches, hence the characteristic scale emerges at smaller spatial scales as a larger number of low-order channels is available for aggregation to reach the characteristic scale faster. Nevertheless, for all combinations of *a* and *c*, A^*_{med}/λ is seen to change between 25.0 to 33.3 with mean 29.2 and standard deviation of 1.7, suggesting that A^*_{med}/λ does not depend significantly on the river networks' probabilistic branching structures. Indeed, from the simulation results it turns out that there exists a level of hierarchy in catchments at which the spatial heterogeneity loses its dominance on the MTT (which is the direct consequence of the Central Limit Theorem) and the magnitude of such a characteristic spatial scale in high-order catchments is on average approximately equal to 30 times the mean incremental area. The above findings have practical implications pertaining to data measurements in the field and inferences that can be made on transport time scales and mixing processes across spatial scales. Specifically, if the interest is to understand the functioning of a large catchment, collecting data at scales smaller than A^* does not allow extrapolation of the computed MTT to larger scales, whereas the MTT computed from scales comparable to A^* and a time-variant Lagrangian transport formulation is not prone to the influence of the aggregation of spatial heterogeneity, allowing thus reliable interpretation and inference at the large catchment scale.

5. Conclusions

Needing to move from overparameterized spatially distributed models to reduced-complexity frameworks while still embedding the spatial heterogeneity of real catchments [*McDonnell et al.*, 2007; *Troch et al.*, 2009] together with yet limited knowledge of how to extrapolate information from the field to the larger scales [e.g.,

Hrachowitz et al., 2013], we examined the ability of the lumped stochastic Lagrangian formulation for water and solute transport in providing reliable estimates of the mean travel time (MTT) in spatially heterogeneous catchments. Via numerical simulations of heterogeneous catchments, we showed that:

1) a time-varying travel time distribution (TTD) formulation results in MTTs that are unbiased to the aggregation of spatial heterogeneity under the random sampling assumption, and not significantly biased under other sampling schemes. This finding reinforces the importance of such a time-variant lumped formalism to appropriately predict the catchment's mean transport time scales without the need to explicitly characterize and embed small-scale spatial heterogeneity.

2) although significant variability of MTT exists at small spatial scales, there exists a characteristic spatial scale above which the MTT converges to a constant value not influenced by the aggregation of spatial heterogeneity.

3) the ratio between the catchment characteristic scale and the mean incremental area is on average independent of the river network topology and spatial arrangement of incremental areas.

This work is one small step toward understanding the dependence of MTT on the network-structured spatial heterogeneity and further study is required to explore the impact of other catchment's physical characteristics (such as hillslope gradient, aspect, soil depth to groundwater, subsurface flow path length, and proportion of hydrologically responsive soil) on the MTT at hierarchical spatial scales.

We have discussed so far the physical processes and transport time scales corresponding to the catchment subsurface layer. However, some natural processes such as hyporheic exchanges and interactions with riparian zones take place in streams. The transport features engaging with these processes, thus, cannot be understood without considering their influence across many (mostly heterogeneous) parts of the drainage system,

including the terrestrial landscape and channels of the river network [e.g., *Lindgren et al.*, 2004; *Mulholland et al.*, 2008; *Ranalli and Macalady*, 2010]. The river networks synthetically generated by the Tokunaga model throughout this chapter were statistically self-similar, enabling us to characterize them by using some scaling relationships, e.g., the Hack's law, which further facilitates exploring the relationships between the river network structure and in-stream natural processes. However, some river networks do not follow self-similar relationships across a range of hierarchical spatial scales. For instance in the MRB, geologic controls dating back to the post-glaciation period [*Ojakangas*, 1982; *Nicollet*, 1993] have imposed constraints on the landscape dissection, resulting in a pronounced spatially anisotropic channel network structure which defeats most scaling laws of fluvial landscapes. In the next chapter, such outlier catchments, which we call self-dissimilar, are studied and methodologies are proposed that can probe into their structure in ways that are able to reveal spatially heterogeneous organization and preferential scales of dissection, which in turn can influence the transport and storage time scales at large-scale catchments with implications for solute transport and water quality.

5

Self-Dissimilar Landscapes: Revealing the Signature of Geologic Constraints on Landscape Dissection via Topologic and Multi-Scale Analysis*

*Under Revision in *Geomorphology* as Danesh-Yazdi M., A. Tejedor, and E. Foufoula-Georgiou, Self-Dissimilar Landscapes: Revealing the Signature of Geologic Constraints on Landscape Dissection via Topologic and Multi-Scale Analysis.

5.1. Summary

External climatic or geologic controls, such as tectonics or glacial drainage, might impose constraints on landscape self-organization resulting in spatial patterns of rivers and valleys which do not obey the typical self-similar relationships found in most landscapes. The goal of this study is to quantify how such geologic constraints express themselves on channel network topology, spatial heterogeneity of drainage patterns, and emergence of preferred scales of landscape dissection. We use as an example a basin located in the Upper Midwestern United States where successive glaciations over the past thousand years have led to a pronounced spatially anisotropic channel network structure which defeats most scaling laws of fluvial landscapes. This is contrasted with another river basin in the North-Central U.S. which has been organized under the absence of major external geologic influences and follows a typical self-similar channel

network organization. We show how the geologic constraints have imposed a competition for space which is captured in the slope-local drainage density probabilistic structure, in the failure of self-similarity in basin-wide river network topology, and in the length-area scaling relationship being not typical of fluvial landscapes. Via a two-dimensional wavelet analysis and synthesis, we demonstrate the occurrence of a spectral gap in the power spectrum which corresponds to the presence of preferred scales of organization, and characterize them through multi-scale detrending. The developed methodologies can be useful in advancing our geomorphologic understanding of how external controls might manifest themselves in creating a landscape dissection that is outside the norm and how this dissection can be studied objectively for understanding cause and effect.

5.2. Introduction

Landscape self-organization driven by the movement of water and sediment, and the emergence of river networks that exhibit a hierarchical structure across a range of scales has been the subject of intensive research over the past decades [e.g., see *Rodriguez-Iturbe and Rinaldo*, 2001 and references therein]. Recently, *Zanardo et al.* [2013] studied 408 river networks from 50 basins with different geographic location and climate across the United States to assess if the majority of the river networks exhibit self-similarity (S-S) in their topological structure. Through a rigorous statistical testing of the Hortonian and Tokunaga self-similarities [see *Zanardo et al.*, 2013 for a detailed representation of these tests], they concluded that 96 percent of the river networks overwhelmingly exhibited Hortonian Self-Similarity (HSS), while 80 percent of them followed a topological hierarchical structure that can be well characterized by Tokunaga Self-Similarity (TSS). Furthermore, the influence of some climatic attributes (e.g., mean annual rainfall depth, mean storm duration, and mean storm frequency) on the S-S parameters of the landscape dissection was investigated. Despite the wealth of studies of landscapes drained by river networks that exhibit S-S, detailed studies of those that

break this symmetry are lacking. The goal of this work is to explore such "outlier basins" which we call "self-dissimilar" and propose methodologies that can probe into their structure in ways that are able to reveal spatially heterogeneous organization and preferential scales of dissection, which then can be related to the underlying controls of climate or geology.

Figure 5.1a illustrates an example of such basins corresponding to the 43,400 km^2 Minnesota River Basin (MRB) located in the Upper Midwestern Unites States. The geologic history of the MRB [*Ojakangas*, 1982; *Nicollet*, 1993] reveals that successive glaciations around 100,000 ~ 10,000 BP and the draining of glacial Lake Agassiz in 13,400 BP drastically carved this landscape [*Clayton and Moran*, 1982; *Belmont et al.*, 2011]. While glacial lobes drained over most of this basin leaving behind a flat and lake-punctuated landscape in the central-eastern part, the bedrock western part was not eroded (Fig. 5.1b). Instead, repeated glacial cycles covered that bedrock with glacial till deposits and formed the 320 km long, 160 km wide geological feature called Coteau des Prairies (CDP) residing along the South Dakota border and extending to the northwestern part of the MRB. As is seen in Figs. 5.1c and 5.1d, at the edge of the CDP there is a pronounced difference in the fluvial dissection compared to the rest of the basin, expressed by the presence of a dense number of steep channels and quasi-periodic ridges and valleys. This high slope region (HSR) includes channels with slope larger than 0.01 m/m and maximum elevation less than 500 m. A cross-section of these almost parallel channels in Fig. 5.1d reveals that these are not rills, but well-formed channels ranging in depth from 10 to 20 meters. The longitudinal profile (Fig. 5.1e) of the analyzed area shown by the box in Fig. 5.1b and expanded in Fig. 5.1c shows a 200 m drop in elevation within a 12 km horizontal distance, resulting in the gradient of 0.017 m/m [see also *Gran et al.*, 2009].

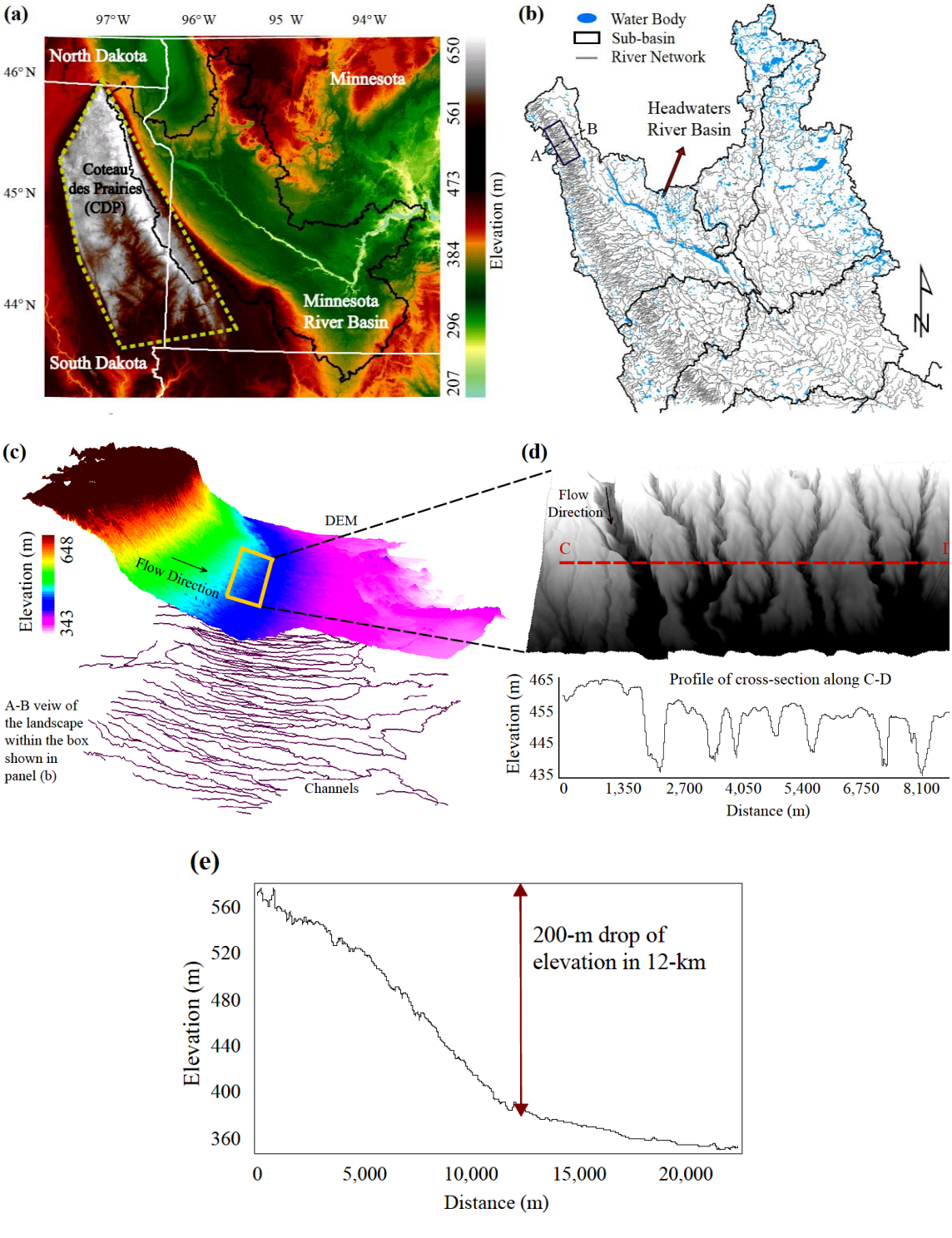
(a)
97°W
96°W
95 W
94°W
46°N
45°N
44°N
North Dakota
Minnesota
Coteau des Prairies (CDP)
Minnesota River Basin
South Dakota
650
561
473
384
296
207
Elevation (m)
(b)
Water Body
Sub-basin
River Network
Headwaters River Basin
A
B
N
(c)
Elevation (m)
648
343
DEM
Flow Direction
A-B veiw of the landscape within the box shown in panel (b)
Channels
(d)
Flow Direction
C
D
Profile of cross-section along C-D
Elevation (m)
465
455
445
435
0
1,350
2,700
4,050
5,400
6,750
8,100
Distance (m)
(e)
560
520
480
440
400
360
Elevation (m)
200-m drop of elevation in 12-km
0
5,000
10,000
15,000
20,000
Distance (m)

Figure 5.1. Illustration of the Minnesota River Basin (MRB) and the Coteau des Prairies (CDP) region. (a) Elevation map of the MRB and the CDP residing along the South Dakota border and extending to the Northwestern part of the MRB. (b) River network topology of the Northern part of the MRB, including the Headwaters sub-basin which encompasses a portion of the CDP. (c) 3D view of the Headwaters landscape delineated by the box shown in panel (b), showing the presence of a dense number of fairly parallel channels. (d) Hillshade of the DEM corresponding to a 70 km^2 patch in the high slope region, depicting quasi-periodic ridges and valleys in this part of the landscape. (e) Longitudinal profile of the cross section A-B within the box shown in panel (b), indicating 200 m drop in elevation within a 12 km horizontal distance.

Figure 5.2 shows the Digital Elevation Model (DEM) and the drainage pattern of the Headwaters River Basin, one of the twelve major sub-basins of the MRB, encompassing a portion of the CDP with a peculiar river network topology, and the Upper Bluestone River Basin located in West Virginia, U.S., as another example of a geologically-controlled landscape. The Upper Bluestone River Basin is indeed a tributary of the much bigger New River Basin which experienced ten geologic era-periods dividing the basin into three major Appalachian Plateaus, Ridge and Valley, and the Blue Ridge Provinces [*Paybins,* 2000]. The Ordovician Taconic Orogeny was the first well-known tectonic event which formed a chain of mountains to the north and east of West Virginia and the next Devonian Acadian Orogeny tectonic event further formed a new set of mountains to the northeast. These strong folding and thrust faulting resulted in the development of long folded ridges which are underlain by sedimentary rocks and separated by relatively flat, broad valleys [*Cardwell,* 1975].

The above basins are only a few examples of a broader category of geologically-controlled landscapes at which deviation from the universal scaling relationships is recognizable from the landscape dissection structure as well as the underlying earth surface processes. For instance, multiple contrasting relationships were found between specific sediment yield and drainage area across a wide range of spatial scales in various regions of Canada, as compared to the typically observed decreasing scaling pattern, e.g., in the south-eastern United States [e.g., see *de Vente et al.*, 2007 and references

therein]. These opposing trends have been associated with the activity of rivers that are still responding to large volumes of sediments remobilized during periods of glaciation [e.g., *Church and Slaymaker*, 1989]. In the study of slope-control on the aspect ratio of weakly dissected river basins ($10-10^3$ km^2), *Castelltort et al.* [2009] attributed anomalous results obtained from some basins in the Columbia River Basin (46° 0′ 0″ N, 116° 0′ 0″ W) to the influence of past tectonics when the North-American plate moved south-west over the Yellowstone Plume. *McGuire et al.* [2005] also emphasized that the lack of relationship between catchment drainage area and mean residence time (as a fundamental descriptor of catchment transport, subsurface storage, mixing, and flow pathways) can be due to the geologic influences having been imposed spatially different throughout the catchment.

Although subjected to a different type of control, all the aforementioned basins are common in carrying the imprint of external forcing, offering a playground for advancing our geomorphologic understanding of cause and effect, studying quantitatively how topographic constrains express themselves on the river network topology, and developing objective methodologies that can extract the prevailing scales of dissection. Addressing these issues constitutes the chief objective of this study. We additionally highlight the morphological differences between self-dissimilar and self-similar landscapes by contrasting the Headwaters river basin with another river basin located in North-Central Washington, the Methow River Basin (Figs. 5.2b and 5.2e). The 4,900 km^2 Methow basin, which is similar in size to the Headwaters basin, was selected for the purposes of comparison since it follows the typical self-similar channel network organization [*Zanardo et al.*, 2013] and the bed elevations have reached geomorphic stable condition [*USBR*, 2008]. Even visual comparison of the river network topology of these basins reveals the significant influence of geologic control on the channel dissection of the Headwaters and Bluestone basins, making them drastically different from the drainage pattern of typical self-similar basins such as the Methow basin.

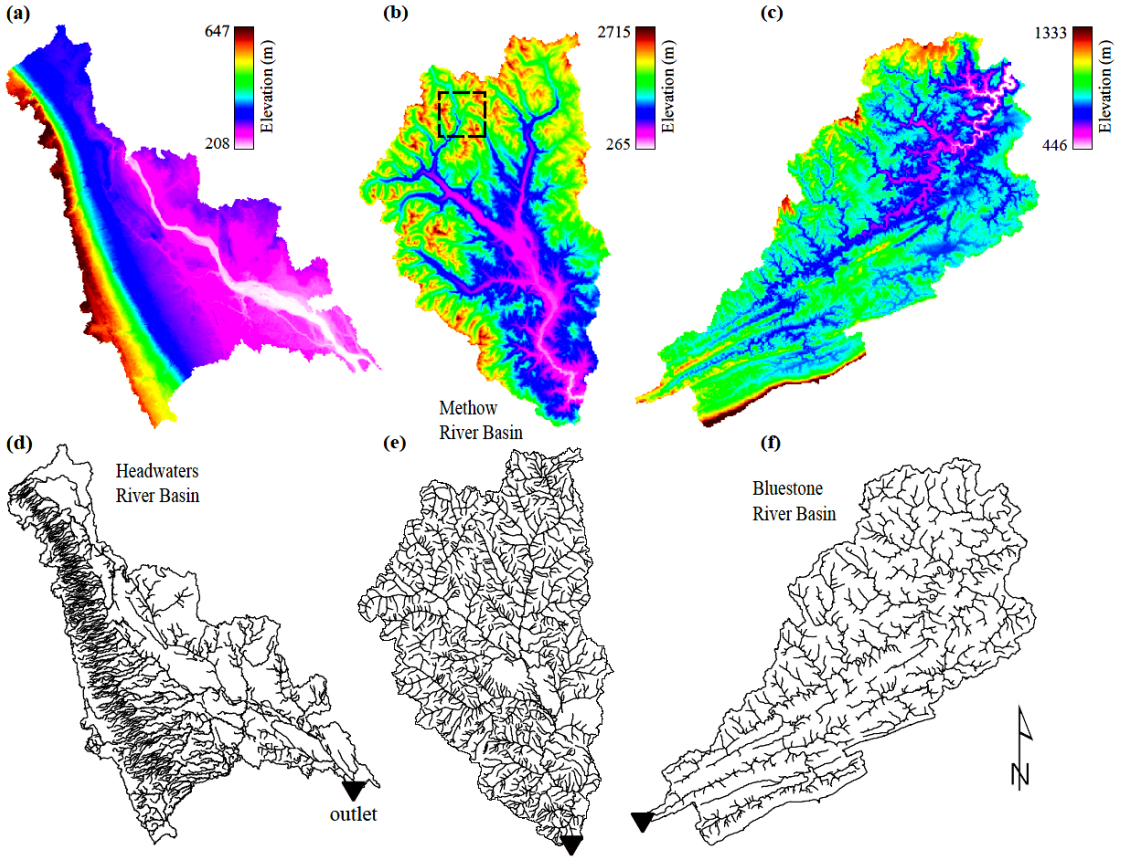

Figure 5.2. Digital Elevation Model (DEM) and river network topology of the self-similar Methow and self-dissimilar Headwaters and Upper Bluestone basins. (a-c) show the elevation map of the 5400 km^2 Headwaters basin (located in Southwestern Minnesota), 4900 km^2 Methow basin (located in Northern Washington), and 1200 km^2 Upper Bluestone basin (a tributary of the much larger New River Basin located in West Virginia), respectively. (d-f) depict the NHDPlus2 river network topology of the Headwaters, Methow, and Upper Bluestone river basins, respectively.

In order to be able to address questions of spatial heterogeneity at all scales and quantify the particular scales and locations contributing mostly to the landscape variability, a localized multi-scale analysis framework, such as that provided by wavelets, is needed. Wavelet analysis has attractive properties such as spatial and spectral localization which allow characterization of differences in the shape and orientation of topographic features

in either one or two dimensions. Here, we examine the wavelet spectrum to study the distribution of landscape variance across scales. We also apply two-dimensional Discrete Wavelet Transform and multi-resolution representation to characterize regular features with preferred scales of organization via a multi-scale landscape detrending.

5.3. Landscape Dissection Analysis

5.3.1. Tests of Hortonian and Tokunaga Self-Similarity

If a river network is represented by a tree composed of links (stream channels) and nodes (stream junctions), in the Horton-Strahler ordering scheme: (1) external links or sources have order equal to 1; (2) when links of the same order w join, the order of the immediate downstream link would be w+1; and (3) when links of different orders come together, they form a link having the highest order of the upstream joining links [*Horton*, 1945; *Strahler*, 1957]. The order (Ω) of a finite river network is equal to the maximum order of links present in the network. For a Hortonian self-similar river network, $N_w / N_{w+1} = R_B$, where R_B is the so-called bifurcation ratio, and N_w is the number of branches of order w, where branches are defined as connected links of the same order. Other commonly studied Horton laws also apply in terms of the average length and average upstream contributing area of the braches of order w, but are not considered here.

The Tokunaga indexing is established on the side branches of a river network, i.e., if N_{ij} is the number of branches of order i that join a branch of order j, and N_j is the total number of branches of order j, the Tokunaga index T_{ij} is defined as $T_{ij} = N_{ij} / N_j$. Thus T_{ij} can be interpreted as the average number of branches of orders i that join a branch of order j. If $\tau_{ij}^{(l)}$ ($1 \le l \le N_j$, $1 \le i < j \le \Omega$) denotes the number of branches of order i that join the nonterminal nodes of the l-th branch of order $j > i$, a tree is called self-similar if its side-branching structure is the same for all branches of the same order (i.e.,

$\tau_{ij}^{(l)} = T_{ij},\ 1 \le l \le N_j,\ 1 \le i < j \le \Omega$) and is also independent of the branch order (i.e., $T_{i(i+k)} = T_k,\ 2 \le i + k \le \Omega$). The Tokunaga self-similarity (TSS) applies an extra constraint [*Tokunaga*, 1978] based on which the ratio of two consecutive Tokunaga indices is constant, i.e., $T_{k+1} / T_k = c,\ 1 \le k \le \Omega - 1$. This gives rise to a family of trees represented by $T_k = ac^{k-1}$, where the positive parameters *a* and *c* are indicative of the first-order side-branching (T_1) and the degree of higher order branching, respectively.

River networks for the Headwaters and Methow basins were obtained from the National Hydrography Dataset (NHDPlus 2.10 released in 2012) and are shown in Figs. 5.3a and 5.3b, respectively. Figures 5.3c and 5.3d show the Horton law of the number of branches, giving the bifurcation ratio equal to 2.87 and 3.93 for the Headwaters and Methow basins, respectively. The linear relationships with coefficients of determination (R^2) equal to 0.92 and 0.98 are both statistically significant, implying that both river networks follow the HSS. However, two points are worth noting. First, although even visually the Headwaters basin exhibits distinct scales of topologic variability not homogeneously present in the landscape, the Hortonian analysis (which essentially applies a coarsening of the landscape based on basin order) is blind to such a structure and indicates the presence of S-S. The inability of the Hortonian analysis to critically depict deviations from S-S has also been reported in other studies [e.g., *Kirkby*, 1976; *Gupta and Waymire*, 1989; *Kirchner*, 1993; *Tarboton*, 1996]. Second, we note that the estimated bifurcation ratio of 2.87 for the Headwaters basin is very low compared to that expected for typical river networks (which is in the order of 4), raising suspicion in its interpretation. The reason for this deviation might be tracked back by comparing the real number of branches of different orders in this basin to the ones "expected" from the bifurcation ratio of 2.87. Indeed, since the maximum order of the Headwaters basin is 7, it is expected that the network includes approximately 3 branches of order 6, 8 branches of order 5, …, 195 branches of order 2, and 559 branches of order 1 if we assume it maintains the bifurcation ratio throughout the lower-order branches. However, topologic

analysis of this river network reveals that there exists a lower number of streams with orders 2 to 5, but a much larger number of first-order streams (that is 648) than expected. Figure 3a shows that the vast majority of such first-order streams not only is present in the high slope region (HSR) of the CDP, but also these streams drain almost parallel to each other decreasing the chance to join and create higher order streams, which ultimately results in a smaller bifurcation ratio than expected for typical landscapes.

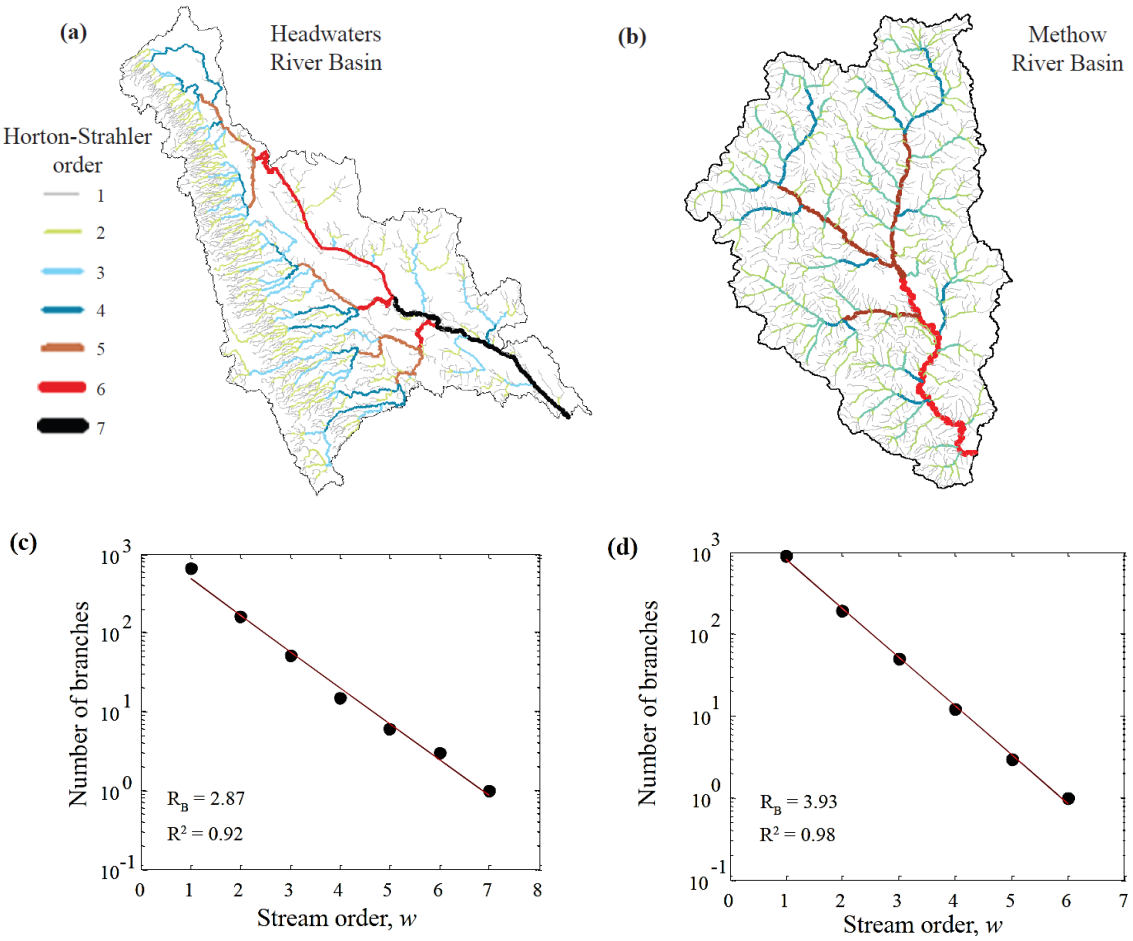

Figure 5.3. Topology and tests of self-similarity (S-S) for the river networks of the Headwaters and Methow basins.

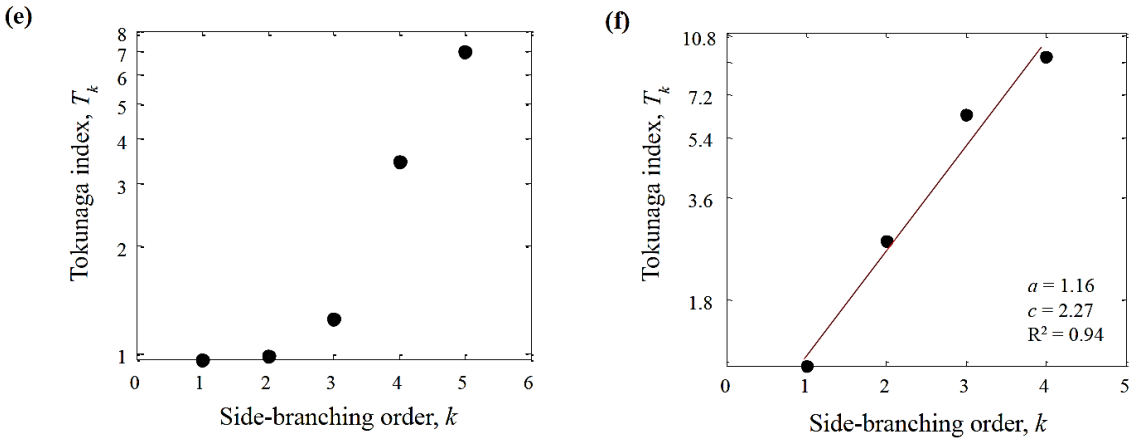

Figure 5.3 (continued). (a) and (b) show the channel network colored by the Horton-Strahler order in the Headwaters and Methow basin, respectively. The presence of a large number of long and fairly parallel low order channels is noticeable in the western part of the Headwaters basin. (c) and (d) depict the Hortonian scaling for the number of branches, confirming the HSS for both river networks. (e) and (f) show the Tokunaga index versus side-branching order, revealing that the stricter TSS is violated in the Headwaters basin, but not in the Methow basin.

Figures 5.3e and 5.3f show the Tokunaga index against the side-branching order for the Headwaters and Methow basins, respectively. It is clearly seen how the stricter TSS is violated in the Headwaters basin, but not in the Methow basin. This is because the TSS considers not only the first-order organization (i.e., number of branches of order w draining into branches of order w+1, that is, $N_{w,w+1}$), but also the transition probability of a branch of order w to drain into a branch of order $w+k$, implying higher order branching. It was found that the total number of low order side-branchings (i.e., N_{12}, N_{23}, N_{34}, N_{13}, N_{24}, N_{14}), which are essentially all the existing transitions in the HSR, forms nearly 60 percent of the same transitions present within the whole basin. This indicates how the hierarchical progression from one order to another is overwhelmingly violated at the above transitions, probing further examination of the causes of the abundance of lower order side-branching within the HSR. Indeed, steep facies (or knickzones) created by the geologic forcing in this region have maintained large areas of low convergence inhibiting the merging of streams to higher orders and resulting in a large number of low

order channels within the HSR. This observation is further investigated in the next section by studying the local drainage density and other geomorphic attributes of the landscape.

5.3.2. Slope-Local Drainage Density Analysis

Drainage density, which is a measure of how dense a landscape is dissected by fluvial channels, has been the focus of several studies aiming to understand how dissection is controlled by factors related to climate and relief [e.g., see *Tucker and Bras*, 1998 and references therein]. Since drainage density in its global form (defined as the total length of fluvial channels divided by total drainage area) cannot account for spatial heterogeneities in a landscape, we compute here the *local drainage density* (LDD), defined as the ratio of the length of a channel to the incremental contributing area draining directly into that channel. Based on this definition, Fig. 5.4 (panels a-d) illustrates the color mapping of the LDD as well as the channel slope on the river network of the Headwaters and Methow basins.

Table 1. Statistics of the channel slope and LDD in the Headwaters and Methow River Basins

Attribute	Statistic	Headwaters basin	Methow basin
Channel slope	Mean (m/m)	0.009	0.129
	Standard deviation (m/m)	0.011	0.102
	Skewness coefficient	1.82	1.17
	Maximum (m/m)	0.089	0.620
LDD	Mean (km/km^2)	1.49	1.02
	Standard deviation (km/km^2)	0.89	0.46
	Skewness coefficient	0.88	0.73
	Maximum (km/km^2)	4.98	2.49

First, it is observed that although the local slopes in the Headwaters basin are on average smaller than those in the Methow basin (i.e., average slope of 0.009 m/m vs. 0.129 m/m, respectively), a reversal is found for the LDDs (i.e., average LDD of 1.49 km/km^2 vs. 1.02 km/km^2, respectively). The maximum LDD in the Headwaters basin (that is, 5.98 km/km^2) is also twice as large as the maximum LDD in the Methow basin (that is, 2.49 km/km^2), implying that the LDD does not necessarily increase with the local slope (see Table 1 for other statistics on the channel slope and LDD). This is counterintuitive as one expects steeper slopes to create longer and narrower incremental areas due to less flow convergence; however, the deviation found here can be an indicator of large-scale heterogeneities in the landscape imposed by tectonic or geologic controls [e.g., *Castelltort and Simpson*, 2006; *Castelltort et al.*, 2009].

Second, higher LDDs in the Headwaters basin are concentrated in the HSR which is very steep and dissected by low order channels (up to order 3), while the Methow basin shows a spatially uniform distribution of slopes and LDDs. A functional comparison of slope and LDD, as shown in Fig. 5.4e, further confirms that in the Headwaters river basin high values of LDDs and slopes fall in the same topographic region related to the HSR, while this is clearly not true in the Methow basin where channels with high LDD do not necessarily correspond to high slopes but span a relatively wide range of slopes. These observations underscore not only the subtle differences between the Headwaters and Methow basins with respect to their landscape organization, but also highlight how the Headwaters basin's HSR has experienced a completely different dissection mechanism compared to the rest of the basin. Figure 5.4f quantifies this by showing the scaling relationship between the channel length and incremental drainage area for all the channels within and outside of the HSR. The high scaling exponent of 0.70 for the HSR affirms the presence of longer streams and narrower contributing areas in this region, demonstrating the particular type of dissection formed in this part of the landscape.

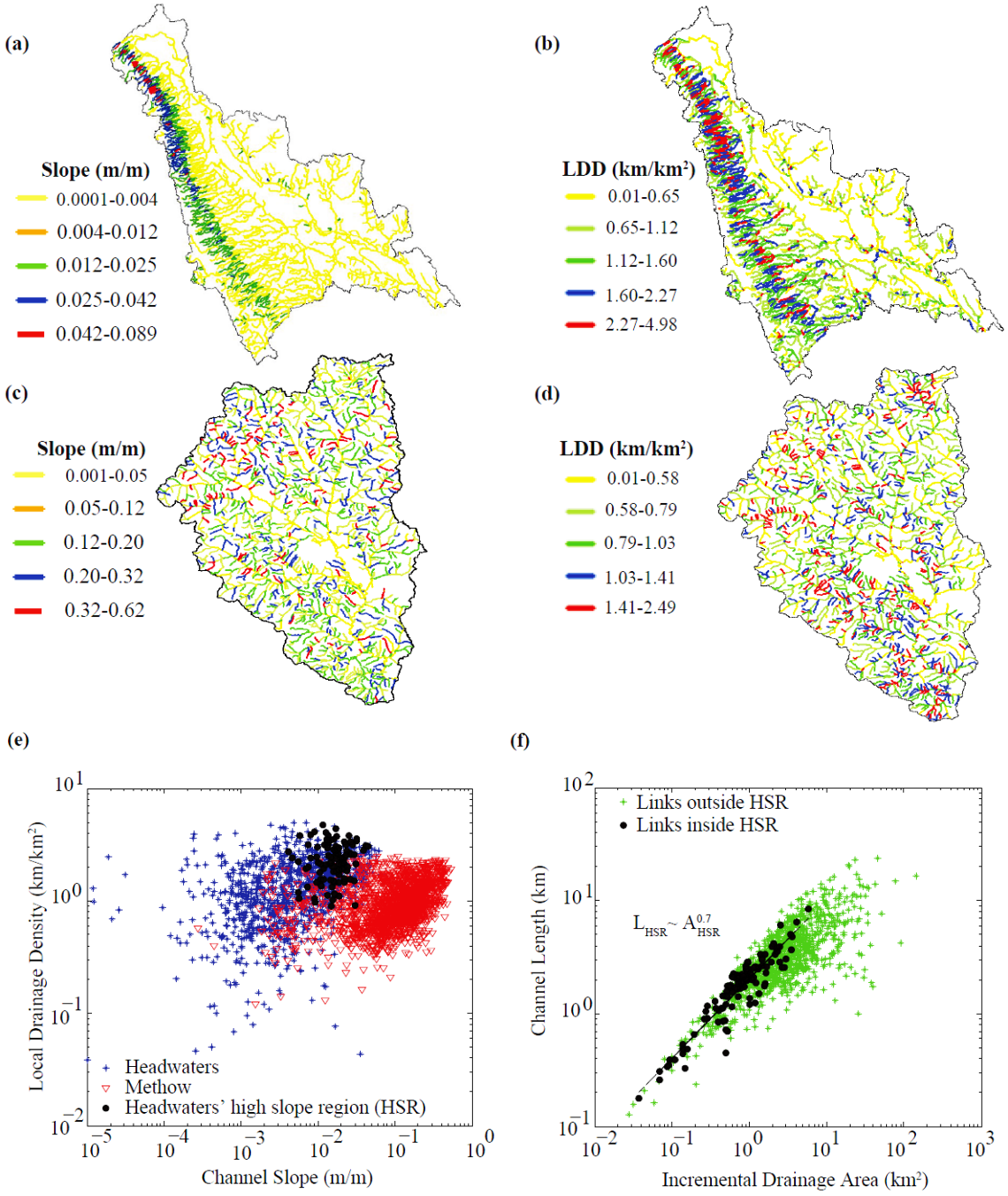

Figure 5.4. Channel slope and LDD spatial distribution, and their functional relationship. (a-b) Spatial distribution of channel slope and LDD in the Headwaters

Figure 5.4 (continued) basin, showing concentration of high LDD in the high slope region (HSR) with steep channels. (c-d) Depicts a uniform spatial distribution of channel slope and LDD in the Methow basin. (e) Functional comparison of the channel slope and LDD between the Headwaters (blue stars), the Methow (red triangles), and the HSR (black circles). (f) Scaling relationship between channel length and incremental drainage area in the Headwaters basin.

To probe further into the relationship between LDD and local slope and specifically to investigate how this relationship might change in a magnitude-frequency space under the presence of spatial heterogeneity, the joint probabilistic structure of these two attributes is studied. Figures 5.5c and 5.5d show the quantile-quantile (Q-Q) plots of LDD and slope for the Headwaters and Methow basins, while Figs. 5a and 5b show the marginal probability distributions functions (PDFs). In the Methow basin, the LDD and slope PDFs follow each other up to the 92th quantile after which the tails of the two distributions diverge as evidenced by their deviation from the line passing through the 0.25 and 0.75 quantiles. However, this breaking point for the Headwaters basin takes place at the 76th quantile, indicating that higher slopes do not necessarily support higher LDDs. The position of all channels with LDD and slope beyond the Q-Q plot's breakpoint are mapped on the Headwaters and Methow river networks as depicted in Figs. 5.5e and 5.5f, respectively. It is seen that these channels are located throughout the Methow basin while they are concentrated within the HSR in the Headwaters basin. Indeed, the western part of the Headwaters landscape has been confined in space creating competition for the developing channels, resulting in the formation of long and fairly parallel low-order channels. Such a preferential dissection and reduced LDD variability at small spatial scales once again is a signature of the strong influence of external forcings, geologic control in this basin, on the landscape organization, leading to deviation from the typical relationships under S-S.

It is interesting to report that the same analysis performed on the Bluestone River Basin showed a breakpoint of the Q-Q plot of the LDD-Slope at approximately the same 75 quantile. Although we are far from making a general conclusion about the quantile of the occurring breakpoint for self-dissimilar landscapes, it is apparent that this Q-Q plot can serve as an indicator of deviation from S-S and the presence of heterogeneity in the spatial organization of a landscape and deserves further study.

Having demonstrated that large-scale geologic controls leave distinct signatures on landscape organization at much smaller scales, our next goal is to quantify the specific spatial scales of preferred dissection. For this, we need appropriate tools such as localized decomposition to interrogate the landscape locally. This issue is examined in the next section.

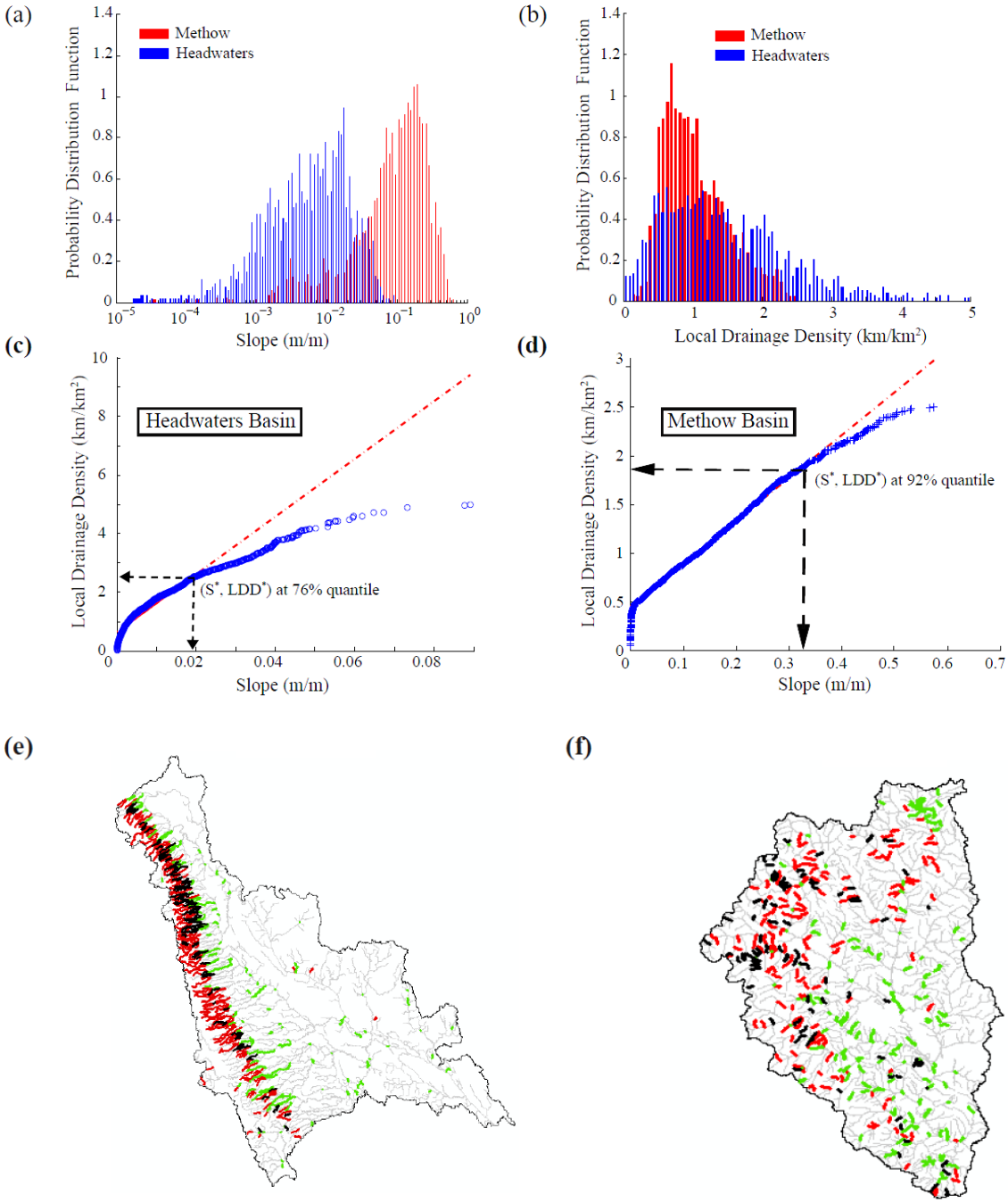

Figure 5.5. Probabilistic comparison of the channel slope and LDD in the Headwaters and Methow basins. (a) and (b) give the channel slope and LDD probability distribution function, respectively. (c) and (d) shows the quantile-quantile plots of the LDD versus slope for the Headwaters and Methow basins, respectively. In these plots, S* and LDD*

Figure 5.5. (Continued) correspond to the breakpoint at which the curve deviates from the 0.25 and 0.75 quantile line. In panels (e) and (f), green channels have slope larger than S*, red channels have LDD larger than LDD*, and black channels are those having both slope larger than S* and LDD larger than LDD*. Concentration of these channel in the Headwaters' high slope region (HSR) is apparent, while they are distributed all over the place in the Methow basin.

5.4. Landscape Multi-Scale Analysis and Preferred Scales of Organization

Multi-scale filtering of landscapes for isolating features within a desired range of scales can be achieved by spectral analysis via Fourier Transform (FT) or Wavelet Transform (WT). Both the FT and the WT perform a convolution of the landscape topography with a family of functions, that is, the sine and cosine functions for the FT and the wavelet functions for the WT. In spite of the widespread application of the FT to study topographic data [e.g., *Ansoult*, 1989; *Hough*, 1989; *Cheng et al.*, 2000; *Wörman et al.*, 2007; *Perron et al.*, 2008; *Booth et al.*, 2009; *Orloff et al.*, 2013], its disadvantages include the lack of spatial localization and the prerequisite for parametric removal of large-scale trends or non-stationarities in the data before the FT can be applied. Instead, the WT is a localized transform in space and frequency and allows for the non-parametric removal of trends by appropriate selection of the mother wavelet [see the classic book of *Mallat*, 1999; *Kalbermatten et al.*, 2012; *Doglioni and Simeone*, 2014; *Foufoula-Georgiou and Kumar*; 2014].

The WT of a function $f(t)$ is defined as

$$WTf(\lambda, b) = < f(t), \psi^*_{\lambda,b}(t) > = \int_{-\infty}^{+\infty} f(t)\psi^*_{\lambda,b}(t)dt \qquad (5\text{-}1)$$

where $< \cdot, \cdot >$ denotes the inner product (convolution) of $f(t)$ with a family of functions $\psi^*_{\lambda,b}(t)$ which are the complex conjugates of the wavelet function $\psi_{\lambda,b}(t)$, expressed as

$$\psi_{\lambda,b}(t) = \frac{1}{\sqrt{\lambda}}\psi\left(\frac{t-b}{\lambda}\right), \qquad \lambda > 0 \qquad (5\text{-}2)$$

where λ is the scale and *b* is the location parameter controlling the contraction (or dilation) and translation of the mother wavelet ψ(*t*), respectively. A wavelet function has zero mean, i.e., $\int_{-\infty}^{+\infty}\psi(t)dt=0$, although higher order momemts may also be zero allowing removal of polynomial trends upto degree *N*, that is, $\int_{-\infty}^{+\infty}t^{k}\psi(t)dt=0,\ k=0,...,N-1$.

5.4.1. Quantifying Preferred Scales of Organization

The wavelet power spectrum (WPS) of topography measures how the variance of the topography is distributed across scales. Contrary to the Fourier spectrum, it offers the advantage of non-parametric surface detrending and also minimizing aliases via the space-frequency localization property of wavelets [*Mallat,* 1999]. Here we use the Mexican hat wavelet (which has two zero moments and thus removes polynomial trends of order 2) to compute the continuous WPS. A number of past studies have reported that the topography is typically scale-invariant and the power spectrum (*PS*) obeys a single power-law scaling relationship with frequency (*f*) according to $PS(f) \propto f^{-\beta}$ [e.g., *Pelletier*, 1999; *Veneziano and Iacobellis*, 1999; *Gagnon et al.*, 2006]. Since the amplitude and the wavelength of topographic features at a given frequency are related to *PS* and *f*, respectively, the spectral slope (β) indicates how the height-to-width ratio of landforms varies with scale. In general, the spectral slope of a self-similar topography computed from a two-dimensional spectrum is equal to 3 (i.e., the landforms' height-to-width ratio is independent of scale), while topographies with spectral slopes other than 3 are categorized as self-affine [see e.g., *Voss*, 1988].

Figures 5.6a and 5.6b show the WPS of the landscape topographies corresponding to a 70 km^2 patch in the Headwaters basin's HSR (see Fig. 5.1d) and a 190 km^2 patch extracted from the Methow basin (marked by the box in Fig. 5.2b), respectively. The WPS of the patch of Methow gives a single spectral slope equal to 2.2 indicating that the

landscape topography is self-affine and obeys the same scaling relationship across a range of scales. However, in the Headwaters' WPS, there are two different scaling regimes with spectral slopes equal to 4.9 and 2.1, separated by a spectral gap between the scales of 0.3 km and 1.5 km. Larger spectral slope above the spectral gap implies that large-scale features (i.e., scales larger than 1.5 km) have larger height-to-width ratio compared to the small-scale features. The presence of the spectral gap documents the existence of some preferred scales of organization corresponding to features whose form is so regular that it does not contribute substantially to the "energy" or variance of the overall signal within that range of scales. Such features correspond to mildly convergent (almost parallel) channels in the Headwaters basin's HSR, and the profile of a cross-section in this region shown in Fig. 5.1d confirms that the scales corresponding to the spectral gap (i.e., 0.3 km to 1.5 km) pertain to the distance between the quasi-periodic ridges and valleys in the HSR. The emergence of a spectral gap, and the presence of two distinctly different scaling regimes around it, is viewed as a signature of "a structured self-dissimilarity" in such landscapes providing information about specific scales of preferred organization and probing the question of understanding the processes that lead to such organization across scales. Topographies that exhibit a break in their power spectra have been reported before, as for example in *Perron et al.* [2008], but landscapes that exhibit a spectral gap over a range of scales have not been reported before to the best of our knowledge.

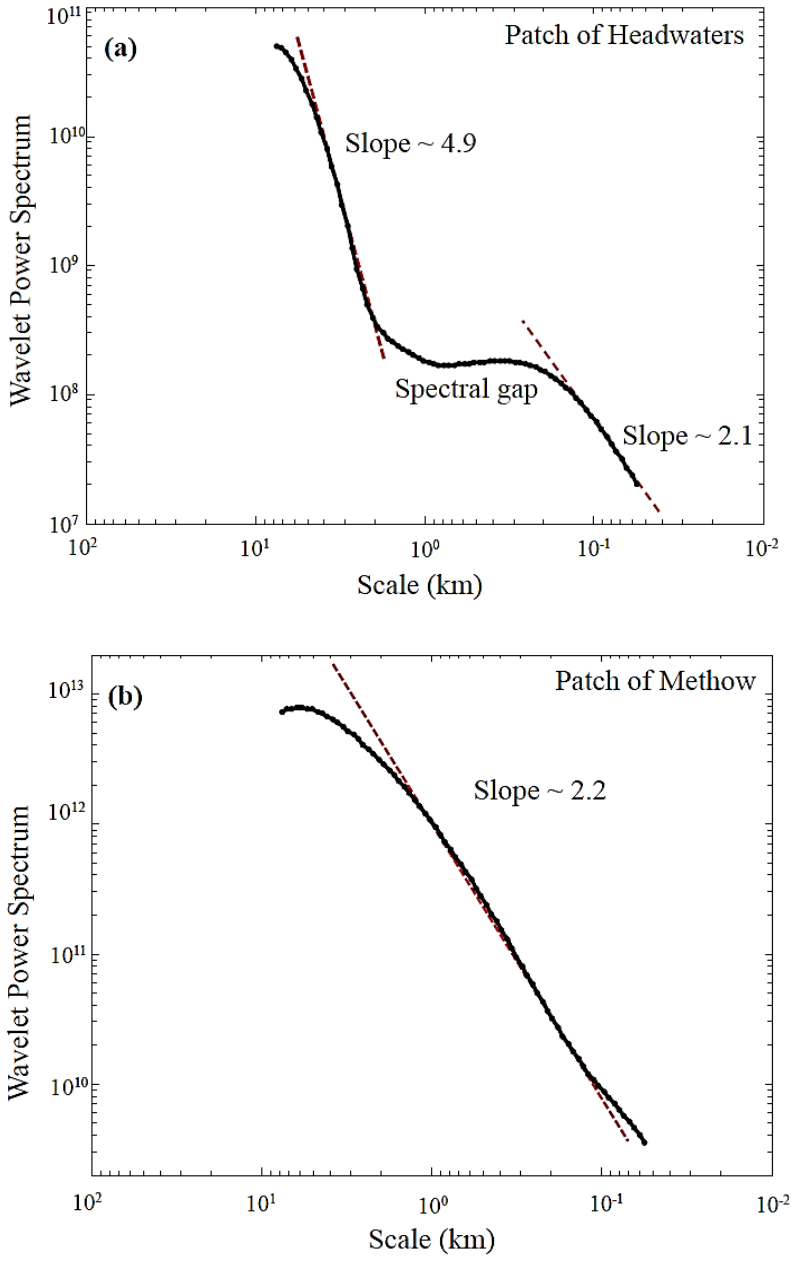

Figure 5.6. Wavelet power spectra. (a) and (b) depict the wavelet power spectrum (WPS) for the patch of Headwaters and Methow basins, respectively. The WPS of the patch of Methow shows a single scaling regime with exponent equal to 2.2 denoting the self-affinity of this landscape. However, the WPS of the patch of Headwaters shows two scaling regimes separated by a spectral gap between scales ~ 0.30 km−1.50 km.

5.4.2. Wavelet Multi-scale Analysis via Multi-Resolution Representation

Although for multi-scale analysis of landscapes the continuous wavelet transform is appropriate, for landscape detrending and reconstruction of local features of interest, a Discrete Wavelet Transform (DWT) is necessary. The discrete wavelet function can be constructed by discretizing the scale and location parameters (usually in a logarithmic scale) written as

$$\psi_{m,n}(t) = \frac{1}{\sqrt{\lambda_0{}^m}} \psi\left(\frac{t - nb_0\lambda_0{}^m}{\lambda_0{}^m} \right) \tag{5-3}$$

where m and n are non-zero integers, λ_0 is a fixed value greater than 1, and b_0 is a positive value. The convolution of $f(t)$ with $\psi_{m,n}(t)$ is called the DWT.

By choosing $\lambda_0 = 2$ and $b_0 = 1$ (called dyadic grid discretization), a certain class of wavelets $\psi(t)$ can be constructed such that $\psi_{m,n}(t)$ are orthogonal to their dilations and translations (i.e., $< \psi_{m,n}(t), \psi_{m',n'}(t) > = \delta_{m,m'}\delta_{n,n'}$, where δ_{ij} is the Kronecker delta function) and form a complete orthonormal basis for all functions that have finite energy. Such functions $f(t)$ can then be written as a linear combination of the wavelets $\psi_{m,n}(t)$, i.e.,

$$f(t) = \sum_{m=-\infty}^{+\infty} \sum_{n=-\infty}^{+\infty} < f(t), \psi_{m,n}(t) > \psi_{m,n}(t) \tag{5-4}$$

where the weights are the inner products of $f(t)$ with the corresponding wavelet function $\psi_{m,n}(t)$. *Mallat* [1989a, b] showed that there exists a unique function $\varphi(t)$, called the *scaling function*, such that $f(t)$ can also be written as

$$f(t) = \sum_{n=-\infty}^{\infty} < f(t), \varphi_{m_0,n}(t) > \varphi_{m_0,n}(t) + \sum_{m=-\infty}^{m_0} \sum_{n=-\infty}^{\infty} < f(t), \psi_{m,n}(t) > \psi_{m,n}(t) \tag{5-5}$$

where the first term in the RHS represents the average or approximation of $f(t)$ at scale m_0 and the second term captures all the "details" of $f(t)$ at scales equal and smaller than m_0. The scaling function is defines as

$$\varphi_{m,n}(t) = \frac{1}{\sqrt{2^m}} \varphi\left(2^{-m} t - n\right) \tag{5-6}$$

which: (1) is an averaging function, i.e., $\int_{-\infty}^{+\infty} \varphi(t) dt = 1$; (2) is orthogonal to all wavelets, i.e., $< \varphi_{m,n}, \psi_{m',n'} >= 0$, and to all of its translations, i.e., $< \varphi_{m,n}, \varphi_{m,n'} >= \delta_{n,n'}$ at any fixed scale m; and (3) can be obtained as a linear combination of translations of scaled versions of itself (the so-called two-scale difference equation):

$$\varphi(t) = \sqrt{2} \sum_k h_k \varphi(2t - k) \tag{5-7}$$

The scaling and the wavelet functions relate to each other such that

$$\psi(t) = \sqrt{2} \sum_k g_k \varphi(2t - k) \tag{5-8}$$

where h_k are the scaling coefficients and g_k are the wavelet coefficients computed from h_k through $g_k = (-1)^k h_{1-k}$ [see also *Daubechies*, 1988]. The scaling coefficients satisfy the following conditions:

1) Compact support width requirement gives: $h_k = 0; \quad \forall k \notin \{0,1,...,2N-1\}$
2) The normalization property reflects to: $\sum_{k=0}^{2N-1} h_k = \sqrt{2}$
3) The function $\psi(t)$ has N vanishing moments if: $\sum_{k=0}^{2N-1} (-1)^k k^l h_k = 0; \quad l = 0,...,N-1$
4) Integer translation and dilation of $\varphi(t)$ and $\psi(t)$ form an orthogonal family if:

$$\sum_{k=0}^{2N-1} h_{k-2p} h_{k-2l} = \delta_{p,l}; \quad \forall k,l$$

It can be easily shown from Eq. (5-5) that the following recursive equation can be written

$$\tilde{f}_{m-1}(t) = \tilde{f}_m(t) + f'_m(t) \tag{5-9}$$

implying that a function approximation at scale *m*-1, $\tilde{f}_{m-1}(t)$, can be written as the sum of the function approximation at the immediately smaller scale *m*, $\tilde{f}_m(t)$, plus its detail at that scale, $f'_m(t)$.

Equation (5-9) constitutes the so-called wavelet multi-resolution representation [*Mallat*, 1989a]. Multi-resolution representation allows for detrending a landscape through the inverse DWT by successive elimination of large-scale features from the topography to better characterize the complex hierarchy of topographic features. From here on, a detrended landscape is denoted by $H_m(t, s)$ and is obtained by setting the approximation coefficients at scale *m* to zero in the reconstruction operation. Figures 5.7a and 5.7b schematically show the general procedure for the multi-resolution decomposition and detrending of a landscape in two dimensions. To analyze two-dimensional topographic data such as DEMs, two-dimensional orthonormal bases can be constructed by taking the tensor product of the one-dimensional scaling and wavelet bases given above [see Appendix B for more detail]. If the bandpass center frequency of the chosen mother wavelet is f_c, and the data sampling period (which is the resolution of the DEM) is denoted by Δ, the physical scale (L_m) relating to the scale *m* is computed by using the following relationship.

$$L_m = \frac{2^m \cdot \Delta}{f_c} \tag{5-10}$$

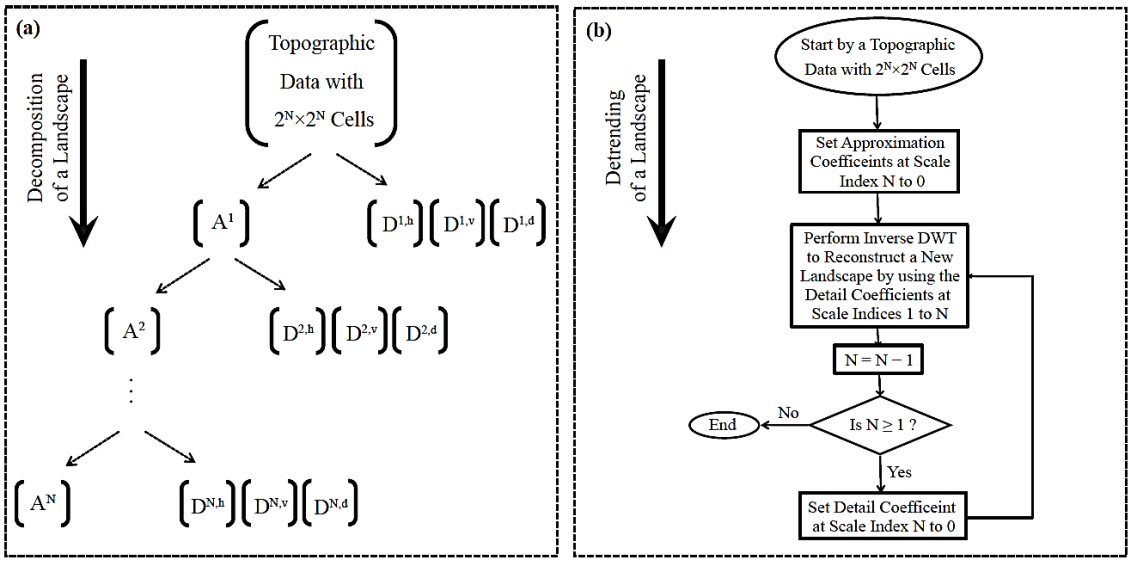

Figure 5.7. General procedure for the decomposition and detrending of a landscape. (a) Shows schematic diagram of the multi-resolution representation of a landscape using two-dimensional DWT. At the first level of decomposition, the transformed input array is split into four sub-matrices: the approximation matrix A^1, the horizontal detail matrix $D^{1,h}$, the vertical detail matrix $D^{1,v}$, and the diagonal detail matrix, $D^{1,d}$. In the next level, the detail coefficients at scale index 1 are remained untouched, and the approximation matrix is further decomposed into three sub-matrices of detail and one matrix of approximation at scale index 2. If the original landscape consists of $2^N \times 2^N$ components, under dyadic grid discretization, this procedure can be repeated N times resulting in coefficient sub-matrices A^N, $D^{1,h}$, $D^{1,v}$, and $D^{1,d}$ at scale index N. (b) Gives the flowchart of the multi-scale detrending of a landscape using two-dimensional DWT. For a $2^N \times 2^N$ input topographic array, the detrending procedure starts by setting the approximation coefficients at the largest scale to 0. In the next iterations, the detail coefficients from large to small scales are successively set to 0 until all the details are removed from the landscape.

5.4.3. Selection of the Wavelet Type and Illustration on the Comparison between Different Daubechies Wavelets

The simplest and most widely used discrete orthonormal wavelet is the Haar wavelet which is, however, poorly localized in frequency. Instead, the Daubechies wavelets [*Daubechies*, 1988; 1992] have enhanced localization in the frequency domain and

allow for removal of high order polynomial trends as needed. Daubechies wavelets with K number of vanishing moments are denoted by DBK, e.g., DB2, DB5, etc. Figure 5.8 shows the scaling and the wavelet functions with the energy spectrum of the Haar, DB2, and DB5 wavelets. It is seen that there is no symmetry or anti-symmetry axis in the Daubechies scaling and wavelet functions (with $K \geq 2$). In fact, the Haar basis is the only orthonormal basis of compactly supported wavelets for which the scaling function has a symmetry axis. Also as the number of the scaling coefficients increases (i.e., wavelet with higher vanishing moments), regularity in φ and ψ increases linearly with the support width [see *Daubechies*, 1998 for formal proof]. This enhances the wavelet localization in the frequency domain, though at the cost of a wider support width. It is also seen how the energy spectrum of the wavelet function becomes flatter as the number of vanishing moments increases.

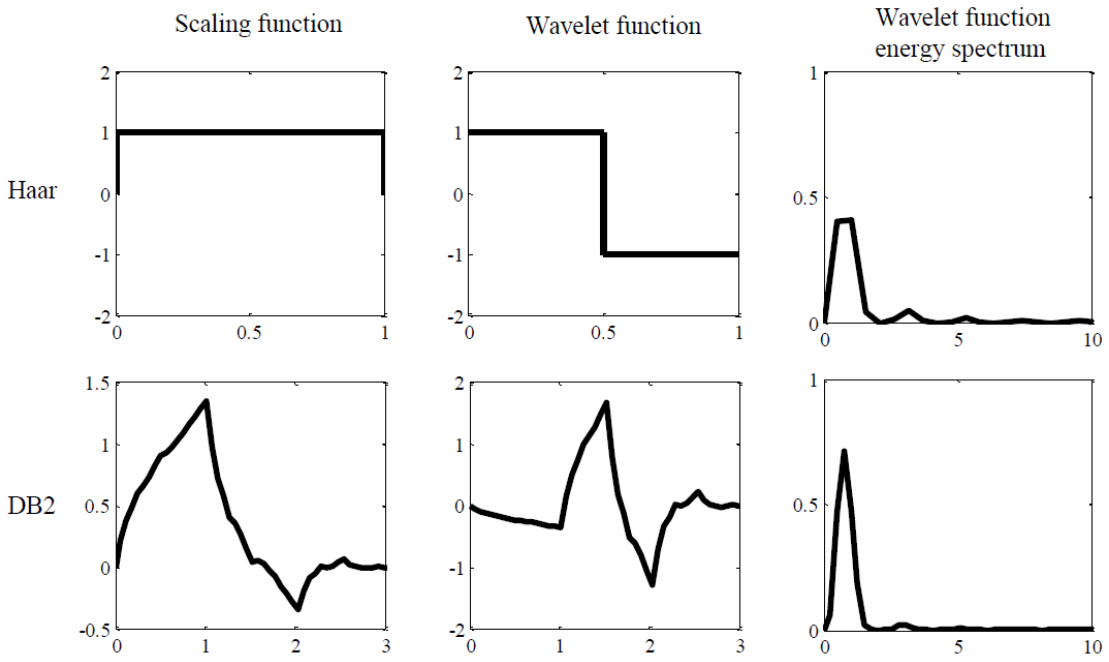

Figure 5.8. Wavelet and scaling function, and the energy spectrum of the Haar, DB2, and DB5 wavelets. All wavelets and scaling functions are shown over their support width.

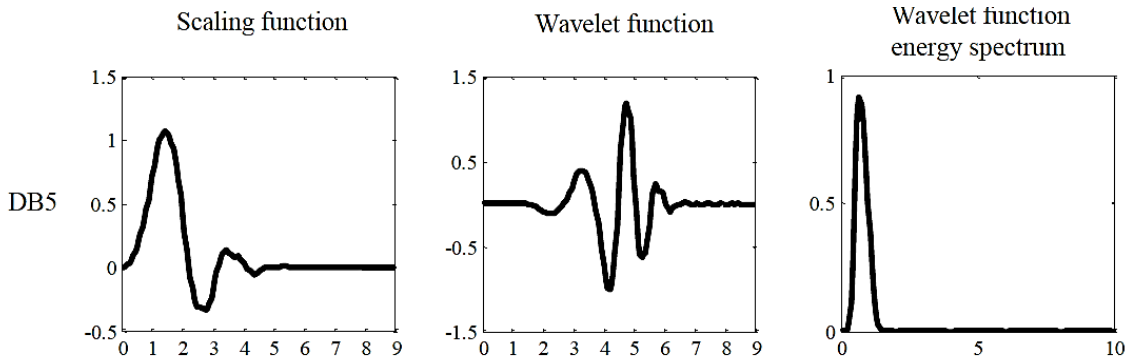

Figure 5.8 (continued). Wavelet and scaling function, and the energy spectrum of the DB5 wavelet. The wavelets and scaling functions are shown over their support width.

We chose the most suitable wavelet for our analysis by testing different Daubechies wavelets, i.e., DB1, DB2, …, DB10 on one hypothetical surface generated by combining a Gaussian noise and two sinusoids (Fig. 5.9a), as well as two patches within the Headwaters and Methow basins (Figs. 5.9b and 5.9c, respectively). The best wavelet would be the one resulting in the least squares difference between the original landscape and the detrended landscape containing the approximation coefficients at the largest scale (which give the spatial trend in topography). We found DB5 the best wavelet for all landscapes with respect to our criterion as it provided a balance between removal of trends and efficiency in the spatial localization compared to other wavelets. Figures 5.9d-5.9l compare the ability of the Haar, DB2, and DB5 wavelets (as examples) to detect spatial trend in different landscapes. It is seen how the use of the Daubechies wavelets with higher number of vanishing moments improves the identified spatial trend due to their enhanced localization property.

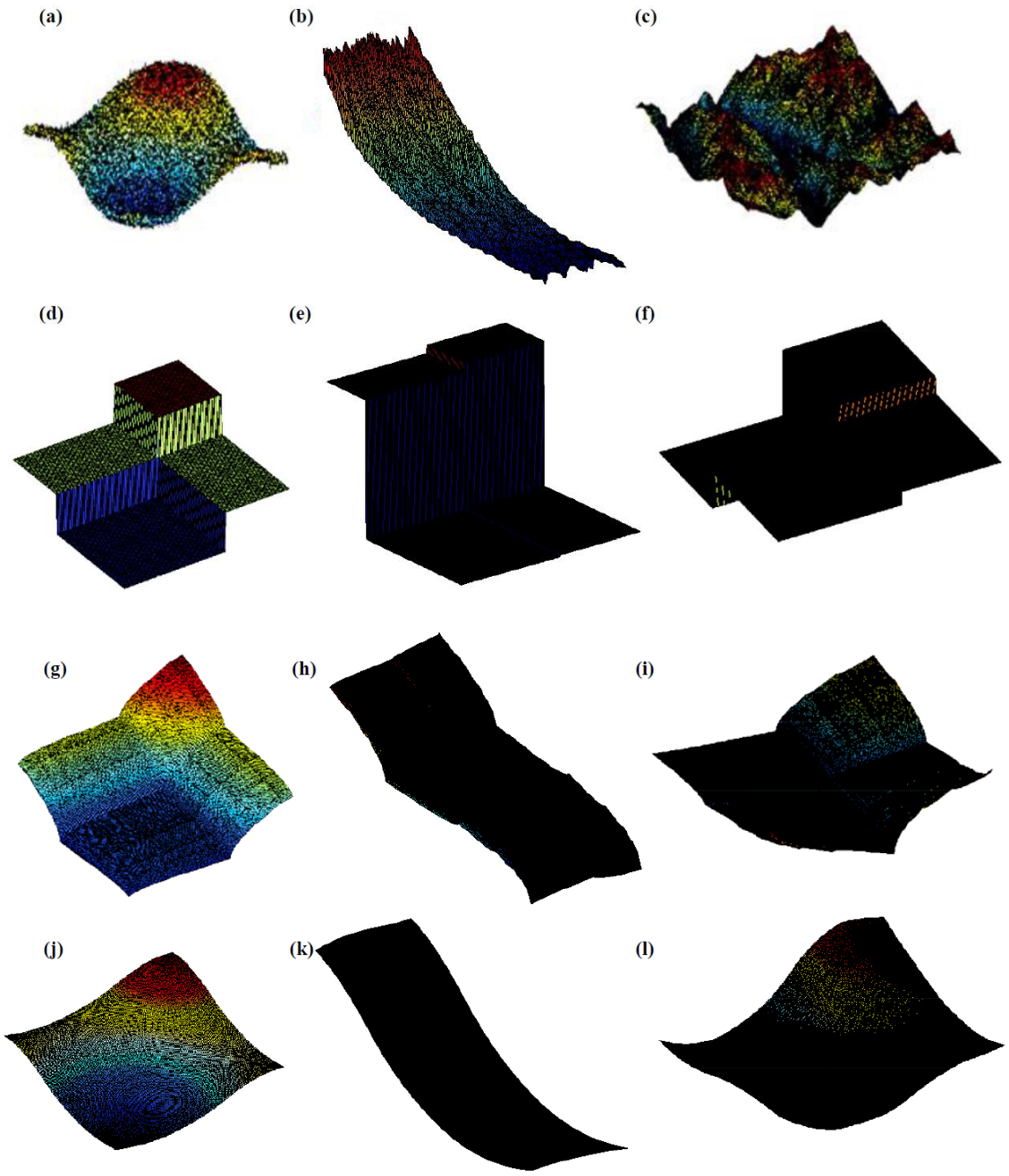

Figure 5.9. Illustration of the Daubechies wavelets ability in identifying the spatial trend in landscapes with different topographies. (a-c) Depict an experimental surface generated by combining a Gaussian noise and two sinusoids, and two patches within the Headwaters and Methow basins. (d-f), (g-i), and (j-l) show the spatial trend in the landscapes detected by using the Haar, DB2, and DB5 wavelets, respectively.

Figure 5.10 further shows the scaling and three directional wavelet functions of the DB5 wavelet in two dimensions. These functions are derived by the tensor product of the one-dimensional scaling and wavelet functions such that the scaling function and the vertical, horizontal, and the diagonal wavelet functions are the tensor products of (φ, φ), (φ, ψ), (ψ, φ), and (ψ, ψ), respectively. The scaling coefficients for the one-dimensional DB5 wavelet can be computed numerically by solving the set of equations (1-4) given in section 5.2, resulting in c_0 = 0.160102397974, c_1 = 0.603829269797, c_2 = 0.724308528438, c_3 = 0.138228145901, c_4 = 0.242294887066, c_5 = 0.032244869585, c_6 = 0.077571493840, c_7 = 0.006241490213, c_8 = 0.012580751999, c_9 = 0.003335725285. The corresponding wavelet coefficients can be computed easily from the scaling coefficients by using the expression given for g_k.

5.4.4. Characterizing Landscape Regularity via Multi-Scale Detrending

The structure of regular features identified by the spectral gap can be spatially located and statistically characterized by successively filtering out the larger scale features from the landscape through multi-scale detrending. Figures 5.11a and 5.11b show the elevation probability distributions of the detrended landscapes ($H_m(t, s)$, m = 1, …, 8) for the Headwaters and Methow patches, respectively. The common observation is that by gradual removal of the large scale features, the elevation probability distribution becomes smoother and more symmetrical. However, the shape of the probability distributions from one level of detrending to another does not change similarly in the patches. Indeed, if the variance of the probability distributions is plotted against scale as

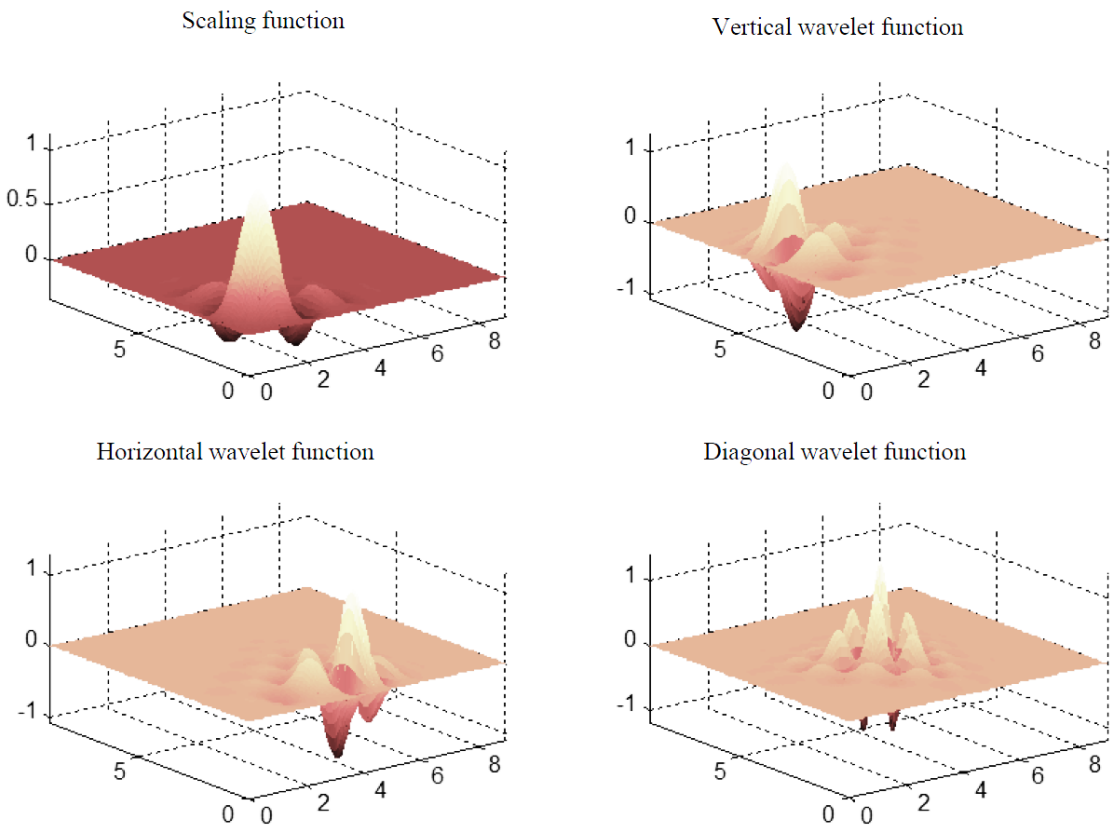

Figure 5.10. Two-dimensional scaling function and three directional wavelet functions for the DB5 wavelet. These functions are derived by the tensor product of the one-dimensional scaling and wavelet functions such that the scaling, vertical, horizontal, and the diagonal wavelet functions are the tensor products of (φ, φ), (φ,ψ), (ψ,φ), and (ψ,ψ), respectively.

shown in Figs. 5.11c and 5.11d, it is seen that the variability changes proportionally across scales in the patch of Methow (as expected for self-similar landscapes), while the variance of the probability distributions does not change significantly by filtering out the features with wavelength between 0.36 km and 1.44 km from the patch of Headwaters basin. Figure. 5.11e depicts the structure of the detrended landscape, $H_4(t, s)$, as an example that contains all topographic features with spatial scale equal and less than 0.72 km. The regularity of the features is apparent in this detrended landscape, which

corresponds to the quasi-periodic ridges and valleys in the Headwaters basin's HSR and their wavelengths are consistent with the scales already revealed by the spectral gap in the WPS of this landscape.

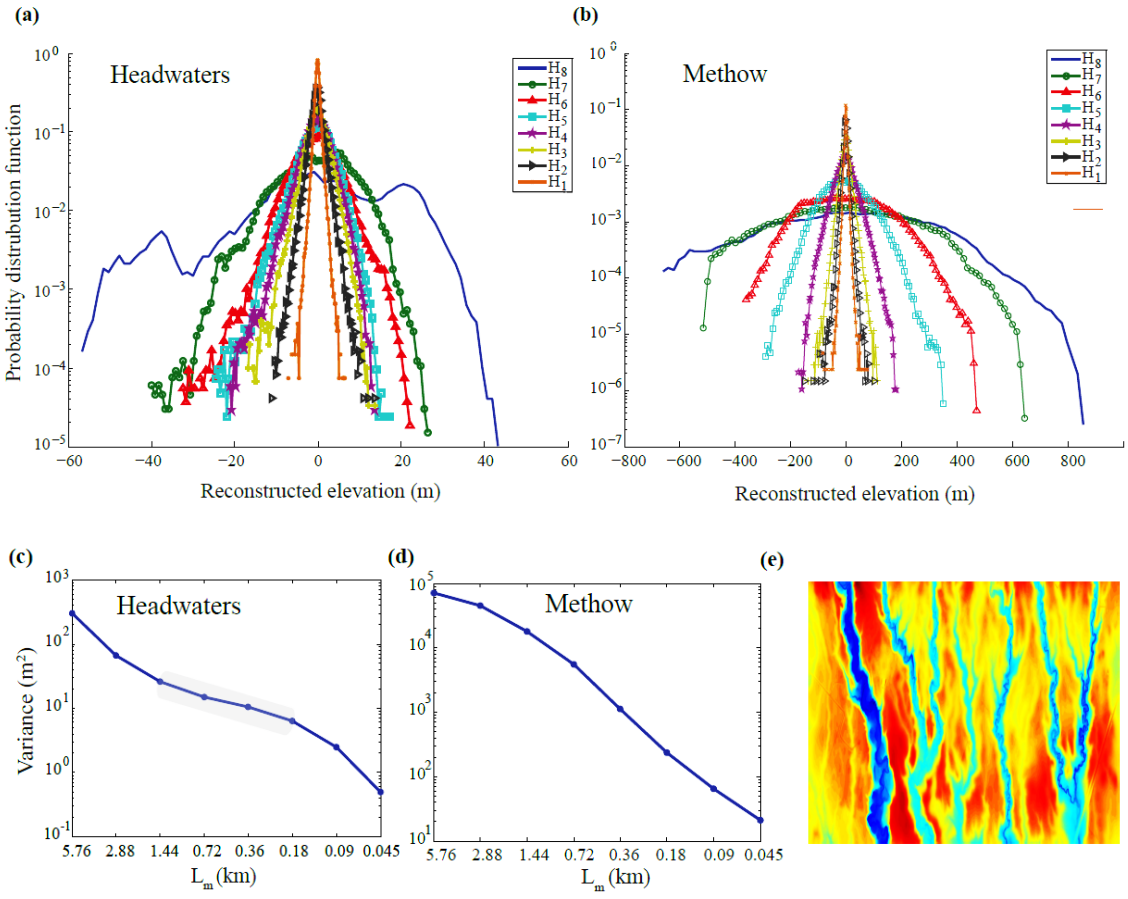

Figure 5.11. Elevation probability distribution and the variance of detrended landscapes against scale. (a-b) shows the probability distribution of the detrended landscapes for the patch of Headwaters and Methow, respectively. (c-d) gives the variance of the detrended landscapes, H_m (t, s), against scale, L_m. The horizontal axis in these plots gives the largest scale present in H_m (t, s). Reduction in the rate of change of variability in the patch of Headwaters is observed by removing features with scales 0.36 km-1.44 km, while the variance changes proportionally across scales in the patch of Methow. (e) depicts the image view of the detrended landscape, $H_4(t, s)$, from the patch of Headwaters. By filtering out features with spatial scale larger than 0.72 km from the landscape, the resulting detrended topography shows regularity that corresponds to the quasi-periodic ridges and valleys in the Headwaters' high slope region.

5.5. Conclusions

Landscapes possess a hierarchical variability over a wide range of scales: from hillslopes, to valleys, to nested river basins of increasing order. If the physical processes that sculpted a landscape are spatially homogeneous, then it is expected that some kind of order in how this variability changes with scale will be found. In fact, a considerable body of work has centered over the past three decades on quantifying these symmetries and self-similarity (S-S) in landscape dissection [e.g., see *Rodríguez-Iturbe and Rinaldo*, 2001]. However, if geologically or geomorphologically spatially heterogeneous processes dominated the landscape evolution, one would expect that this heterogeneity will be reflected over some range of scales which would exhibit different spatial organization and variability than other scales. The purpose of this study was to examine landscapes which exhibit spatial heterogeneity in their dissection, and via localized analysis and synthesis identify and quantify scales of preferred organization and relate them to the underlying geologic controls. We call these landscapes "self-dissimilar" and suggest that research is needed to both theoretically characterize these landscapes and to connect their structure to the underlying climatic, tectonic, or geologic mechanisms that have broken the typical symmetries that most landscapes possess. From the analysis presented here, the following conclusions are made:

1) Even in basins which exhibit visually distinct spatially heterogeneous river branching structures, Hortonian self-similarity (HSS) analysis is unable to capture broken symmetries in network topology. However, the stricter Tokunaga self-similarity (TSS) analysis can detect the presence of hierarchical irregularities in the branching structure of the river networks.

2) The probabilistic dependence of local slope and local drainage density (LDD), examined via a quantile-quantile analysis, has the potential to quantify spatial heterogeneities in landscape dissection by a disproportional lack of high LDD at high slopes. Such an analysis is easy to perform and can be a first step in detecting

spatial heterogeneities in landscape dissection, which then can be explicitly positioned on the landscape to study cause and effect.

3) The presence of a spectral gap (no net increase in energy with increasing scale) in the wavelet power spectrum (WPS) can reveal scales at which excess regularity is present, as for example in the quasi-periodic ridges and valleys, in our case.

4) Using appropriate localized multi-scale filters, the structure of topographic features with preferred scales of organization can be quantified via localized multi-scale detrending by successive removal of features from the largest to the smallest scale of interest.

The analysis presented herein highlighted the need to develop formal methods for studying spatially heterogeneous landscapes in order to understand their drainage structure and relate it to the underlying causative mechanisms. Such an analysis should be performed in many more basins, including those where anthropogenic influences have disturbed the landscape natural evolution, so that a path to a more formal framework for characterization of self-dissimilar landscapes is developed.

6

Concluding Remarks and Future Perspectives

The scope and magnitude of anthropogenic interventions during past decades have undeniably affected water and solute transport and fate in intensively managed landscapes, altering regional and global biochemical cycling. This dissertation has developed a quantitative framework within which first-order estimates of the relative changes in travel time statistics in those landscapes undergoing substantial alterations in land-use land-cover (LULC) can be quantified. Regarding the lack of high spatiotemporal resolution hydro-chemical data required for an accurate estimation of transport time scales, this work has explored whether a lumped system representation via a time-varying stochastic Lagrangian formulation can provide reliable estimates of mean travel time (MTT) in spatially heterogeneous catchments in the absence of within-catchment observations. As the river network structure (which is typically considered self-similar) might impose a significant control on the in-stream transport time scales and be used to explain some properties of the relating physical processes, we further explored those river networks that do not obey the typical self-similar relationships over a range of spatial scales. We proposed methodologies that can probe into the structure of such outlier basins (which we call self-dissimilar) in ways that are able to reveal their

spatially heterogeneous organization and preferential scales of dissection, which in turn might influence the transport and storage time scales at large-scale catchments with implications for solute transport and water quality.

The main results of this work can be summarized as

1) By employing the theory of time-variant travel time distributions (TTDs) within a stochastic Lagrangian transport formulation in the Redwood River Basin (one of major sub-basins of the Minnesota River Basin (MRB) located in the Upper Midwestern U.S.), we found that the MTT has considerably decreased post-1975 (when extensive expansion of subsurface tile drainage and a change in the daily hydrologic response have been documented), compared to the pre-1975 period, during all months with the maximum reduction during the growing season (e.g., reduction by 41 percent in the month of June). This was attributed to the intensification of tile drainage that can effectively extract the excess soil moisture from the subsurface by providing extra pathways through which water is delivered to the streams much faster compared to the natural transport within the soil matrix. The year-to-year variability of the MTT was also found to be highly reduced in the presence of extensive subsurface tile drainage, indicating that the "filtering" of the natural heterogeneity via the artificially re-plumbed landscape results in a time-space homogenization of the hydrologic response and an overall system that responds to climatic variability in a more predictable way.

2) It was shown that a time-varying TTD (within a stochastic Lagrangian transport formulation) results in MTTs that are unbiased to the aggregation of spatial heterogeneity under the random sampling assumption, and not significantly biased under other sampling schemes. This finding reinforces the importance of such a time-variant lumped formalism to appropriately predict the catchment's mean transport time scales without the need to explicitly characterize and embed small-scale spatial heterogeneity.

3) Although significant variability of MTT exists at the small catchment scale, there exists a characteristic spatial scale above which the MTT converges to a constant value not influenced by the aggregation of smaller-scale spatial heterogeneity. The ratio between the catchment characteristic scale and the mean incremental area of the catchment was found to be on average independent of the river network topology and spatial arrangement of incremental areas.

4) Hortonian self-similarity (HSS) analysis was shown to be unable to capture broken symmetries in network topology even in catchments exhibiting visually distinct spatially heterogeneous river branching structures. However, the stricter Tokunaga self-similarity (TSS) analysis could detect the presence of hierarchical irregularities in the branching structure of the river networks.

5) The probabilistic dependence of local slope and local drainage density (LDD), examined via a quantile-quantile analysis, was shown to have the potential to quantify spatial heterogeneities in landscape dissection by a disproportional lack of high LDD at high slopes. Such an analysis is easy to perform and can be a first step in detecting spatial heterogeneities in landscape dissection, which then can be explicitly positioned on the landscape to study cause and effect.

6) The presence of a spectral gap (no net increase in energy with increasing scale) in the wavelet power spectrum (WPS) can reveal scales at which excess regularity is present in a landscape, as for example in the quasi-periodic ridges and valleys, in the MRB. Using appropriate localized multi-scale filters, the structure of topographic features with preferred scales of organization can be quantified via localized multi-scale detrending by successive removal of features from the largest to the smallest scale of interest.

Future Research: Some of the future research directions can be outlined as follows.

- One of the key components of the theory of time-variant TTD is the Storage Selection (SAS) function characterization, which integrates the effects of heterogeneity in flowpaths and dispersion mechanisms dictating the water and solute transport through a hydrologic system. Nevertheless, as emphasized in Chapter 3, availability of long time series of high resolution hydro-chemical data for input and output fluxes is necessary for inferring the appropriate form of the SAS function for a catchment of interest, which is usually a challenge in practical applications. Future research on this context can then focus on: (1) unravelling how the shape of the SAS function varies across hierarchical spatial scales of a catchment, and (2) exploring if the SAS function becomes scale-independent after a characteristic spatial scale, which might enable us to parameterize its scale-invariance shape by a specific theoretical probability distribution function.\
- The literature is ample with many experimental and fewer numerical studies attempting to understand the relationship between a catchment mean travel/residence time and its physical characteristics such as drainage area [e.g., *McGlynn et al.*, 2003], flowpath length, flowpath slope, drainage density [e.g., *McGuire et al.*, 2005; *Tetzlaff et al.*, 2009a, 2009b], percentage of hydrologically responsive soils [e.g., *Rodgers et al.*, 2005]; subsurface hydraulic conductivity [e.g., *Maxwell et al.*, 2016], groundwater contribution [e.g., *Soulsby et al.*, 2006], aspect [e.g., *Broxton et al.*, 2009], and topographic wetness index [e.g., *Asano and Uchida*, 2012], among others. However, some of these relationships are inconsistent, mostly attributed to the fact that the dominant influence of climate should be first considered and removed from the data before assessing the actual influence of topographic indices on MTTs [*Heidbüchel et al.*, 2013; *Seeger and Weiler*, 2014], mainly because these catchments' characteristics typically co-evolve with climate [*Troch et al.*, 2013]. Such a consideration requires controlled

simulations (through numerical models) by which the distinct influence of a catchment's physical property on the transport time scales can be explored while keeping other attributes unchanged.

- Via Monte-Carlo simulations of a stochastic soil moisture model, *Botter et al.* [2010] and *Botter* [2012] found that MTTs in a hillslope are clearly dependent on the hydro-climatic features of a basin, that is, the MTTs in wet climates are smaller than those observed in dry climatic conditions. This obviously implies that the magnitude of the MTT at the catchment's larger scales is also to some degree controlled by climate. Moreover, *Danesh-Yazdi et al.* [unpublished work, 2016] found that rainfall inter-arrival time seems to be a more dominant control on the MTT than the rainfall depth, but not necessarily at all frequencies and depths. This observation suggests that it is the interplay between different rainfall characteristics such as rainfall depth, rainfall inter-arrival time, and rainfall duration that determines the water particles' waiting and remobilization time scales, which is still poorly understood and needs to be further studied. This research would also unravel the relationship between the magnitude of the MTT at the catchment's spatial characteristic scale (i.e., the scale above which the MTT does not vary with spatial aggregation of heterogeneity) and the rainfall aforementioned characteristics.

References

Allen, R.G., I. A. Walter, R. Elliott, T. Howell, and D. Itenfisu (2005), ASCE's standardized reference evapotranspiration equation, *ASCE-EWRI Task Committee Report*.

Ansoult, M. (1989), Circular sampling for Fourier analysis of digital terrain data, *Mathematical geology*, *21*(4), 401–410.

Arheimer, B., and H. B. Wittgren (2002), Modelling nitrogen removal in potential wetlands at the catchment scale, *Ecological engineering*, *19*(1), 63-80.

Asano Y., and T. Uchida (2012), Flow path depth is the main controller of mean base flow transit times in a mountainous catchment, *Water Resour. Res.*, *48*, W03512. DOI: 10.1029/2011WR010906.

Ayalew, T. B., W. F. Krajewski, and R. Mantilla (2014), Connecting the power-law scaling structure of peak-discharges to spatially variable rainfall and catchment physical properties, *Advances in Water Resources*, *71*, 32–43.

Ayars, J. E., and R. G. Evans (2015), Subsurface drainage: what's next?, *Irrig. and Drain.*, *64*, 378–392.

Basu, N. B., S. E. Thompson, and P. S. C. Rao (2011), Hydrologic and biogeochemical functioning of intensively managed catchments: A synthesis of top-down analyses, *Water Resour. Res.*, *47*(10).

Belmont, P., et al. (2011), Large shift in source of fine sediment in the Upper Mississippi River, *Environmental science & technology*, *45*(20), 8804–8810.

Benettin, P., A. Rinaldo, and G. Botter (2013a), Kinematics of age mixing in advection-dispersion models, *Water Resour. Res.*, *49*(12), 8539–8551, doi:10.1002/2013WR014708.

Benettin, P., Y. Velde, S. E. Zee, A. Rinaldo, and G. Botter (2013b), Chloride circulation in a lowland catchment and the formulation of transport by travel time distributions, *Water Resour. Res.*, *49*(8), 4619–4632.

Benettin, P., J. W. Kirchner, A. Rinaldo, and G. Botter (2015a), Modeling chloride transport using travel time distributions at Plynlimon, Wales, *Water Resour. Res.*, *51*(5), 3259–3276, doi:10.1002/2014WR016600.

Benettin, P., A. Rinaldo, and G. Botter (2015b), Tracking residence times in hydrological systems: forward and backward formulations: Forward and Backward TTD, *Hydrol. Process.*, *29*(25), 5203–5213.

Birkel, C., and C. Soulsby (2015), Advancing tracer-aided rainfall-runoff modelling: a review of progress, problems and unrealised potential: Advancing Tracer-aided Rainfall-Runoff Modelling, *Hydrol. Process.*, *29*(25), 5227–5240.

Birkel, C., C. Soulsby, and D. Tetzlaff (2011), Modelling catchment-scale water storage dynamics: reconciling dynamic storage with tracer-inferred passive storage, *Hydrol. Processes*, *25*(25), 3924–3936.

Birkel, C., C. Soulsby, D. Tetzlaff, and S. Dunn (2012), High-frequency storm event isotope sampling reveals time-variant transit time distributions and influence of diurnal cycles, *Hydrol. Processes*, *26*(2), 308–316, doi:10.1002/hyp.8210.

Blann, K. L., J. L. Anderson, G. R. Sands, and B. Vondracek (2009), Effects of agricultural drainage on aquatic ecosystems: a review, *Critical Reviews in Environmental Science and Technology*, *39*(11), 909–1001.

Boland-Brien, S. J., N. B. Basu, and K. E. Schilling (2014), Homogenization of spatial patterns of hydrologic response in artificially drained agricultural catchments, *Hydrol. Processes*, *28*(19), 5010–5020.

Booth, A. M., J. J. Roering, and J. T. Perron (2009), Automated landslide mapping using spectral analysis and high-resolution topographic data: Puget sound lowlands, Washington, and Portland hills, Oregon, *Geomorphology*, *109*(3), 132–147.

Botter, G., and A. Rinaldo (2003), Scale effect on geomorphologic and kinematic dispersion, *Water Resour. Res.*, *39*(10).

Botter, G., E. Bertuzzo, and A. Rinaldo (2010), Transport in the hydrologic response: Travel time distributions, soil moisture dynamics, and the old water paradox, *Water Resour. Res.*, *46*(3).

Botter, G., E. Bertuzzo, and A. Rinaldo (2011), Catchment residence and travel time distributions: The master equation, *Geophysical Research Letters*, *38*(11).

Botter, G., T. Settin, M. Marani, and A. Rinaldo (2006), A stochastic model of Nitrate transport and cycling at basin scale, *Water Resour. Res.*, *42*(4).

Broxton, P. D., P. A. Troch, and S. W. Lyon (2009), On the role of aspect to quantify water transit times in small mountainous catchments, *Water Resour. Res.*, *45*, W08427, doi:10.1029/2008WR007438.

Brutsaert, W., and J. L. Nieber (1977), Regionalized drought flow hydrographs from a mature glaciated plateau, *Water Resour. Res.*, *13*(3), 637–643.

Cardwell, D. H. (1975), Geologic History of West Virginia, *West Virginia Geological and Economic Survey*, 10.

Cardwell, V. (1982), Fifty years of Minnesota corn production: Sources of yield increase, *Agronomy Journal*, *74*(6), 984–990.

Castelltort, S., and G. Simpson (2006), River spacing and drainage network growth in widening mountain ranges, *Basin Research*, *18*(3), 267–276.

Castelltort, S., G. Simpson, and A. Darrioulat (2009), Slope-control on the aspect ratio of river basins, *Terra Nova*, *21*(4), 265–270.

Chapman, A., I. D. Foster, J. Lees, and R. Hodgkinson (2005), Sediment delivery from agricultural land to rivers via subsurface drainage, *Hydrol. Processes*, *19*(15), 2875– 2897.

Chen, B., W. F. Krajewski, X. Zhou, and M. J. Helmers (2015), Organized variability of surface runoff responses across neighboring hillslopes in Iowa, *Journal of Hydrology*, *523*, 1−13.

Cheng, Q., Y. Xu, and E. Grunsky (2000), Integrated spatial and spectrum method for geochemical anomaly separation, *Natural Resources Research*, *9*(1), 43-52.

Church, M., and O. Slaymaker (1989), Disequilibrium of Holocene sediment yield in glaciated British Columbia, *Nature*, *337*(6206), 452-454.

Clayton, L., and S. R. Moran (1982), Chronology of late Wisconsinan glaciation in middle North America, *Quaternary Science Reviews*, *1*(1), 55–82.

Clement, J.-C., L. Aquilina, O. Bour, K. Plaine, T. P. Burt, and G. Pinay (2003), Hydrological flowpaths and nitrate removal rates within a riparian floodplain

along a fourth-order stream in Brittany (France), *Hydrol. Processes*, *17*(6), 1177–1195.

Cornaton, F. and P. Perrochet (2006), Groundwater age, life expectancy and transit time distributions in advective–dispersive systems: 1. Generalized reservoir theory, *Advances in Water Resources*, 29(9): 1267–1291. DOI:10.1016/j.advwatres.2005.10.009.

Czuba, J. A., and E. Foufoula-Georgiou (2015), Dynamic connectivity in a fluvial network for identifying hotspots of geomorphic change, *Water Resour. Res.*, *51*(3), 1401-1421.

Dagan, G. (1989), Flow and Transport in Porous Formations, *Springer*, New York.

Dahl, T. E. (2000), Status and trends of wetlands in the conterminous united states 1986 to 1997, *Tech. rep.*, US Fish and Wildlife Service.

Danesh-Yazdi, M., E. Foufoula-Georgiou, D. L. Karwan, and G. Botter (2016), Inferring changes in water cycle dynamics of intensively managed landscapes via the theory of time-variant travel time distributions, *Water Resour. Res.*, *52*(10), 7593-7614.

Daubechies, I. (1988), Orthonormal bases of compactly supported wavelets, *Communications on pure and applied mathematics*, *41*(7), 909–996.

Daubechies, I., et al. (1992), *Ten lectures on wavelets*, vol. 61, SIAM.

De Vente, J., J. Poesen, M. Arabkhedri, and G.Verstraeten (2007), The sediment delivery problem revisited, *Progress in Physical Geography*, *31*(2), 155-178.

Dettmann, E. H. (2001), Effect of water residence time on annual export and denitrification of nitrogen in estuaries: a model analysis, *Estuaries*, *24*(4), 481-490.

Discovery Farms Minnesota (2015), Hydro-climate data at Stearns, Dodge, and Blue Earth Sites, Minnesota [Personal Communication].

Doglioni, A., and V. Simeone (2014), Geomorphometric analysis based on discrete wavelet transform, *Environmental Earth Sciences*, *71*(7), 3095–3108.

Dusek, J., T. Vogel, and M. Sanda (2012), Hillslope hydrograph analysis using synthetic and natural oxygen-18 signatures, *Journal of Hydrology*, *475*, 415–427.

Fenicia F., S. Wrede, D. Kavetski, L. Pfister, L. Hoffmann, H.H.G. Savenije, and J.J. McDonnell (2010), Assessing the impact of mixing assumptions on the estimation of streamwater mean residence time, *Hydrol. Processes*, *24*, 1730–1741. DOI: 10.1002/hyp.7595.

Fiori, A., and D. Russo (2008), Travel time distribution in a hillslope: Insight from numerical simulations, *Water Resour. Res.*, *44*(12).

Fiori, A., and D. Russo (2013), Numerical experiments on the age of seasonal rain water in hillslopes, *Procedia Environmental Sciences*, *19*, 331–340.

Foufoula-Georgiou, E., and P. Kumar (2014), *Wavelets in geophysics*, vol. 4, Academic Press.

Foufoula-Georgiou, E., Z. Takbiri, J. A. Czuba, and J. Schwenk (2015), The change of nature and the nature of change in agricultural landscapes: Hydrologic regime shifts modulate ecological transitions, *Water Resour. Res.*, *51*(8), 6649–6671.

Fraser, H., R. Fleming, and P. Eng (2001), Environmental benefits of tile drainage, *Prepared for: LICO. Land Improvement Contractors of Ontario*, Ridgetown College, University of Guelph.

Gagnon, J.-S., S. Lovejoy, D. Schertzer, et al. (2006), Multifractal earth topography, *Nonlinear Processes in Geophysics*, *13*(5), 541–570.

Gall, H.E., S.A. Sassman, L.S. Lee, and C.T. Jafvert (2011), Hormone discharges from a Midwest tile-drained agroecosystem receiving animal wastes, *Environmental science and technology*, *45*(20), 8755-8764.

Gelfand, I., R. Sahajpal, X. Zhang, R. C. Izaurralde, K. L. Gross, and G. P. Robertson (2013), Sustainable bioenergy production from marginal lands in the US Midwest, *Nature*, *493*(7433), 514–517.

Ginn, T. R. (1999), On the distribution of multicomponent mixtures over generalized exposure time in subsurface flow and reactive transport: Foundations, and formulations for groundwater age, chemical heterogeneity, and biodegradation, *Water Resour. Res.*, 35(5), 1395–1407.

Gran, K. B., P. Belmont, S. S. Day, C. Jennings, A. Johnson, L. Perg, and P. R. Wilcock (2009), Geomorphic evolution of the Le Sueur river, Minnesota, USA, and implications for current sediment loading, *Geological Society of America Special Papers*, *451*, 119–130.

Groisman, P. Y., R. W. Knight, and T. R. Karl (2012), Changes in intense precipitation over the central United States, *Journal of Hydrometeorology*, *13*(1), 47–66.

Groisman, P. Y., R. W. Knight, T. R. Karl, D. R. Easterling, B. Sun, and J. H. Lawrimore (2004), Contemporary changes of the hydrological cycle over the contiguous United States: Trends derived from in situ observations, *Journal of hydrometeorology*, *5*(1), 64–85.

Gupta, V. K., and E. Waymire (1989), Statistical self-similarity in river networks parameterized by elevation, *Water Resources Research*, *25*(3), 463–476.

Harman, C. J. (2015), Time-variable transit time distributions and transport: Theory and application to storage-dependent transport of chloride in a watershed, *Water Resour. Res.*, *51*(1), 1–30.

Heidbuchel, I., P. A. Troch, and S. W. Lyon (2013), Separating physical and meteorological controls of variable transit times in zero-order catchments, *Water Resour. Res.*, *49*, 7644–7657, doi:10.1002/2012WR013149.

Heidbuchel, I., P. A. Troch, S. W. Lyon, and M. Weiler (2012), The master transit time distribution of variable flow systems, *Water Resour. Res.*, *48*(6).

Higgins, R. W., and V. E. Kousky (2013), Changes in observed daily precipitation over the United States between 1950-79 and 1980–2009, *J. Hydrometeorol.*, 14(1), 105–121, doi:10.1175/JHM-D-12–062.1.

Hinck, P.J. (2008), Evapotranspiration Measurement and Modeling for Annual and Perennial Crops in South-Central Minnesota, *M.S. Thesis, Graduate School, University of Minnesota, Minneapolis, MN*.

Holmes, R., and G. Robertson (1963), Application of the relationship between actual and potential evapotranspiration in dry land agriculture, *Trans. ASAE*, *6*(1), 65–67.

Horton, R. E. (1945), Erosional development of streams and their drainage basins: Hydrophysical approach to quantitative morphology, *Geol. Soc. Am. Bull.*, *56*, 275–370.

Hough, S. (1989), On the use of spectral methods for the determination of fractal dimension, *Geophysical Research Letters*, *16*(7), 673–676.

Hrachowitz, M. et al. (2013), A decade of Predictions in Ungauged Basins (PUB)—a review, *Hydrol. Sci. J.*, *58*(6), 1198–1255.

Hrachowitz, M., C. Soulsby, D. Tetzlaff, and I. A. Malcolm (2011), Sensitivity of mean transit time estimates to model conditioning and data availability, *Hydrol. Processes*, *25*(6), 980–990.

Hrachowitz, M., C. Soulsby, D. Tetzlaff, and M. Speed (2010a), Catchment transit times and landscape controls: does scale matter?, *Hydrol. Processes*, *24*(1), 117–125.

Hrachowitz, M., C. Soulsby, D. Tetzlaff, I. A. Malcolm, and G. Schoups (2010b), Gamma distribution models for transit time estimation in catchments: Physical interpretation of parameters and implications for time-variant transit time assessment, *Water Resour. Res.*, *46*, W10536, doi:10.1029/2010WR009148.

Hrachowitz, M., C. Soulsby, D. Tetzlaff, J. J. C. Dawson, and I. A. Malcolm (2009), Regionalization of transit time estimates in montane catchments by integrating landscape controls, *Water Resour. Res.*, *45*, W05421, doi:10.1029/2008WR007496.

Jin, C., G. Sands, H. Kandel, J. Wiersma, and B. Hansen (2008), Influence of subsurface drainage on soil temperature in a cold climate, *Journal of Irrigation and Drainage Engineering*, *134*(1), 83–88.

Kalbermatten, M., D. Van De Ville, P. Turberg, D. Tuia, and S. Joost (2012), Multiscale analysis of geomorphological and geological features in high resolution digital elevation models using the wavelet transform, *Geomorphology*, *138*(1), 352–363.

Kanwar, R. S., R. M. Cruse, M. Ghaffarzadeh, A. Bakhsh, D. Karlen, and T. B. Bailey (2005), Corn-soybean and alternative cropping systems effects on no 3-n leaching losses in subsurface drainage water, *Applied engineering in agriculture*, *21*(2), 181.

Karl, T. R., R. W. Knight, D. R. Easterling, and R. G. Quayle (1996), Indices of climate change for the United States, *Bull. Am. Meteorol. Soc.*, *77*(2), 279–292, doi:10.1175/1520 0477(1996)077<0279:IOCCFT>2.0.CO;2.

Kennedy, C. D., C. Bataille, Z. Liu, S. Ale, J. VanDeVelde, C. R. Roswell, ... and G. J. Bowen, (2012), Dynamics of nitrate and chloride during storm events in agricultural catchments with different subsurface drainage intensity (Indiana, USA), *Journal of Hydrology*, *466*, 1-10.

Kiffney, P. M., C. M. Greene, J. E. Hall, and J. R. Davies (2006), Tributary streams create spatial discontinuities in habitat, biological productivity, and diversity in mainstream rivers, *Can. J. Fish. Aquat. Sci.*, 63, 2518–2530, doi:10.1139/F06-138.

Kirchner, J. W. (1993), Statistical inevitability of Horton's laws and the apparent randomness of stream channel networks, *Geology*, *21*(7), 591–594.

Kirchner, J. W. (2006), Getting the right answers for the right reasons: Linking measurements, analyses, and models to advance the science of hydrology, *Water Resour. Res.*, *42*(3).

Kirchner, J. W. (2009), Catchments as simple dynamical systems: Catchment characterization, rainfall-runoff modeling, and doing hydrology backward, *Water Resour. Res.*, 45, W02429, doi:10.1029/2008WR006912.

Kirchner, J. W. (2016a), Aggregation in environmental systems – Part 1: Seasonal tracer cycles quantify young water fractions, but not mean transit times, in spatially heterogeneous catchments, *Hydrol. Earth Syst. Sci.*, *20*(1), 279–297.

Kirchner, J. W. (2016b), Aggregation in environmental systems – Part 2: Catchment mean transit times and young water fractions under hydrologic nonstationarity, *Hydrol. Earth Syst. Sci.*, *20*(1), 299–328.

Kirchner, J. W., D. Tetzlaff, and C. Soulsby (2010), Comparing chloride and water isotopes as hydrological tracers in two Scottish catchments, *Hydrol. Processes*, *24*(12), 1631–1645.

Kirchner, J. W., P. J. Dillon, and B. D. Lazerte (1993), Predictability of geochemical buffering and runoff acidification in spatially heterogeneous catchments, *Water Resour. Res.*, *29*(12), 3891–3901, doi:10.1029/93WR02202.

Kirchner, J. W., X. Feng, and C. Neal (2000), Fractal stream chemistry and its implications for contaminant transport in catchments, *Nature*, *403*(6769), 524–527.

Kirkby, M. (1976), Tests of the random network model, and its application to basin hydrology, *Earth Surface Processes*, *1*(3), 197–212.

Kladivko, E. J., L. C. Brown, and J. L. Baker (2001), Pesticide transport to subsurface tile drains in humid regions of North America, *Critical Reviews in Environmental Science and Technology*, *31*(1), 1–62.

Laio, F., A. Porporato, L. Ridolfi, and I. Rodriguez-Iturbe (2001), Plants in water-controlled ecosystems: active role in hydrologic processes and response to water stress: II. Probabilistic soil moisture dynamics, *Advances in Water Resources*, *24*(7), 707–723.

Lindgren, G. A., G. Destouni, and A. V. Miller (2004), Solute transport through the integrated groundwater-stream system of a catchment, *Water Resour. Res.*, 40, W03511, doi:10.1029/2003WR002765.

Mallat, S. G. (1989a), A theory for multiresolution signal decomposition: the wavelet representation, *Pattern Analysis and Machine Intelligence, IEEE Transactions on*, *11*(7), 674–693.

Mallat, S. G. (1989b), Multifrequency channel decompositions of images and wavelet models, *Acoustics, Speech and Signal Processing, IEEE Transactions on*, *37*(12), 2091– 2110.

Mallat, S. G. (1999), A wavelet tour of signal processing. *Academic press*.

Mantilla, R., V. K. Gupta, and O. J. Mesa (2006), Role of coupled flow dynamics and real network structures on Hortonian scaling of peak flows, *Journal of Hydrology*, *322*(1), 155–167.

McDonnell, J. J. et al. (2007), Moving beyond heterogeneity and process complexity: A new vision for watershed hydrology, *Water Resour. Res.*, *43*(7).

McDonnell, J. J., and Beven, K. (2014), Debates-The future of hydrological sciences: A (common) path forward? A call to action aimed at understanding velocities, celerities and residence time distributions of the headwater hydrograph, *Water Resour. Res.*, 50, 5342–5350, doi:10.1002/2013wr015141, 2014.

McGlynn, B., J. McDonnell, M. Stewart, and J. Seibert (2003), On the relationships between catchment scale and streamwater mean residence time, *Hydrol. Processes*, *17*(1), 175–181.

McGuire, K. J., and J. J. McDonnell (2006), A review and evaluation of catchment transit time modeling, *Journal of Hydrology*, *330*(3), 543–563.

McGuire, K., D. DeWalle, and W. Gburek (2002), Evaluation of mean residence time in subsurface waters using oxygen-18 fluctuations during drought conditions in the Midappalachians, *Journal of Hydrology*, *261*(1), 132–149.

McGuire, K., J. J. McDonnell, M. Weiler, C. Kendall, B. McGlynn, J. Welker, and J. Seibert (2005), The role of topography on catchment-scale water residence time, *Water Resour. Res.*, *41*(5).

McMillan, H., D. Tetzlaff, M. Clark, and C. Soulsby (2012), Do time-variable tracers aid the evaluation of hydrological model structure? A multi-model approach, *Water Resour. Res.*, *48*, W05501, doi:10.1029/2011WR011688.

Minnesota Pollution Control Agency (2006), Water, Water Types and Programs, Surface Water, Wetlands, New reports on Minnesota's wetlands [Available at https://www.pca.state.mn.us/water/new-reports-minnesotas-wetlands].

Minnesota Pollution Control Agency (2007), Water, Water Types and Programs, Surface Water, Basins in Minnesota, Minnesota [Available at https://www.pca.state.mn.us/water/minnesota-river-basin].

Minnesota Pollution Control Agency (2013), About the MPCA, News and Media, Features Stories, Report on nitrogen in surface water [Available at https://www.pca.state.mn.us/news/report-nitrogen-surface-water].

McIsaac, G. F. and X. Hu (2004), Net N input and riverine N export from Illinois agricultural watersheds with and without extensive tile drainage, *Biogeochemistry*, *70*(2), 253-273.

Monaghan, R. M., R. J. Paton, L. C. Smith, and C. Binet (2000), Nutrient losses in drainage and surface runoff from a cattle-grazed pasture in Southland, In *Proceedings of the Conference-New Zealand Grassland Association*, 99-104.

Mulholland, P. J., et al. (2008), Stream denitrification across biomes and its response to anthropogenic nitrate loading, *Nature*, *452*(13), 202–205.

Muneepeerakul, R., E. Bertuzzo, H. J. Lynch, W. F. Fagan, A. Rinaldo, and I. Rodriguez-Iturbe (2008), Neutral metacommunity models predict fish diversity

patterns in Mississippi-Missouri basin, *Nature*, 453, 220–222, doi:10.1038/nature06813.

National Oceanic and Atmospheric Administration (2015), National Climatic Data Center, Climate Data Online, Washington, D. C. [Available at https://www.ncdc.noaa.gov/cdo-web/].

Nicollet, J. N. (1993), Joseph N. Nicollet on the Plains and Prairies: The Expeditions of 38-39, with Journals, Letters, and Notes on the Dakota Indians, *The National Academies*.

Niemi, A. J. (1977), Residence time distributions of variable flow processes, *The International Journal of Applied Radiation and Isotopes*, *28*(10), 855–860.

Ojakangas, R. W. (1982), Minnesota's geology, *University of Minnesota Press*.

Orloff, T., M. Kreslavsky, and E. Asphaug (2013), Distribution of polygon characteristic scale in Martian patterned ground terrain in the northern hemisphere using the Fourier transform, *Journal of Geophysical Research: Planets*, *118*(7), 1558–1566.

Pavelis, G. A. (1987), *Farm drainage in the United States: History, status, and prospects*, 1455, US Department of Agriculture, Economic Research Service.

Paybins, K. S. (2000), Water Quality in the Kanawha-New River Basin: West Virginia, Virginia, and North Carolina, 1996-98, *US Geological Survey*, 1204.

Pelletier, J. D. (1999), Self-organization and scaling relationships of evolving river networks, *Journal of Geophysical Research: Solid Earth (1978–2012)*, *104*(B4), 7359–7375.

Perron, J. T., J. W. Kirchner, and W. E. Dietrich (2008), Spectral signatures of characteristic spatial scales and nonfractal structure in landscapes, *Journal of Geophysical Research: Earth Surface (2003–2012)*, *113*(F4).

Porporato, A., and S. Calabrese (2015), On the probabilistic structure of water age, *Water Resour. Res.*, *51*(5), 3588–3600, doi:10.1002/2015WR017027.

Power, M. E., and W. E. Dietrich (2002), Food webs in river networks, *Ecol. Res.*, 17, 451–471.

Queloz, P., L. Carraro, P. Benettin, G. Botter, A. Rinaldo, and E. Bertuzzo (2015), Transport of fluorobenzoate tracers in a vegetated hydrologic control volume: 2. theoretical inferences and modeling, *Water Resour. Res.*, doi:10.1002/2014WR016508.

Ranalli, A. J., and D. L. Macalady (2010), The importance of the riparian zone and in-stream processes in nitrate attenuation in undisturbed and agricultural watersheds–A review of the scientific literature, *Journal of Hydrology*, *389*(3), 406-415.

Richard, T. L., and T. S. Steenhuis (1988), Tile drain sampling of preferential flow on a field scale, *Journal of Contaminant Hydrology*, *3*(2-4), 307-325.

Rigon, R., I. Rodriguez-Iturbe, A. Maritan, A. Giacometti, D. G. Tarboton, and A. Rinaldo (1996), On Hack's Law, *Water Resour. Res.*, *32*(11), 3367–3374, doi:10.1029/96WR02397.

Rinaldo, A., K. J. Beven, E. Bertuzzo, L. Nicotina, J. Davies, A. Fiori, D. Russo, and G. Botter (2011), Catchment travel time distributions and water flow in soils, *Water Resour. Res.*, *47*(7).

Rinaldo, A., P. Benettin, C. J. Harman, M. Hrachowitz, K. J. McGuire, Y. Van der Velde, E. Bertuzzo, and G. Botter (2015), Storage selection functions: A coherent framework for quantifying how catchments store and release water and solutes, *Water Resour. Res.*, *51*(6), 4840–4847.

Risken, H. (1984), Fokker-Planck Equation, in *The Fokker-Planck Equation*, vol. 18, pp. 63–95, Springer Berlin Heidelberg, Berlin, Heidelberg.

Roa-García, M. C. and Weiler, M.: Integrated response and transit time distributions of watersheds by combining hydrograph separation and long-term transit time modeling, *Hydrol. Earth Syst. Sci.*, *14*, 1537–1549, doi:10.5194/hess-14-1537-2010, 2010.

Rodgers, P., C. Soulsby, S. Waldron, and D. Tetzlaff (2005), Using stable isotope tracers to assess hydrological flow paths, residence times and landscape influences in a nested mesoscale catchment, *Hydrol. Earth Syst. Sci.*, *9*(3), 139–155, doi:10.5194/hess-9-139-2005.

Rodhe, A., L. Nyberg, and K. Bishop (1996), Transit times for water in a small till catchment from a step shift in the oxygen 18 content of the water input, *Water Resour. Res.*, *32*(12), 3497–3511.

Rodriguez-Iturbe, I., and A. Rinaldo (2001), *Fractal river basins: chance and self-organization*, Cambridge University Press.

Schilling, K. E., and M. Helmers (2008), Effects of subsurface drainage tiles on streamflow in Iowa agricultural watersheds: Exploratory hydrograph analysis, *Hydrol. Processes*, *22*(23), 4497–4506.

Schilling, K.E., C.F. Wolter, T.M Isenhart, and R.C. Schultz (2015), Tile drainage reduces groundwater travel times and compromises riparian buffer effectiveness, *Journal of Environmental Quality*, *44*(6), 1754-1763.

Schottler, S. P., J. Ulrich, P. Belmont, R. Moore, J. Lauer, D. R. Engstrom, and J. E. Almendinger (2014), Twentieth century agricultural drainage creates more erosive rivers, *Hydrol. Processes*, *28*(4), 1951–1961.

Seeger, S., and M. Weiler (2014), Reevaluation of transit time distributions, mean transit times and their relation to catchment topography, *Hydrol. Earth Syst. Sc.*, *18* (12), 4751-4771, doi:10.5194/hess-18-4751-2014.

Sivapalan, M., C. Jothityangkoon, and M. Menabde (2002), Linearity and nonlinearity of basin response as a function of scale: discussion of alternative definitions, *Water Resour. Res.*, *38*(2), 4–1.

Skaggs, R., M. Breve, and J. Gilliam (1994), Hydrologic and water quality impacts of agricultural drainage?, *Critical Reviews in Environmental Science and Technology*, *24*(1), 1–32.

Sklar, L. S., W. E. Dietrich, E. Foufoula-Georgiou, B. Lashermes, and D. Bellugi (2006), Do gravel bed river size distributions record channel network structure?, *Water Resour. Res.*, 42, W06D18, doi:10.1029/2006WR005035.

Soulsby, C., D. Tetzlaff, P. Rodgers, S. Dunn, and S. Waldron (2006), Runoff processes, stream water residence times and controlling landscape characteristics in a mesoscale catchment: an initial evaluation, *Journal of Hydrology*, *325*(1), 197–221.

Soulsby, C., K. Piegat, J. Seibert, and D. Tetzlaff (2011), Catchment scale estimates of flow path partitioning and water storage based on transit time and runoff modelling, *Hydrol. Processes*, *25*(25): 3960–3976.

Soulsby, C., R. Malcolm, R. Helliwell, R. C. Ferrier, and A. Jenkins (2000), Isotope hydrology of the Allt a' Mharcaidh catchment, Cairngorms, Scotland: implications for hydrological pathways and residence times, *Hydrol. Process.*, *14*(4), 747–762, doi:10.1002/(SICI)1099-1085(200003)14:4<747::AID-HYP970>3.0.CO;2-0.

Spaling, H. (1995), Analyzing cumulative environmental effects of agricultural land drainage in southern Ontario, Canada, *Agriculture, ecosystems and environment* *53*(3), 279-292.

Spaling, H., and B. Smit (1995), A conceptual model of cumulative environmental effects of agricultural land drainage, *Agriculture, Ecosystems & Environment*, *53*(2), 99–108.

Stewart-Koster, B., M. J. Kennard, B. D. Harch, F. Sheldon, A. H. Arthington, and B. J. Pusey (2007), Partitioning the variation in stream fish assemblages within a spatio-temporal hierarchy, *Mar. Freshwater Res.*, 58, 675–686.

Strahler, A. N. (1957), Quantitative analysis of watershed geomorphology, *Trans. AGU*, *38*, 913–920.

Tarboton, D. G. (1996), Fractal river networks, Horton's laws and Tokunaga cyclicity, *Journal of Hydrology*, *187*, 105–117.

Tarboton, D. G., R. L. Bras, and I. Rodriguez-Iturbe (1991), On the extraction of channel networks from digital elevation data, *Hydrol. Process.*, *5*(1), 81–100, doi:10.1002/hyp.3360050107.

Tetzlaff, D., J. Seibert, and C. Soulsby (2009b), Inter-catchment comparison to assess the influence of topography and soils on catchment transit times in a geomorphic province; the Cairngorm Mountains, Scotland, *Hydrol. Processes*, *23*(13), 1874–1886.

Tetzlaff, D., J. Seibert, K. J. McGuire, H. Laudon, D. A. Burns, S. M. Dunn, and C. Soulsby (2009a), How does landscape structure influence catchment transit time across different geomorphic provinces?, *Hydrol. Processes*, *23*, 945–953, doi:10.1002/hyp.7240.

Tilman, D., C. Balzer, J. Hill, and B. L. Befort (2011), Global food demand and the sustainable intensification of agriculture, *Proceedings of the National Academy of Sciences*, *108*(50), 20260-20264.

Tokunaga, E. (1978), Consideration on the composition of drainage networks and their evolution, *Department of Geography, Tokyo Metropolitan University*, *13*, 1–27.

Tomer, M., D. Meek, D. Jaynes, and J. Hatfield (2003), Evaluation of nitrate nitrogen fluxes from a tile-drained watershed in central Iowa, *Journal of Environmental Quality*, *32*(2), 642–653.

Troch, P. A., G. A. Carrillo, I. Heidbüchel, S. Rajagopal, M. Switanek, T. H. M. Volkmann, and M. Yaeger (2009), Dealing with Landscape Heterogeneity in Watershed Hydrology: A Review of Recent Progress toward New Hydrological Theory, *Geogr. Compass*, *3*(1), 375–392.

Troch, P.A., G. Carrillo, M. Sivapalan, T. Wagener, and K. Sawicz (2013), Climate-vegetation soil interactions and long-term hydrologic partitioning: signatures of catchment co-evolution, *Hydrol. Earth Syst. Sci.*, *17*, 2209–2217, doi:10.5194/hess-17-2209-2013.

Tscharntke, T., Y. Clough, T.C. Wanger, L. Jackson, I. Motzke, I. Perfecto, J. Vandermeer, and A. Whitbread (2012), Global food security, biodiversity conservation and the future of agricultural intensification, *Biological Conservation*, *151*(1), 53-59.

Tucker, G. E., and R. L. Bras (1998), Hillslope processes, drainage density, and landscape morphology, *Water Resources Research*, *34*(10), 2751–2764.

United States Geological Survey (2012), National Hydrography Dataset 2.1, Washington, D. C. [Available at https://nhd.usgs.gov/data.html].

United States Department of Agriculture (2015), National Agricultural Statistics Service, Data and Statistics, Quick Stats 2.0, Washington, D. C. [Available at http://quickstats.nass.usda.gov/].

U.S. Department of Agriculture (2015), National Resources Conservation Service, Soil, Soils Data Access, Washington, D. C. [Available at http://quickstats.nass.usda.gov/].

United Stated Bureau of Reclamation (2008), *Methow Subbasin Geomorphic Assessment, Okanogan County Technical Appendices*, Department of the Interior Bureau of Reclamation.

van der Velde, Y., P. J. J. F. Torfs, S. E. A. T. M. van der Zee, and R. Uijlenhoet (2012), Quantifying catchment-scale mixing and its effect on time-varying travel time distributions, *Water Resour. Res.*, *48*(6), doi:10.1029/2011WR011310.

Velde, v. d. Y., P. Torfs, S. Zee, and R. Uijlenhoet (2012), Quantifying catchment-scale mixing and its effect on time-varying travel time distributions, *Water Resour. Res.*, *48*(6).

Velde, Y., I. Heidbuchel, S. W. Lyon, L. Nyberg, A. Rodhe, K. Bishop, and P. A. Troch (2014), Consequences of mixing assumptions for time-variable travel time distributions, *Hydrol. Processes*, doi:10.1002/hyp.10372.

Veneziano, D., and V. Iacobellis (1999), Self-similarity and multifractality of topographic surfaces at basin and subbasin scales, *Journal of Geophysical Research: Solid Earth (1978–2012)*, *104*(B6), 12,797–12,812.

Villarini, G., J. A. Smith, M. L. Baeck, R. Vitolo, D. B. Stephenson, and W. F. Krajewski (2011), On the frequency of heavy rainfall for the Midwest of the United States, *J. Hydrol.*, *400*(1-2), 103-120, doi:10.1016/j.jhydrol.2011.01.027.

Vorosmarty, C. J., and D. Sahagian (2000), Anthropogenic disturbance of the terrestrial water cycle, *BioScience*, *50*(9), 753–765.

Voss, R. F. (1988), Fractals in nature: from characterization to simulation, *Springer*, *The science of fractal images*, pp. 21–70.

Weiler, M., B. L. McGlynn, K. J. McGuire, and J. J. McDonnell (2003), How does rainfall become runoff? A combined tracer and runoff transfer function approach, *Water Resour. Res.*, *39*(11).

Wörman, A., A. I. Packman, L. Marklund, J. W. Harvey, and S. H. Stone (2007), Fractal topography and subsurface water flows from fluvial bedforms to the continental shield, *Geophysical Research Letters*, *34*(7).

Young, P. (2003), Top-down and data-based mechanistic modelling of rainfall-flow dynamics at the catchment scale, *Hydrol. Process.*, *17*(11), 2195–2217.

Zanardo, S., I. Zaliapin, and E. Foufoula-Georgiou (2013), Are American rivers Tokunaga self-similar? New results on fluvial network topology and its climatic dependence, *Journal of Geophysical Research: Earth Surface*, *118*(1), 166–183.

Zedler, J. B. (2003), Wetlands at your service: reducing impacts of agriculture at the watershed scale, *Frontiers in Ecology and the Environment*, *1*(2), 65–72.

Zhang, Y.-K., and K. Schilling (2006), Increasing streamflow and baseflow in Mississippi river since the 1940s: Effect of land use change, *Journal of Hydrology*, *324*(1), 412–422.

Zucker, L., and L. Brown (1998), Agricultural drainage: Water quality impacts and subsurface drainage studies in the Midwest, *Ohio State University Extension*, *871*.